

NASA/TM-2001-206892, Vol. 15



SeaWiFS Postlaunch Technical Report Series

Stanford B. Hooker and Elaine R. Firestone, Editors

Volume 15, Results of the Second SeaWiFS Data Analysis Round Robin, March 2000 (DARR-00)

S.B. Hooker, G. Zibordi, J-F Berthon, D. D'Alimonte, S. Maritorena, S. McLean, and J. Sildam

National Aeronautics and
Space Administration

Goddard Space Flight Center
Greenbelt, Maryland 20771

December 2001

The NASA STI Program Office ... in Profile

Since its founding, NASA has been dedicated to the advancement of aeronautics and space science. The NASA Scientific and Technical Information (STI) Program Office plays a key part in helping NASA maintain this important role.

The NASA STI Program Office is operated by Langley Research Center, the lead center for NASA's scientific and technical information. The NASA STI Program Office provides access to the NASA STI Database, the largest collection of aeronautical and space science STI in the world. The Program Office is also NASA's institutional mechanism for disseminating the results of its research and development activities. These results are published by NASA in the NASA STI Report Series, which includes the following report types:

- **TECHNICAL PUBLICATION.** Reports of completed research or a major significant phase of research that present the results of NASA programs and include extensive data or theoretical analysis. Includes compilations of significant scientific and technical data and information deemed to be of continuing reference value. NASA's counterpart of peer-reviewed formal professional papers but has less stringent limitations on manuscript length and extent of graphic presentations.
- **TECHNICAL MEMORANDUM.** Scientific and technical findings that are preliminary or of specialized interest, e.g., quick release reports, working papers, and bibliographies that contain minimal annotation. Does not contain extensive analysis.
- **CONTRACTOR REPORT.** Scientific and technical findings by NASA-sponsored contractors and grantees.

- **CONFERENCE PUBLICATION.** Collected papers from scientific and technical conferences, symposia, seminars, or other meetings sponsored or cosponsored by NASA.
- **SPECIAL PUBLICATION.** Scientific, technical, or historical information from NASA programs, projects, and mission, often concerned with subjects having substantial public interest.
- **TECHNICAL TRANSLATION.** English-language translations of foreign scientific and technical material pertinent to NASA's mission.

Specialized services that complement the STI Program Office's diverse offerings include creating custom thesauri, building customized databases, organizing and publishing research results . . . even providing videos.

For more information about the NASA STI Program Office, see the following:

- Access the NASA STI Program Home Page at <http://www.sti.nasa.gov/STI-homepage.html>
- E-mail your question via the Internet to help@sti.nasa.gov
- Fax your question to the NASA Access Help Desk at (301) 621-0134
- Telephone the NASA Access Help Desk at (301) 621-0390
- Write to:
NASA Access Help Desk
NASA Center for AeroSpace Information
7121 Standard Drive
Hanover, MD 21076-1320



SeaWiFS Postlaunch Technical Report Series

Stanford B. Hooker, Editor
NASA Goddard Space Flight Center, Greenbelt, Maryland

Elaine R. Firestone, Senior Technical Editor
Science Applications International Corporation, Beltsville, Maryland

Volume 15, Results of the Second SeaWiFS Data Analysis Round Robin, March 2000 (DARR-00)

Stanford B. Hooker
NASA Goddard Space Flight Center, Greenbelt, Maryland

Giuseppe Zibordi
Jean-François Berthon
Davide D'Alimonte
JRC Space Applications Institute, Ispra, Italy

Stéphane Maritorena
UCSB Institute for Computational Earth System Science, Santa Barbara, California

Scott McLean
Juri Sildam
Satlantic, Inc., Halifax, Canada

ISSN 1522-8789

Available from:

NASA Center for AeroSpace Information
7121 Standard Drive
Hanover, MD 21076-1320
Price Code: A17

National Technical Information Service
5285 Port Royal Road
Springfield, VA 22161
Price Code: A10

PREFACE

Some of the primary objectives of the SeaWiFS Project, as stated in Volume 1 of the *SeaWiFS Prelaunch Technical Report Series* (Hooker, et al. 1992) are to achieve a radiometric accuracy to within 5% absolute and 1% relative, water-leaving radiances to within 5% absolute, and chlorophyll *a* concentration to within 35% over the range of 0.05–50 mg m⁻³. These goals are challenging, because they require very accurate estimation of a large number of variables, both radiometric and biological. The SeaWiFS Project, in collaboration with the SIMBIOS Project, continues to address calibration, measurement protocol, and data analysis issues associated with reducing the uncertainties in the key variables required to achieve the stated measurement goals. This overall effort has now been underway for a decade and continues. The work completed prior to the launch of SeaWiFS is documented in Hooker and McClain (2000). All 14 volumes of the *SeaWiFS Postlaunch Technical Report Series* have been dedicated to calibration and validation topics (these include two index volumes).

Volume 15 is the report of the second Data Analysis Round Robin executed in March 2000 (DARR-00), which focused on variations in spectral upwelling radiance, downwelling irradiance, and diffuse attenuation coefficients resulting from differences in data processing methods. The first Data Analysis Round Robin (DARR-94) demonstrated that different analysis techniques can produce reasonably similar results with so-called *good* data (Siegel et al. 1995); however, with noisy data, the results were inconsistent. DARR-94 did not recommend specific techniques as being clearly superior to others. DARR-00 represents a more detailed intercomparison, but does not include the same suite of analysis methods. The participants in DARR-00 were the Goddard Space Flight Center, the Joint Research Center, and Satlantic, Inc. All three groups have extensive experience and have worked on a variety of field programs together. Each has developed its own analysis approach making an intercomparison a natural extension of their ongoing collaboration. As might be expected, the results show differences in the derived products and in some cases, the differences are substantial. These results are of interest to the bio-optics community because many groups have also developed their own analysis methodologies and should be aware of the considerations outlined in this study.

These analysis round robins were conducted on a voluntary basis with the philosophy and purpose of addressing difficult processing problems so as to deliver better data products. The DARR-00 group has dealt with a number of perplexing issues and has documented their approach and findings in an open and straightforward manner. Their efforts and honest appraisals are laudable, and advance the state of the art a step closer to meeting our data accuracy requirements.

Greenbelt, Maryland
May 2001

— C. R. McClain

Table of Contents

Prologue	1
1. The Second SeaWiFS Ocean Optics DARR (DARR-00)	4
1.1 Introduction	4
1.2 Instrumentation	5
1.2.1 The AMT Instruments	6
1.2.2 The AAOT Instruments	7
1.3 The DARR-00 Database	8
1.3.1 The GSFC Data	8
1.3.2 The JRC Data	9
1.3.3 The Data Products	9
1.4 Data Analysis Methods	9
1.5 Results-Standard (V1)	16
1.5.1 $L_u(0^-)$	17
1.5.2 $E_d(0^-)$	19
1.5.3 K_L and K_d	20
1.5.4 $E_d(0^+)$	21
1.5.5 R_{rs}	21
1.5.6 $[L_w]_N$	23
1.5.7 $E_u(0^-)$ and $Q_n(0^-)$	25
1.5.8 Ancillary Variables	25
1.5.9 V1 Summary	27
1.6 Results-Nonstandard	29
1.6.1 V2 Summary	29
1.6.2 V3 Summary	31
1.6.3 V4 Summary	37
1.6.4 V5 Summary	37
1.7 Discussion	40
1.8 Conclusions	45
2. The GSFC Data Processing System	46
2.1 Introduction	46
2.2 Data Collection	47
2.3 Data Format	47
2.4 Processing Steps	47
2.4.1 Data Conversion	47
2.4.2 Data Visualization	49
2.4.3 In-Water Data Products	49
2.4.4 Above-Water Data Products	50
2.4.5 Ancillary Data Products	50
2.5 Summary	50
3. The JRC Data Processing System	52
3.1 Introduction	52
3.2 Data Requirements	53
3.3 Data Processing Steps	53
3.3.1 Calibration and Formatting	53
3.3.2 Filtering and Processing	55
3.4 Summary	56

Table of Contents (*cont.*)

4.	The ProSoft Optical Data Processor	57
4.1	Introduction	57
4.2	Data Processing	57
4.2.1	Level-1 Data Processing	58
4.2.2	Level-2 Data Processing	61
4.2.3	Level-3 Data Processing	62
4.3	Summary	65
APPENDIX A	66
APPENDIX B	66
GLOSSARY	66
SYMBOLS	67
REFERENCES	69
THE SEAWIFS POSTLAUNCH TECHNICAL REPORT SERIES	71

ABSTRACT

The accurate determination of upper ocean apparent optical properties (AOPs) is essential for the vicarious calibration of the Sea-viewing Wide Field-of-view Sensor (SeaWiFS) instrument and the validation of the derived data products. To evaluate the importance of data analysis methods upon derived AOP values, the Second Data Analysis Round Robin (DARR-00) activity was planned during the latter half of 1999 and executed during March 2000. The focus of the study was the intercomparison of several standard AOP parameters: a) the upwelled radiance immediately below the sea surface, $L_u(0^-, \lambda)$; b) the downward irradiance immediately below the sea surface, $E_d(0^-, \lambda)$; c) the diffuse attenuation coefficients from the upwelling radiance and the downward irradiance profiles, $K_L(\lambda)$ and $K_d(\lambda)$, respectively; d) the incident solar irradiance immediately above the sea surface, $E_d(0^+, \lambda)$; e) the remote sensing reflectance, $R_{rs}(\lambda)$; f) the normalized water-leaving radiance, $[L_W(\lambda)]_N$; g) the upward irradiance immediately below the sea surface, $E_u(0^-)$, which is used with the upwelled radiance to derive the nadir Q -factor immediately below the sea surface, $Q_n(0^-, \lambda)$; and h) ancillary parameters like the solar zenith angle, θ , and the total chlorophyll a concentration, C_{Ta} , derived from the optical data through statistical algorithms. In the results reported here, different methodologies from three research groups were applied to an identical set of 40 multispectral casts in order to evaluate the degree to which differences in data analysis methods influence AOP estimation, and whether any general improvements can be made. The overall results of DARR-00 are presented in Chapter 1 and the individual methods used by the three groups and their data processors are presented in Chapters 2–4.

PROLOGUE

The Sea-viewing Wide Field-of-view Sensor (SeaWiFS) Project is tasked with executing a program to acquire a global ocean color data set, validate and monitor its accuracy and quality, process the radiometric data into geophysical units using a set of atmospheric and bio-optical algorithms, and distribute the final products to the scientific community through the Goddard Space Flight Center (GSFC) Distributed Active Archive Center (DAAC). The long-standing objective of the SeaWiFS Project is to produce water-leaving radiances to within 5% absolute (Hooker and Esaias 1993).

The accurate determination of upper ocean apparent optical properties (AOPs) is essential for the vicarious calibration of an ocean color sensor like SeaWiFS and the validation of the derived data products, because the sea-truth measurements are the reference data to which the satellite observations are compared (McClain et al. 1998). The only economically feasible approach for minimizing spatial biases for a global data set is to maximize the acquisition of *in situ* measurements by soliciting data from the oceanographic community at large. The SeaWiFS Bio-Optical Archive and Storage System (SeaBASS) is the database maintained by the Project for these data and SeaWiFS sponsored field activities (Hooker et al. 1994).

The uncertainties associated with *in situ* AOP measurements have various sources, such as, the deployment and measurement protocols used in the field, the absolute calibration of the radiometers, the environmental conditions encountered during data collection, the conversion of the light signals to geophysical units in a data processing scheme, and the stability of the radiometers in the

harsh environment they are subjected to during transport and use. In recent years, progress has been made in estimating the magnitude of some of these uncertainties and in defining procedures for minimizing them. For the SeaWiFS Project, the first step in the process of controlling sources of uncertainty was to convene a workshop to draft the SeaWiFS Ocean Optics Protocols (SOOP). The SOOP adheres to the Joint Global Ocean Flux Study (JGOFS) sampling procedures (Joint Global Ocean Flux Study 1991) and defines the standards for optical measurements to be used in SeaWiFS radiometric validation and algorithm development (Mueller and Austin 1992). The SOOP is periodically updated as deficiencies are identified and outstanding issues are resolved (Mueller and Austin 1995, and Mueller 2000).

The follow-on inquiries into controlling sources of uncertainty investigated a variety of topics. The SeaWiFS Intercalibration Round-Robin Experiment (SIRREX) activity demonstrated that the uncertainties in the traceability between the spectral irradiance of calibration lamps were approximately 1.0%, and the intercomparisons of sphere radiance was approximately 1.5% in absolute spectral radiance and 0.3% in stability (Mueller et al. 1996). The first SeaWiFS Data Analysis Round Robin (DARR-94) showed differences in commonly used data processing methods for determining $L_u(0^-, \lambda)$ and $E_d(0^+, \lambda)$ were about 3–4% of the aggregate mean estimate (Siegel et al. 1995). Hooker and Aiken (1998) made estimates of radiometer stability using the SeaWiFS Quality Monitor (SQM), a portable and stable light source, and showed the stability of their radiance and irradiance sensors in the field during a 36-day deployment was on average to within 1.0% (although

some channels occasionally performed much worse). More recently, Hooker and Maritorena (2000) quantified differences in the in-water methods and techniques employed for making radiometric measurements in support of SeaWiFS validation and demonstrated a total uncertainty in the measurement of in-water AOPs at approximately the 3% level.

As part of the SeaWiFS Project calibration and validation activities, the SeaWiFS field program conducted specific experiments to investigate these issues. The experiments took place during several Atlantic Meridional Transect (AMT) cruises on board the Royal Research Ship *James Clark Ross* (JCR) between England and the Falkland Islands. The odd-numbered, southbound cruises sampled the boreal autumn and austral spring; while the even-numbered, northbound cruises sampled the boreal spring and austral autumn (Aiken and Hooker 1997).

The accuracy of any AOP determination is a function of the quality of the observational measurement, the data acquisition methodology, and the data processing method employed. The former includes the quality of the optical calibration and the radiometric stability of the instruments while they are being used in the field. To minimize observational uncertainties, the SeaWiFS Project has sponsored a variety of multidisciplinary workshops to outline the observations and sampling protocols required for bio-optical algorithm development (Mueller and Austin 1992 and 1995). One of the consequences of the workshops was the establishment of the series of SIRREX activities to demonstrate and advance the state of the art for calibrating the instruments used in field activities.

Although the SeaBASS architecture allows for some quality control (Hooker et al. 1994), it is based primarily on resolving obvious clerical errors in the reporting of where and when data acquisition activities took place—it does not attempt to quantify differences in the data analysis methods employed. The latter is, in part, a function of how the individual software packages deal with data filtering, binning, smoothing, and removing possible artifacts from changes in surface illumination, ship shadow, or reflections and wave focusing.

The focus of this intercomparison study is the estimation of a variety of optical parameters derived from vertical profiles of the downward irradiance, $E_d(z, \lambda)$, the upwelled (nadir) radiance, $L_u(z, \lambda)$, and the upward irradiance, $E_u(z, \lambda)$. In the results reported here, different methodologies from three international groups are applied to the aforementioned multispectral profiles to evaluate the degree to which data analysis methods influence AOP estimation, and whether any general improvements can be made. In addition to GSFC, there were three groups involved:

- a) The University of California at Santa Barbara (UCSB) Institute for Computational Earth System Science (ICESS),

- b) The Joint Research Centre (JRC) Marine Environment Unit of the Space Applications Institute, and
- c) Satlantic, Inc. (Halifax, Canada).

The overall results of the second Data Analysis Round Robin (DARR-00) are presented in Chapter 1 and the individual methods of the three groups are presented in Chapters 2–4, respectively. The participants in the activity are given in Appendix A. A summary of the material presented in each chapter is given below.

1. *The Second SeaWiFS Ocean Optics DARR (DARR-00)*

The focus of this round-robin study was the estimation of a variety of commonly used data products derived from in-water optical measurements. Eleven parameters important to bio-optical analyses were determined and compared from three different in-water optical data processors from the JRC, GSFC, and Satlantic, Inc. The parameters were calculated for a data set covering a large range of total chlorophyll *a* concentration ($0.08\text{--}2.43\text{ mg m}^{-3}$). All three processors were intercompared using 40 optical profiles; the JRC and GSFC processors were further intercompared using an additional 10 casts (the larger data set increased the amount of data in very clear waters, thereby extending the lowest total chlorophyll *a* concentration to 0.027 mg m^{-3}). In terms of overall spectral averages, many of the JRC and GSFC results intercompared to within 2.5%, but none of the Satlantic results intercompared with the other processors at this level. Band-ratio averages, however, frequently intercompared to within 2.5% for all processor combinations, even when the overall spectral averages did not. These results suggest a database constructed with processed data from a wide source of contributors will have substantially higher uncertainties than a database constructed with raw data which is processed with a single processor, although band ratios regularly provide reduced uncertainties with respect to individual spectral uncertainties.

2. *The GSFC Data Processing System*

The GSFC data processing system was designed to calculate apparent optical properties from underwater profiles of upward and downward irradiance, as well as upwelling radiance, from a wide variety of open ocean regimes. The full processing involves three steps: a) the calibration of the data, b) the establishment of the extrapolation interval, and c) the derivation of the final data products. In the first step, special files containing dark voltages are used to remove detector offsets and apply a pressure tare to the depth sensor. The second step is done interactively while viewing all the optical and ancillary (sensor tilts, fluorescence, etc.) fields. The final step is usually executed in batch mode using a file of extrapolation limits created in the second step. All of the code is written in the Interactive Data Language (IDL) programming environment from Research Systems, Inc. (Boulder, Colorado).

3. *The JRC Data Processing System*

The JRC Data Processor was developed for the analysis of field data collected in coastal and marine regions in support of ocean color calibration and validation activities. The code specifically supports the calibration, formatting, visualization, and processing of in-water optical profiles of $L_u(z, \lambda)$, $E_d(z, \lambda)$, and $E_u(z, \lambda)$ collected with the Satlantic seven-channel OCR-200 and OCI-200 sensor series. The user can define a variety of options which permit the selection of the extrapolation interval for the computation of the near-surface values, and the removal of outliers through statistical filtering. Relevant features include the possibility to minimize measurement perturbations such as instrument self shading, bottom effects, and superstructure shading (although the latter is restricted to measurements performed at the *Acqua Alta* Oceanographic Tower (AAOT) site in the northern Adriatic Sea). Each step of the processing is supported by the graphic presentation of intermediate results. Output products are the subsurface values $L_u(0^-, \lambda)$, $E_d(0^-, \lambda)$, and $E_u(0^-, \lambda)$; the diffuse attenuation coefficients $K_d(\lambda)$, $K_L(\lambda)$, and $K_u(\lambda)$; plus the derived products $R(0^-, \lambda)$, $R_{rs}(\lambda)$, $[L_W(\lambda)]_N$, and $Q_n(0^-, \lambda)$.

4. *The ProSoft Optical Data Processor*

The ProSoft data processor was developed for the analysis of optical data collected with instruments manufactured by Satlantic, Inc., including profiling and fixed-depth (buoy) systems. The data processing steps are organized into different levels which follow, as much as possible, the procedures given in the *Ocean Optics Protocols for SeaWiFS Validation, Revision 1* (Mueller and Austin 1995). The processing involves three steps wherein the level-1 raw data (usually binary) are converted to calibrated values (engineering units) using one of several options for dark current correction, the level-2 data are averaged and corrected for acquisition and performance problems (if any), and the level-3 data are used to compute the final data products, e.g., R_{rs} , $[L_W(\lambda)]_N$, photosynthetically available radiation (PAR), etc. Processing can be done manually (and interactively) by the user, guided by the ProSoft processing steps, or in a fully automated batch mode. A notable difference between ProSoft and other data processors is the diffuse attenuation coefficient can be estimated using a traditional estimation of the slope of the optical variables within a user-defined extrapolation interval or using a new methodology based on multiresolution wavelet analysis.

Chapter 1

The Second SeaWiFS Ocean Optics DARR (DARR-00)

STANFORD B. HOOKER
NASA Goddard Space Flight Center
Greenbelt, Maryland

GIUSEPPE ZIBORDI
Marine Environment Unit, Space Applications Institute
Joint Research Centre of the European Commission
Ispra, Italy

STÉPHANE MARITORENA
UCSB Institute for Computational Earth System Science
Santa Barbara, California

ABSTRACT

The focus of this round-robin study was the estimation of a variety of commonly used data products derived from in-water optical measurements. Eleven parameters important to bio-optical analyses were determined and compared from three different in-water optical data processors from the JRC, the GSFC, and Satlantic, Inc. The parameters were calculated for a data set covering a large range of total chlorophyll *a* concentration ($0.08\text{--}2.43\text{ mg m}^{-3}$). All three processors were intercompared using 40 optical profiles; the JRC and GSFC processors were further intercompared using an additional 10 casts (the larger data set increased the amount of data in very clear waters, thereby extending the lowest total chlorophyll *a* concentration to 0.027 mg m^{-3}). In terms of overall spectral averages, many of the JRC and GSFC results intercompared to within 2.5%, but none of the Satlantic results intercompared with the other processors at this level. Band-ratio averages, however, frequently intercompared to within 2.5% for all processor combinations, even when the overall spectral averages did not. These results suggest a database constructed with processed data from a wide source of contributors will have substantially higher uncertainties than a database constructed with raw data which is processed with a single processor, although band ratios regularly provide reduced uncertainties with respect to individual spectral uncertainties.

1.1 INTRODUCTION

The SeaWiFS calibration and validation plan (Hooker and McClain 2000) relies on radiometric measurements made at sea by a diverse community of investigators. One of the long-standing objectives of the SeaWiFS Project is to produce spectral water-leaving radiances, $L_w(\lambda)$, within an uncertainty of 5% (Hooker and Esaias 1993), and the sea-truth measurements are the reference data to which the satellite observations are compared (McClain et al. 1998). The accuracy of the field measurements are, therefore, of crucial importance.

If a total 5% uncertainty level is to be maintained for a vicarious calibration exercise (remote plus *in situ* instrumentation), approximately half of the uncertainty budget, i.e., 2.5% (actually if quadrature sums are used, the ground

truth component is closer to 3.5%), is available for the ground truth component. Hooker and Maritorena (2000) investigated whether or not current deployment and processing schemes meet the 2.5% objective, and found several systems almost did. Their study considered four sources of uncertainty: calibration, *in situ* stability, data collection, and data processing. They estimated data processing, which was restricted to a single data processing package, contributed approximately 2% uncertainty to the total uncertainty.

The primary objective of DARR-00 was to use multiple data processors to investigate whether or not a data processing uncertainty below the 3–4% result determined for DARR-94 is achievable. Two uncertainty thresholds were considered for this inquiry: 2.5% as a hoped for minimum

(because it represents almost all of the ground truth uncertainty budget, but is below the DARR-94 results), and 1.0% as a needed goal (because it permits some expansion in the other components of the total uncertainty budget).

1.2 INSTRUMENTATION

As part of the SeaWiFS Project calibration and validation activities, the SeaWiFS field program participated in AMT cruises on board the JCR and in deployments to the AAOT site. The AMT Program exploits the passage of the JCR as it transits more than 100° of latitude and 50° of longitude in the North and South Atlantic Oceans between the UK and the Falkland Islands in support of British Antarctic expeditions. In September, the JCR sails from the UK, and the following April it makes the return trip with the vast majority of the sampling taking place in Case-1 waters (Aiken et al. 2000).

The AAOT is located in the northern Adriatic Sea (12.51°E, 45.31°N) approximately 15 km east of the city of Venice (Italy). The site has been visited on a monthly basis since the fall of 1995 in support of ocean color calibration and validation activities. Because of its near-coastal location, the site may be characterized by Case-1 or Case-2 conditions.

The AOP instruments used on AMT and AAOT deployments included the SeaWiFS Optical Profiling System (SeaOPS) and the Low-Cost NASA Environmental Sampling System (LoCNESS) for the former, and the Wire-Stabilized Profiling Environmental Radiometer (WiSPER) and a variant of the miniature NASA Environmental Sampling System (miniNESS) for the latter. SeaOPS and WiSPER are deployed using a winch and crane, whereas, LoCNESS and miniNESS are floated away from the sampling platform and deployed by hand.

Although there are many differences between optical instruments deployed with winch systems versus free-fall units, the primary differences are related to ship-induced perturbations, wave motion, and the time required to perform a cast. Optical instruments deployed with winch systems potentially suffer from more disadvantages than advantages:

1. Cranes have a limited reach, so platform perturbations can be a problem.
2. For a ship, the vessel is not decoupled from the ocean surface, so roll and pitch can cause measurement problems (particularly for irradiance sensors).
3. Winches and cranes are sophisticated systems, so there is a continuing vulnerability associated with breakdowns, especially with the hydraulic subsystems (this vulnerability is much reduced in the shallow coastal environment where small electric winches are the most frequently used).
4. At sea, winches and cranes are stowed during passage, so they require relatively lengthy preparation

time for operations to begin and end, which means a quick cast during optimal sky conditions is frequently difficult to achieve.

5. The instruments are not submerged until they are far from the side of the platform, so there is very little chance of them being damaged by wave action.
6. Many winches have low wire speeds, so the cycle rate for a complete cast is relatively long (in shallow water this is not the case). A long cycle rate means cloud contamination during a cast is likely, and the cast frequently must be temporarily halted to allow the cloud to pass, which adds to the time required (of course, a low wire speed means high vertical sampling resolution).

Tethered (or free-fall) systems, in comparison, have more strengths than weaknesses:

- A. The profiler (and sometimes the reference) can be deployed away from the platform clear of any platform shading or reflections to the *in situ* light field.
- B. The profiler is not subject to wave action, but it must be properly trimmed to ensure minimal tilts during descent.
- C. A free-floating reference is not decoupled from surface motion, but engineering solutions and deployment practices can be adopted to reduce this effect.
- D. There is a direct cable connection between the instruments and the data acquisition units, so there is no complicated (hydraulic) machinery or electrical (slip ring) connection which can require long repair times in the event of a failure.
- E. The cable is usually a lighter material than steel (e.g., Kevlar® †), and is more easily damaged than the standard hydrowire used with winch systems.
- F. The instruments are usually hand lowered close to the side of the ship, so they are vulnerable to damage by wave action.
- G. Deployment and recovery can be accomplished with only two scientists which ensures a rapid cycle rate.

The latter is particularly important, because it means casts can be executed in between cloud passage and more casts can be done in a particular unit of time. It also means station scheduling can be kept informal with the ship being stopped only when the illumination conditions are optimal.

All of the radiometers, including any spares, were manufactured by Satlantic, Inc. (Halifax, Canada). The basic subcomponents of the light systems were the power and telemetry units, called DATA-100s, the series 200 Ocean Color Irradiance (OCI-200) sensors, and the series 200 Ocean Color Radiance (OCR-200) sensors. The radiometers have seven channels, which were chosen to correspond

† Kevlar is a registered trademark of E.I. du Pont de Nemours and Company, Wilmington, Delaware.

with the SeaWiFS instrument wavelengths and bandwidths (Hooker et al. 1993).

1.2.1 The AMT Instruments

SeaOPS is composed of two sets of instruments. The in-water component is composed of a downward-pointing radiance sensor (OCR-200), which measures $L_u(z, \lambda)$, an upward-pointing irradiance sensor (OCI-200), which measures $E_d(z, \lambda)$, and a downward-pointing irradiance sensor (OCI-200), which measures $E_u(z, \lambda)$. Internal tilt sensors quantify the vertical orientation (φ) of the profiler as it is lowered through the water. The above-water component, an OCI-200, is fitted to a pole on a mast and measures the incident solar irradiance above the ocean surface, $E_d(0^+, \lambda)$. A custom-built T-shaped frame is used to carry SeaOPS, which is lowered and raised through the water column by a winch; data are collected during the lowering and raising of the frame as down and up casts, respectively.

The positioning of the equipment on the SeaOPS frame was developed with a geometry that ensured the light sensors were in close proximity to one another while preventing the radiance sensor from viewing any part of the support (Fig. 1). The narrow geometry of the frame was designed to provide a minimal optical cross section. The field of view of the irradiance sensor was only influenced by the 7 mm winch wire.

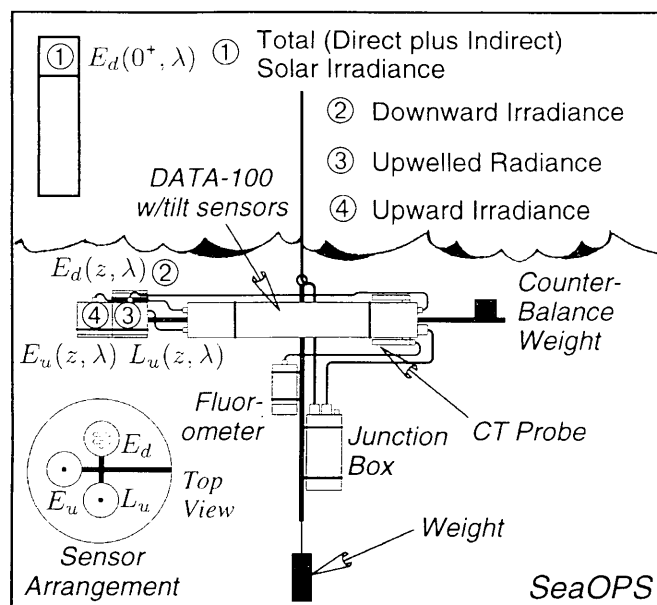


Fig. 1. A detailed layout of the SeaOPS components showing the dimensional relationships between the pieces of equipment.

Careful attention was paid to the balance of the instrument frame, even though SeaOPS had tilt and roll sensors. At the start of each cruise, the frame was trimmed with lead weights in air, accounting for the in-water weights of the sensors; final trim checks were carried out *in situ* during the first (test) station. The typical lowering and raising speed of the winch was approximately $0.20\text{--}0.25\text{ m s}^{-1}$.

For most stations, the sun was kept on the same side from which SeaOPS was deployed except if adverse sea or wind conditions prevented this. The crane used had about a 10 m reach over the side of the ship.

The LoCNESS profiler is not a new instrument per se, but instead is built up from the SeaOPS components. SeaOPS has two pairs of internal tilt sensors, one pair for when it is oriented horizontally and one pair for when it is oriented vertically for the LoCNESS configuration. In its prototype configuration, LoCNESS measured two components of the light field (Aiken et al. 1998); the DATA-100 and the two light sensors were connected in line using extension brackets with an OCR-200 at the nose (pointing downwards to measure L_u) and an OCI-200 at the tail (pointing upwards to measure E_d). The addition of weight to the nose bracket and buoyant (foam) fins to the tail bracket produced a balanced package that fell through the water column with minimum tilts (less than 2°).

The Three-Headed Optical Recorder (THOR) option allowed LoCNESS to measure the same three components of the in-water light field as SeaOPS (Fig. 2). In all configuration options, the power and telemetry cable to the profiler extended through the field of view of the irradiance sensor, but the small diameter of the cable (7 mm) minimized any negative effects on the measured light field. The irradiance incident at the sea surface was measured with a sensor installed on a mast situated above the ship's deck (often called the reference or *deck cell* measurement).

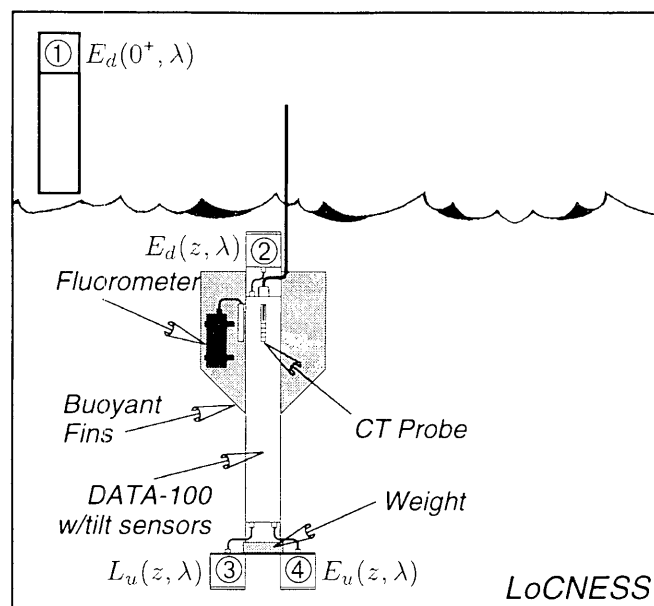


Fig. 2. A schematic of the LoCNESS profiler.

The principle advantage of LoCNESS in comparison to conventional free-fall profilers is its cost and flexibility; it can be assembled from relatively low cost components and it can be quickly reconfigured, because the radiometers used are not integral to the design. For example, the two

Table 1. Channel numbers (λ_i) and center wavelengths (in nanometers) for the radiometers used with the AMT sampling systems.

Sensor Type	SeaOPS (SO)							LoCNESS (LN)						
	λ_1	λ_2	λ_3	λ_4	λ_5	λ_6	λ_7	λ_1	λ_2	λ_3	λ_4	λ_5	λ_6	λ_7
$L_u(z)$	411.0	442.8	489.8	509.7	555.0	664.8	682.7	411.6	442.7	489.9	510.3	554.2	665.3	682.6
$E_d(z)$	411.5	442.5	489.3	509.6	555.4	665.7	683.2	411.3	442.5	489.3	509.1	554.8	666.0	682.9
$E_u(z)$	411.4	442.7	490.0	509.3	554.3	665.9	682.4	411.6	443.2	490.8	510.2	554.9	665.5	682.4
$E_d(0^+)$	411.9	443.0	489.8	511.0	555.5	665.2	683.7	411.9	443.0	489.8	511.0	555.5	665.2	683.7

different nose sensors can be replaced with two identical sensors so they can be intercompared *in situ*.

A summary of the center wavelengths for the SeaOPS and LoCNESS radiometers is given in Table 1. All of the instruments have very similar center wavelengths, and a common solar reference was used for the two systems.

1.2.2 The AAOT Instruments

The WiSPER system is permanently installed on the AAOT and is operated from a 7 m platform extension on the southeastern side of the second level. A custom-built profiling rig and the positioning of the equipment on the rig were developed with a geometry that ensures all radiometers do not view any part of the mechanical supports. The radiometers are mounted on a 1 m extension boom which displaces them from the bulk of the underwater instrumentation and puts them approximately 7.5 m from the nearest tower leg. Two taught wires anchored between the tower and the sea bottom prevent the movement of the rig out of the vertical plane defined by the wires.

The narrow geometry of the WiSPER frame was designed to provide a minimal optical cross section. The field of view of the irradiance sensor is obstructed by the power and telemetry cable as well as the stabilization wires, but all of these have very small cross sections. Careful attention was paid to the rigidity and stability of the rig, so there is no need for tilt or roll sensors.

WiSPER uses the same kind of optical sensors (the 7-channel OCR-200 and OCI-200 series of instruments) and makes the same measurements as SeaOPS: one OCI-200 to measure $E_d(z, \lambda)$, one OCR-200 to measure $L_u(z, \lambda)$, and one OCI-200 to measure $E_u(z, \lambda)$. One difference between SeaOPS and WiSPER, is the solar irradiance sensor for the latter is regularly occulted at the end of a cast to determine the diffuse (or indirect) solar irradiance, $E_i(0^+, \lambda)$.

A special kind of DATA-100, the MOR-005, provides the analog-to-digital (A/D) conversion and telemetry capability for the WiSPER instruments. The equipment is powered directly from 12 V lead-acid batteries which are stored and kept charged on the tower. WiSPER is raised and lowered using a small electrical winch. The typical lowering and raising speed of the winch is approximately 0.08 m s^{-1} . Visual sea- and sky-state observations are recorded during all casts. A schematic of the WiSPER system is shown in Fig. 3.

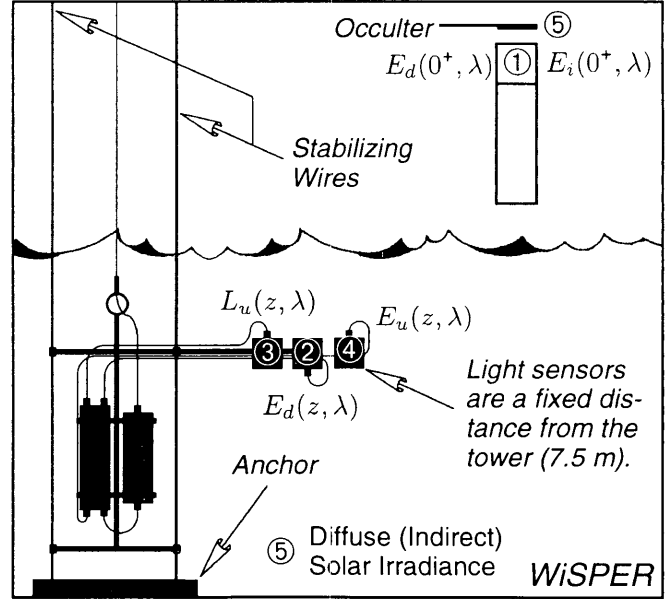


Fig. 3. The measurements made with the WiSPER system. The in-water sensors are shown in a distorted configuration, so each can be seen clearly. Their actual physical layout is similar to SeaOPS.

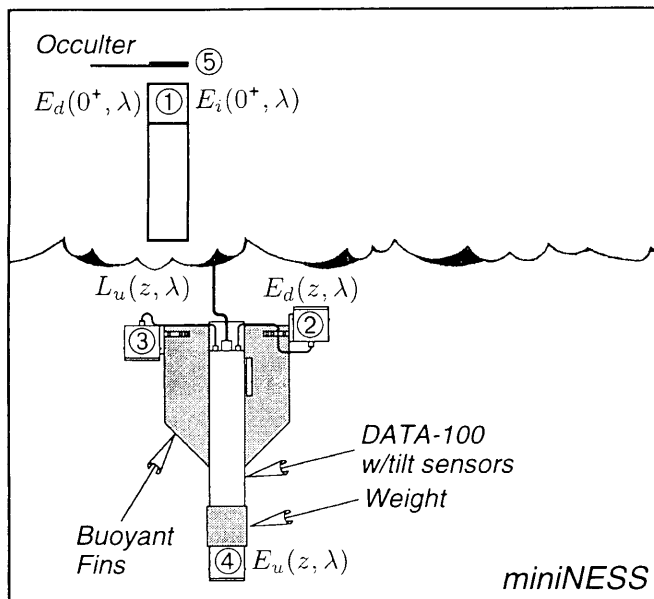
The miniNESS profiler makes the same measurements as WiSPER, except it is deployed as a tethered, free-fall package (and has internal tilt sensors). It is a variant of LoCNESS and is built with the same modular components: a DATA-100 (with 16-bit A/D converters) for power and telemetry, and 7-channel OCR-200 and OCI-200 sensors. The main difference between the LoCNESS and miniNESS profilers is the former has all of the light sensors mounted at the ends of the rocket-shaped profiler, whereas the latter has the E_d and L_u sensors mounted on the fins and E_u on the nose. An adapter is used to mount the E_u sensor on the nose (a flared metal cage can be used to protect this sensor against accidental bottom impacts).

Putting light sensors on the fins destabilizes the profiler (although, careful trimming of the profiler has regularly produced tilts less than 2°), and it makes the L_u sensor more susceptible to shading. This problem was minimized by choosing where the mechanical termination was with respect to the sensors and the sun. In general, the two sensor fins, which are 180° apart, will align perpendicular

Table 2. Channel numbers (λ_i) and center wavelengths (in nanometers) for the AAOT sampling systems.

Sensor Type	WiSPER (WP)							miniNESS (MN)						
	λ_1	λ_2	λ_3	λ_4	λ_5	λ_6	λ_7	λ_1	λ_2	λ_3	λ_4	λ_5	λ_6	λ_7
$L_u(z)$	412.3	442.8	490.5	510.8	554.9	665.8	683.9	412.5	442.2	490.9	510.3	554.5	665.4	684.0
$E_d(z)$	412.4	443.5	490.6	509.1	555.9	665.4	682.1	412.3	442.1	490.5	510.3	554.5	665.7	683.8
$E_u(z)$	412.5	442.2	490.7	509.8	554.7	664.8	683.2	412.4	443.5	490.8	509.9	554.7	664.9	683.2
	411.5	442.8	490.9	510.4	554.3	664.8	682.7	412.5	442.2	490.7	509.8	554.7	664.8	683.2
$E_d(0^+)$	411.5	442.8	489.9	510.3	554.5	664.8	683.2	411.5	442.8	489.9	510.3	554.5	664.8	683.2
	412.1	442.9	490.2	509.3	555.2	665.1	683.0	412.1	442.9	490.2	509.3	555.2	665.1	683.0

to the mechanical termination when the cable is pulled in to bring the profiler to the surface (before a profile). To minimize L_u shading, all that is required is to choose which of the other two fins should be used for the mechanical termination, so the L_u sensor aligns towards the sun. A schematic of the miniNESS profiler is shown in Fig. 4.

**Fig. 4.** The sensors and corresponding measurements of the JRC miniNESS profiler.

A summary of the center wavelengths for the WiSPER and miniNESS radiometers is given in Table 2, all of which are very similar. Multiple entries for a particular sensor type represent alternative configurations. For the solar reference measurement, both sampling systems always used the same reference.

1.3 THE DARR-00 DATABASE

The DARR-00 data processing groups participated as volunteers, so to minimize the work associated with ingesting a potentially wide variety of formats, one data format was chosen: tab-delimited files complying with the American Standard Code for Information Interchange (ASCII), i.e., standard text files with the entries separated by tabs.

Ten optical casts with supporting calibration and ancillary documentation from a diverse set of bio-optical regimes, in terms of chlorophyll *a* concentration, were chosen for four different instrument systems (for a total of 40 casts). The types of instruments were classified into two broad categories based on the deployment method used, free fall or winch and crane (20 casts for each), so the importance (if any) of deployment methods could be determined.

To further simplify the comparisons, the instruments involved were restricted to the OCR-200 and OCI-200 Atlantic series of light sensors. Restricting the data to ASCII files from one instrument series limited the data sources to the JRC and GSFC groups. The GSFC group submitted 10 casts each from SeaOPS and LoCNESS, while the JRC group submitted 10 casts each from WiSPER and miniNESS. The instruments were also classified according to the primary sampling environment involved, deep ocean or shallow coastal (20 casts for each), which correspond in a general sense to Case-1 or Case-2 conditions, respectively.

Although the submitted 40 casts covered a wide range of conditions, they did not adequately represent very clear waters, so an additional 10 casts from very low chlorophyll *a* conditions were added to the data set (Sect. 1.5). Because the participating groups were volunteering their time and effort, not all of them could accommodate the extra burden of 10 more casts, so the only groups that analyzed these extra data were the JRC and GSFC. As will be shown subsequently, this had a minimal effect on the conclusions derived from the different results.

1.3.1 The GSFC Data

The GSFC data are filed using a simple naming scheme:

MCCHDNNN.EEE,

where the encoding letters are defined as

- M A one-letter code for each major campaign (A for AMT);
- CC A two-digit sequential campaign number;
- H A single letter indicating the hosting instrument for the measurement which is based on the serial number (S/N) of the DATA-100 involved (0 for SeaOPS S/N 4, K for LoCNESS S/N 11, and L for LoCNESS S/N 4);

- D A single letter indicating the deployment direction (D for down and U for up);
- NNN A three-digit sequential cast number; and
- EEE The file extension (SH0 for 6 Hz in-water optical data, and SHM for 6 Hz solar reference data).

An inventory of all the data used for the DARR-00 activity is presented in Appendix B.

1.3.2 The JRC Data

The JRC data are also organized using a simple algorithm to set the file names:

ICCSNL.EEE,

the encoding for which is defined as

- I A one-letter code for each instrument (W for WiSPER and P for the miniNESS profiler);
- CC A two-digit sequential campaign number;
- S A single letter indicating the data type (S for station and D for dark);
- N A one-digit station number;
- L A sequential letter incremented for each cast (A for 1, B for 2, etc.); and
- EEE The file extension (MOR for WiSPER, OCP for miniNESS, and MVD for the solar reference).

1.3.3 The Data Products

Water-leaving radiance is a primary variable in the calibration and validation process, not only because it is a first-order quantity (i.e., it appears explicitly in the radiative transfer equation governing the remote sensing observations), but also because it is the central physical quantity for bio-optical studies in the upper ocean. Many variables used for the latter (e.g., $R_{rs}(\lambda)$) are derived directly from $L_W(\lambda)$ and are the input data for the algorithms used to invert ocean color observations into chlorophyll *a* concentrations.

Many in-water techniques for calculating $L_W(\lambda)$ are based on formulations well expressed by the Smith and Baker (1984) method. Variations are a consequence of the procedures (and platforms) used to acquire the data, and how the in-water data are propagated to the surface. The $L_u(\lambda, z)$ near-surface profile is usually used to compute the diffuse attenuation coefficient, $K_L(\lambda, z_0)$, as the local (around the depth z_0) slope of $\ln[L_u(\lambda, z)]$. $K_L(\lambda, z_0)$ is used to extrapolate the upwelled radiance through the upper layer to null depth. $L_W(\lambda)$ is then obtained by properly propagating the near-surface upwelling radiance, $L_u(\lambda, 0^-)$, through the air-sea interface.

The data products compared are those commonly associated with bio-optical analyses:

1. The upwelled radiance immediately below the sea surface, $L_u(0^-, \lambda)$;

2. The downward irradiance immediately below the sea surface, $E_d(0^-, \lambda)$;
3. The diffuse attenuation coefficients from the upwelling radiance and the downward irradiance profiles, $K_L(\lambda)$ and $K_d(\lambda)$, respectively;
4. The incident solar irradiance immediately above the sea surface, $E_d(0^+, \lambda)$;
5. The remote sensing reflectance, $R_{rs}(\lambda)$;
6. The normalized water-leaving radiance, $[L_W(\lambda)]_N$;
7. The upward irradiance immediately below the sea surface, $E_u(0^-)$, which is used with the upwelled radiance to derive the nadir *Q*-factor immediately below the sea surface, $Q_n(0^-, \lambda)$; and
8. Ancillary parameters like the solar zenith angle, θ , and the total chlorophyll *a* concentration, C_{Ta} , derived from the optical data.

The latter is usually determined using one of the standard ocean color (OC) algorithms (O'Reilly et al. 1998). For the DARR-00 activity, the OC2v2 algorithm is intercompared, because all of the processors used this algorithm.

Plots of calibrated optical measurements for selected casts from the JRC data set are shown in Figs. 5–7. A subset of wavelengths are shown to maintain clarity of presentation. The first file, W56S7A from WiSPER (Fig. 5), was selected to show the influence of multiple stratification on the in-water light fields. The second file, P60S4R from miniNESS (Fig. 6), is an example of the significance of surface effects, i.e., wave focusing, which is most clearly seen in the $E_d(z, \lambda)$ data. The third file, W56S1A from WiSPER (Fig. 7), shows an ideal case with no in-water extra sources of variance and very stable solar illumination.

Plots of calibrated optical measurements for selected casts from the GSFC data set are shown in Figs. 8–10. Again, a subset of wavelengths are shown to maintain clarity of presentation. The first file, A07KD025 (Fig. 8), corresponds to high chlorophyll *a* conditions ($C_{Ta} = 1.18 \text{ mg m}^{-3}$) wherein several in-water parameters that characterize the water column are confined to the upper layer: the depth of the chlorophyll maximum (DCM) as estimated from the fluorometer data is 37 m, the mixed layer depth (MLD) is 29 m, and the one-percent light level (OLL), based on the decay of the surface PAR value, is 38 m. The second file, A07KD040 (Fig. 9), is an example of a cast in very clear water ($C_{Ta} = 0.08 \text{ mg m}^{-3}$) with typical deep ocean water properties: the DCM is 139 m, the MLD is 121 m, and the OLL is 124 m. The last file, A060D033 (Fig. 10), is presented to show a case with abnormally large vessel motion in eutrophic waters ($C_{Ta} = 2.43 \text{ mg m}^{-3}$) during otherwise very good conditions.

1.4 DATA ANALYSIS METHODS

In this study, no one data processing system is assumed to be more correct than another, so an unbiased parameter is needed to compare the various methods. The average unbiased percent difference (UPD) between two data

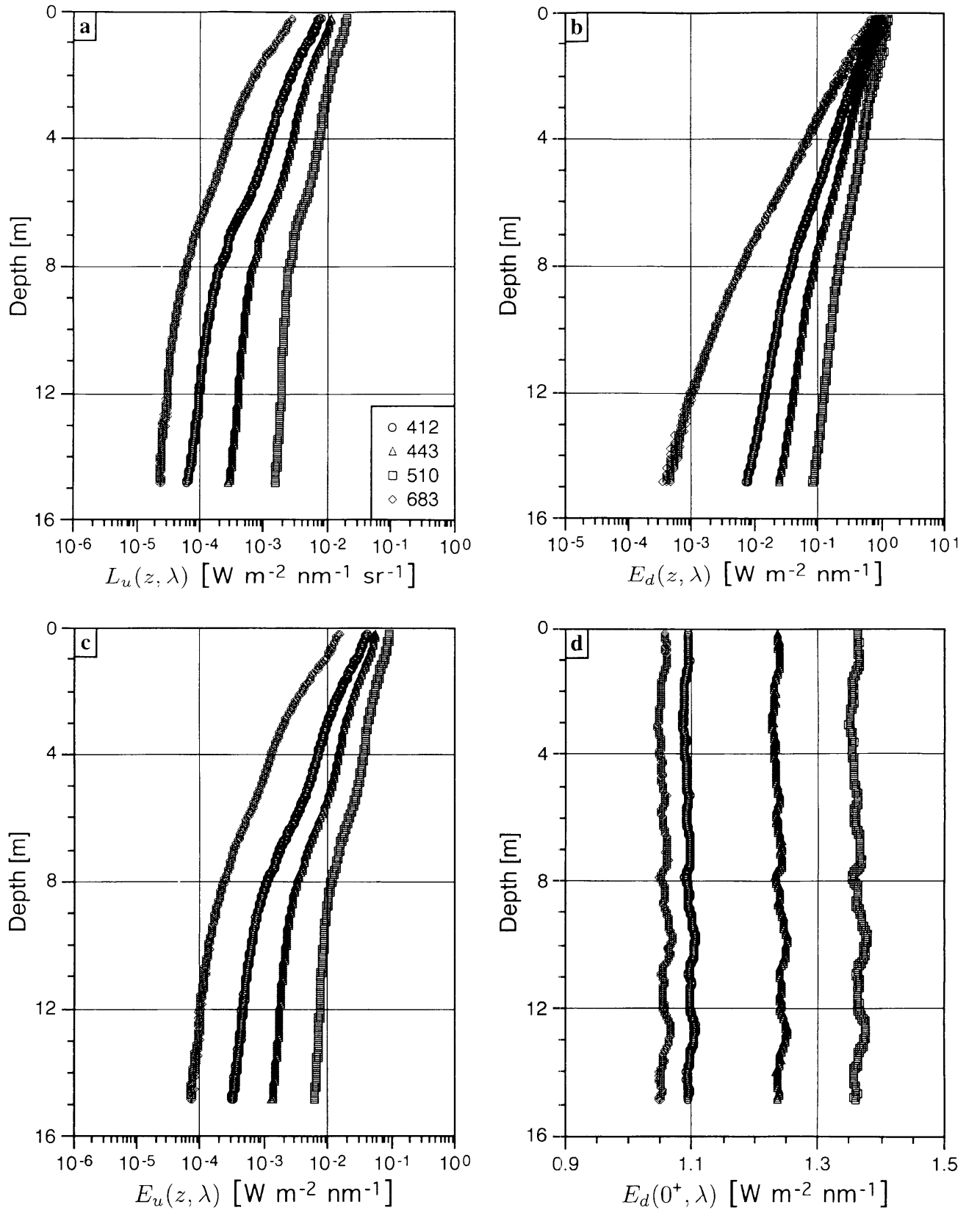


Fig. 5. The in-water and solar reference data for W56S7A.MOR and W56S7A.MVD, respectively: a) $L_u(z, \lambda)$, b) $E_d(z, \lambda)$, c) $E_u(z, \lambda)$, and d) $E_d(0^+, \lambda)$, shown as a function of the corresponding z value rather than t .

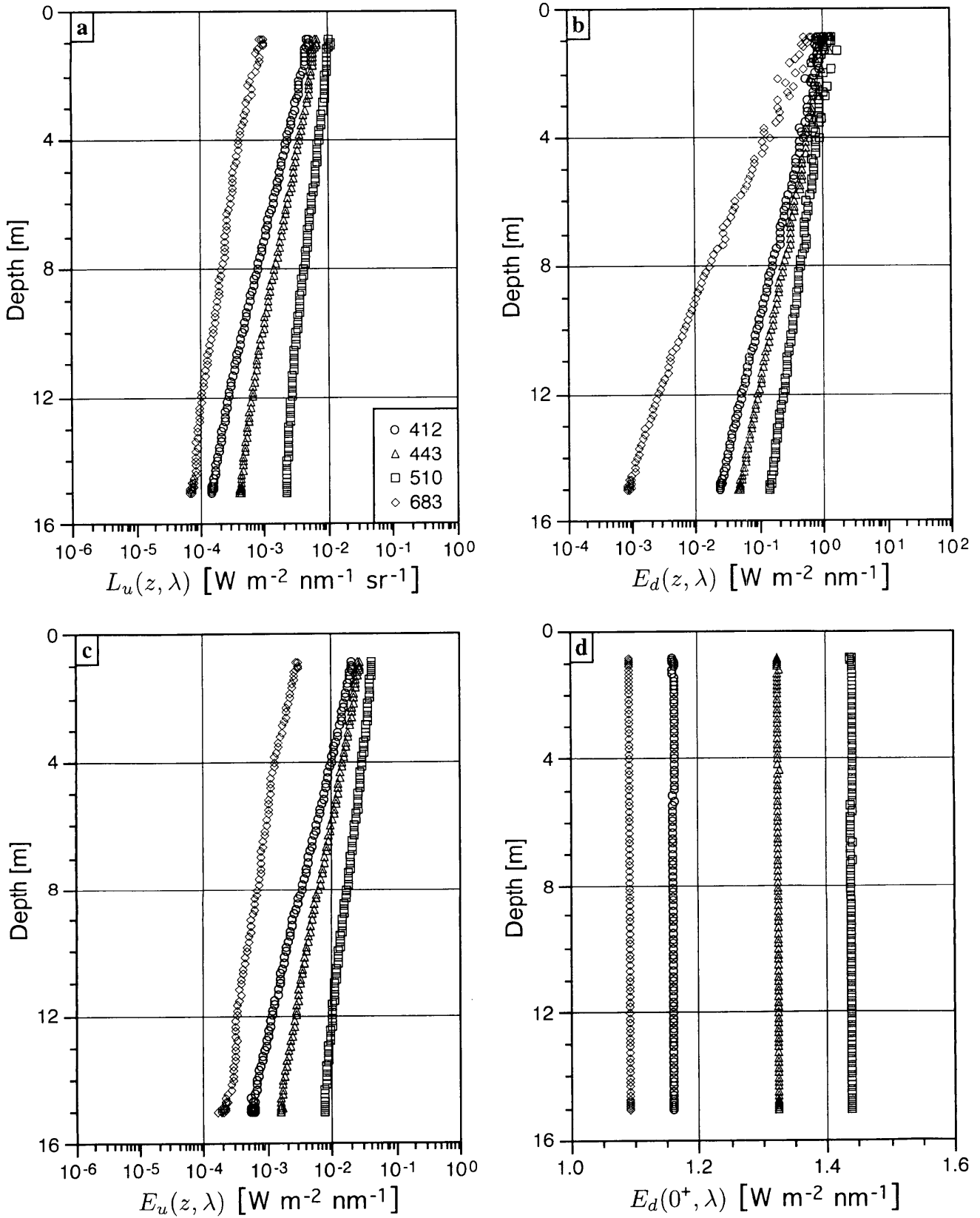


Fig. 6. The in-water and solar reference data collected for P60S4R.OCP and P60S4R.MVD, respectively: a) $L_u(z, \lambda)$, b) $E_d(z, \lambda)$, c) $E_u(z, \lambda)$, and d) $E_d(0^+, \lambda)$.

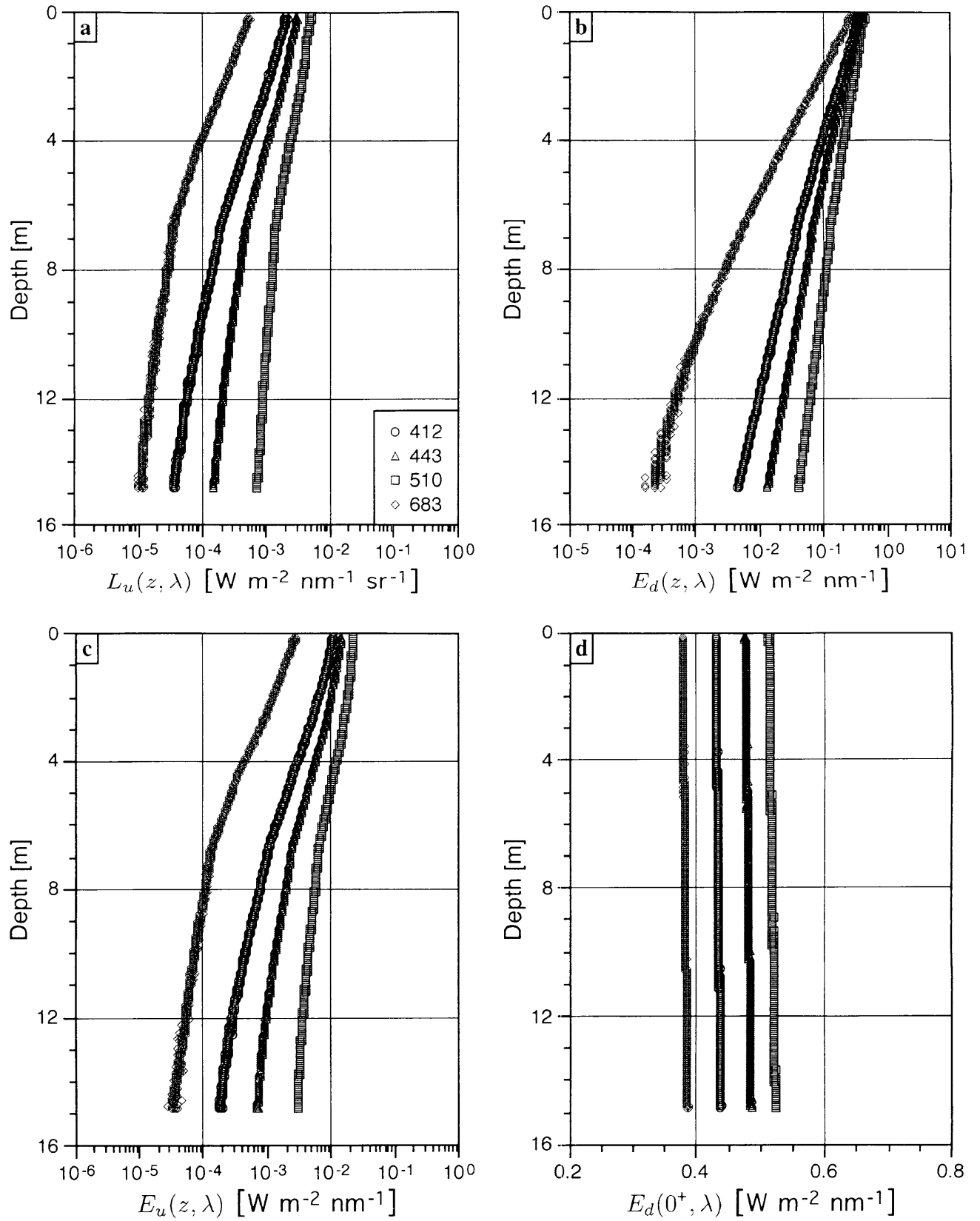


Fig. 7. The in-water and solar reference data collected for W56S1A.MOR and W56S1A.MVD, respectively: a) $L_u(z, \lambda)$, b) $E_d(z, \lambda)$, c) $E_u(z, \lambda)$, and d) $E_d(0^+, \lambda)$.

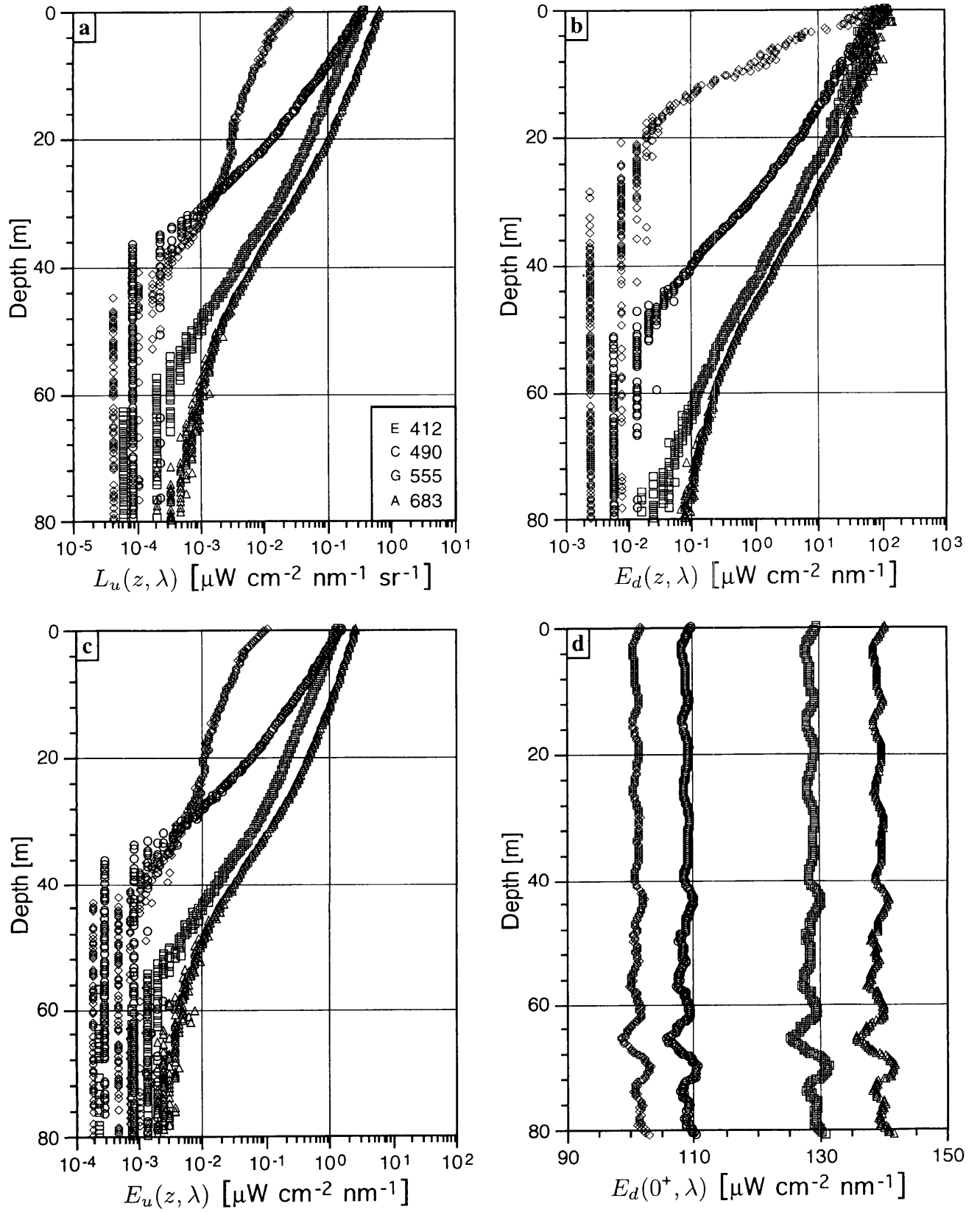


Fig. 8. The in-water and solar reference data collected for A07KD025.SH0 and A07KD025.SHM, respectively: a) $L_u(z, \lambda)$, b) $E_d(z, \lambda)$, c) $E_u(z, \lambda)$, and d) $E_d(0^+, \lambda)$.

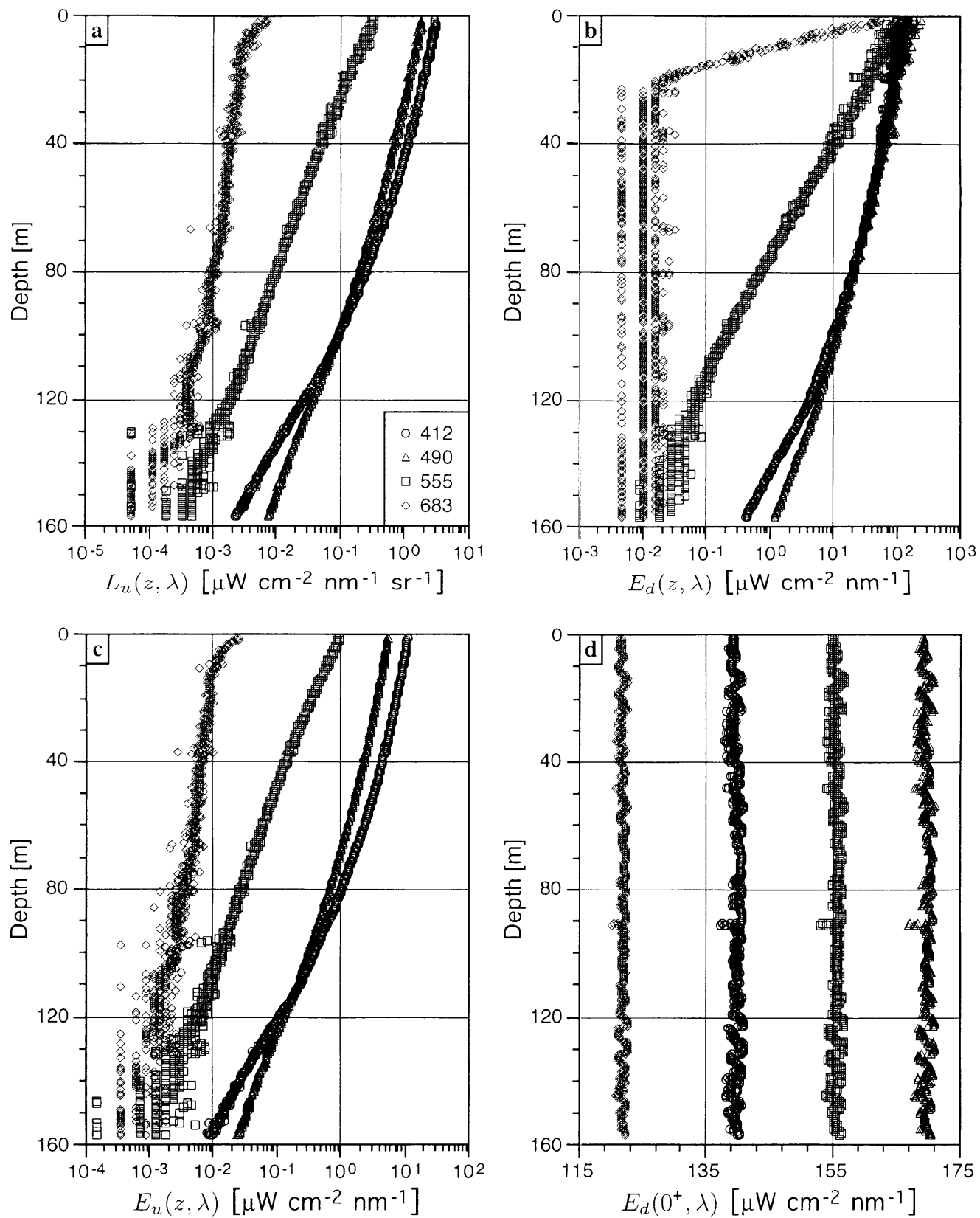


Fig. 9. The in-water and solar reference data collected for A07KD040.SH0 and A07KD040.SHM, respectively: a) $L_u(z, \lambda)$, b) $E_d(z, \lambda)$, c) $E_u(z, \lambda)$, and d) $E_d(0^+, \lambda)$.

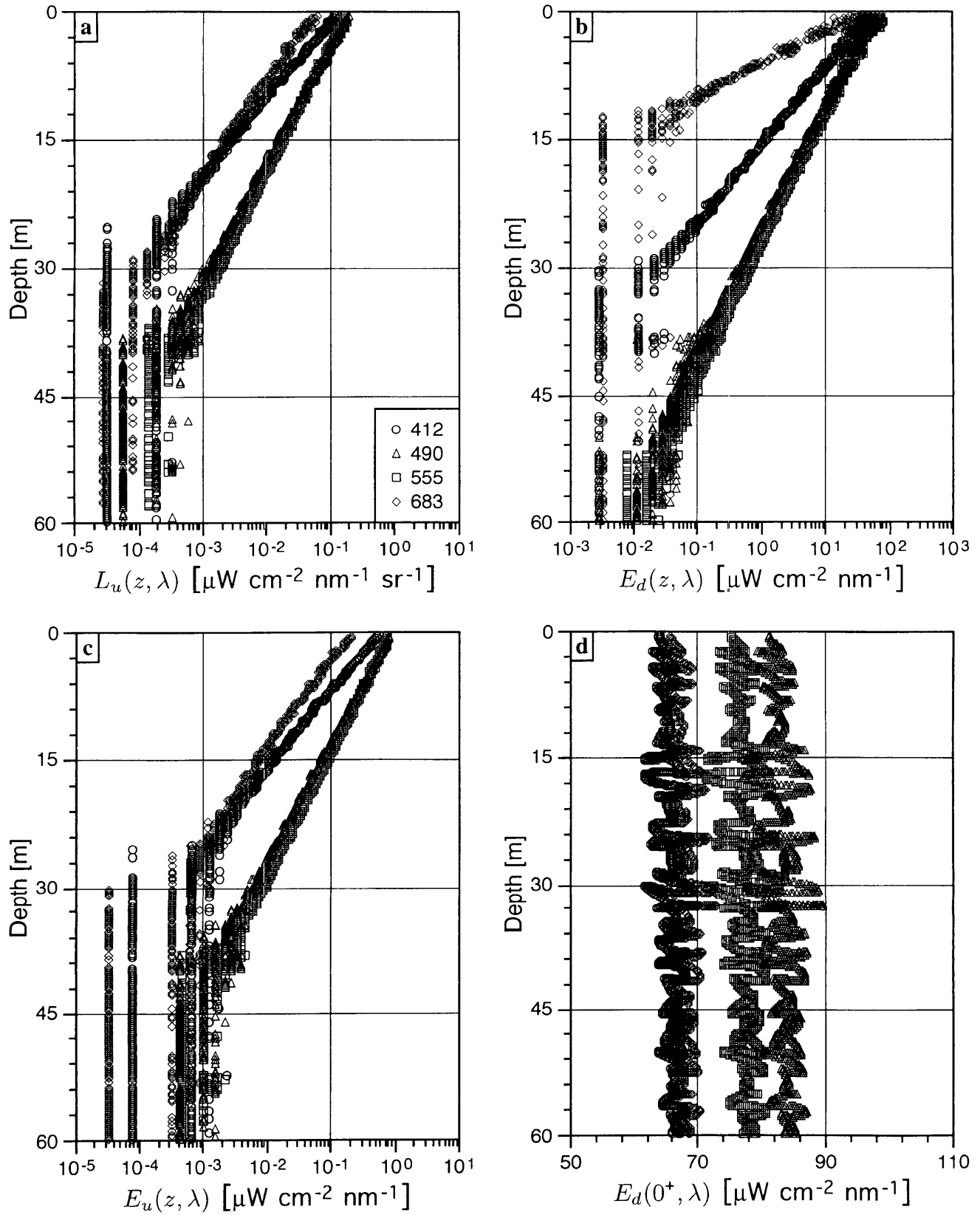


Fig. 10. The in-water and solar reference data collected for A060D033.SH0 and A060D033.SHM, respectively: a) $L_u(z, \lambda)$, b) $E_d(z, \lambda)$, c) $E_u(z, \lambda)$, and d) $E_d(0^+, \lambda)$.

products \mathfrak{F}^A and \mathfrak{F}^B was computed as:

$$\bar{\psi}_{\mathfrak{F}}^{AB}(\lambda) = \frac{200}{N_m} \sum_{i=1}^{N_m} \frac{|\mathfrak{F}^A(\lambda, t_i) - \mathfrak{F}^B(\lambda, t_i)|}{\mathfrak{F}^A(\lambda, t_i) + \mathfrak{F}^B(\lambda, t_i)} \quad (1)$$

where t_i is the time associated with the sample (the i index selects a sample), N_m is the number of measurements being compared, and \mathfrak{F} represents the data product, $L_u(0^-)$, $E_d(0^-)$, K_d , etc. The A and B codes identify the processors involved: J for JRC, G for GSFC, and S for Satlantic. The UPD between the upwelled radiances (at null depth) estimated with the JRC and GSFC processors, for example, is $\psi_{L_u}^{JG}(\lambda)$ and represents the uncertainty between the two processors in estimating $L_u(0^-, \lambda)$.

Spectral averages of the UPD are calculated by including a summation in (1) over the requisite number of spectral bands, N_b :

$$\Psi_{\mathfrak{F}}^{AB} = \frac{1}{N_b} \sum_{j=1}^{N_b} \bar{\psi}_{\mathfrak{F}}^{AB}(\lambda_j). \quad (2)$$

Although several schemes can be devised for spectral averages, the ones considered here are as follows: the average of the blue-green wavelengths, $\Psi_{\mathfrak{F}}^{AB}(\lambda_{1-5})$, the average of the red wavelengths, $\Psi_{\mathfrak{F}}^{AB}(\lambda_{6-7})$, and the average of all the wavelengths, $\Psi_{\mathfrak{F}}^{AB}(\lambda_{1-7})$.

The primary interest in this study are spectral estimates of water-leaving radiance, but the most frequently used ocean color algorithms, OC2v2 (O'Reilly et al. 1998), uses band ratios, e.g., the 490 and 555 nm bands. Consequently, another important parameter for the above-water analyses presented here is the UPD for a band ratio:

$$\Phi_{\mathfrak{B}}^{AB}(\lambda_{k/l}) = \frac{200}{N_m} \sum_{i=1}^{N_m} \frac{|\mathfrak{B}^A(\lambda_{k/l}, t_i) - \mathfrak{B}^B(\lambda_{k/l}, t_i)|}{\mathfrak{B}^A(\lambda_{k/l}, t_i) + \mathfrak{B}^B(\lambda_{k/l}, t_i)} \quad (3)$$

where \mathfrak{B} is the band ratio of a particular data product for wavelengths k and l (the data product for wavelength k is divided by the data product for wavelength l). For this study, the only band ratio presented is between 490 and 555 nm. For example, the average band ratio results for $L_u(490)$ and $L_u(555)$ for the JRC and GSFC processors is denoted as $\Phi_{L_u}^{JG}(\lambda_{3/5})$.

Most results are presented in tables as a function of data products and method codes. In these cases, a shorthand notation is used for spectral averages and band ratios:

- Ψ_{1-7} The average of all (seven) wavelengths, 412–683 nm;
- Ψ_{1-5} The average of the (five) wavelengths in the blue-green part of the spectrum, 412–555 nm;
- Ψ_{6-7} The average of the (two) wavelengths in the red part of the spectrum, 665–683 nm; and
- $\Phi_{3/5}$ The average of the band-ratio results calculated for 490 and 555 nm (bands three and five, respectively).

The processing of the data does not always end with the calculation of $L_w(\lambda)$. The WiSPER and miniNESS data, for example, are collected in the proximity of a large structure sited in shallow water, so there are other processing aspects which need to be considered:

1. Instrument self-shading, which affects all in-water instruments, particularly in the red domain where water absorption is elevated;
2. Bottom reflection, which can be important in shallow water; and
3. Platform shading, which can effect any instrument deployed in close proximity to a large structure (e.g., a research vessel or offshore tower).

Correction terms for these effects are generally not applied, because they require accurate knowledge of several atmospheric and marine optical parameters, and they may require extensive computations.

1.5 RESULTS-STANDARD (V1)

The first results presented are the comparisons derived from the processing of data using standard options for each processor, i.e., those procedures normally employed by the processing groups. These results are also referred to as the version 1 (V1) results, and subsequent changes to the processors are identified by increasing version numbers.

In addition to the instrument types (SO, LN, WP, and MN), the data sets can be naturally divided into a variety of categories depending on the sampling location, the deployment methodology, and the total chlorophyll a concentration. The former two are encoded as follows:

- DO For the deep ocean data (SO and LN);
- SC For the shallow coastal data (WP and MN);
- WC For the winch and crane data (SO and WP); and
- FF For the free-fall data (LN and MN).

The deep ocean data are all from Case-1 conditions, and the shallow coastal data are from Case-2 conditions or from water near the threshold between Case-1 and Case-2 in terms of the Loisel and Morel (1998) classification scheme.

The C_{Ta} (in milligrams per cubic meter) is used to separate the data into three concentration (or trophic) regimes, which are encoded as follows:

- ET For the eutrophic regime ($C_{Ta} > 1$);
- MT For the mesotrophic regime ($0.1 \leq C_{Ta} \leq 1$); and
- OT For the oligotrophic regime ($C_{Ta} < 0.1$).

These groups are a mixture of all instrument types, except all the oligotrophic data come from the LN data set.

The various combinations of processor intercomparisons are identified by two-letter codes:

- JG For the JRC and GSFC processors;
- JS For the JRC and Satlantic processors; and
- GS For the GSFC and Satlantic processors.

As will be shown below, the JRC and GSFC processors are architecturally similar. Unlike the Satlantic processor, they are also maintained by individual investigators with narrowly defined user groups, so they can be quickly modified without negatively effecting a large community.

The contribution of each instrument type to the concentration regimes is presented in Table 3, which is divided into two groups given by the subtotal and total partitions. The former represents the data used for intercomparing all the processors, whereas the latter represents the additional data beyond the original 40 casts to ensure a reasonable number of samples in each concentration regime (which were only processed by the JRC and GSFC groups).

Table 3. The number of casts from each instrument type within each concentration regime. Also shown are the sampling location and deployment method codes for each instrument, as well as the groups that processed the indicated casts.

Instrument	Groups	ET	MT	OT
SO (DO and WC)	J G S	8	2	0
LN (DO and FF)	J G S	1	6	3
WP (SC and WC)	J G S	3	7	0
MN (SC and FF)	J G S	3	7	0
Original (40-Cast) Subtotal		15	22	3
SO (DO and WC)	J G	0	0	3
LN (DO and FF)	J G	0	0	7
Extended (50-Cast) Total		15	22	13

The distribution of the instrument types within the various categories shown in Table 3 will produce biases in some of the results. For example, the majority of the shallow coastal data are in the mesotrophic regime, which also means the majority of these data are for stable references. These biases are not necessarily detrimental to the comparison process, because they allow a quantitative assessment of the differences between the instrument types, sampling locations, and deployment methods. It is important to remember these biases, however, because they do mitigate the application of the results to broader generalizations.

The various processing options that can influence the final determination of $L_W(\lambda)$ can have a far-reaching effect on bio-optical analyses. Five different processing options are considered in the presentation of the results:

1. Tilt filtering (this is usually a simple threshold—if the tilt of the instrument exceeds a particular value, the data are not used);
2. $E_d(0^+)$ normalization (to account for the influence of changing illumination conditions during the profile, some processors normalize the in-water light data by $E_d(0^+, t)/E_d(0^+, t_0)$, where t_0 is the start time of the profile);
3. The type of linear fit used in the extrapolation process (simple least-squares regressions are common,

but some processors use routines wherein any data with a large variance are weighted the least);

4. Whether or not data are statistically filtered, i.e., any point more than a specified number of standard deviations ($n\sigma$) from the linear regression is considered a so-called *outlier* and is ignored (this is a more extreme form of weighted fitting); and
5. The limits of the extrapolation interval, i.e., the upper and lower depths.

For the three processors, the standard options used for each are as follows:

- J Tilt filtering (5° threshold), $E_d(0^+)$ normalization, 3σ filter for outliers, least-squares (unweighted) linear fit, and extrapolation depths chosen to ensure all wavelengths are well parameterized;
- G No tilt filtering, no $E_d(0^+)$ normalization, not filtered for outliers, least-squares (unweighted) linear fit, and extrapolation depths chosen so the blue-green wavelengths are optimally parameterized; and
- S Tilt filtering (5° threshold), no $E_d(0^+)$ normalization, filtered for outliers, least-squares (unweighted) linear fit, and near-surface extrapolation based on binned data.

All of the results presented in this section are based on these standard processing options.

1.5.1 $L_u(0^-)$

All the DARR-00 processors calculated $L_W(\lambda)$ from profiles of upwelled spectral radiance, $L_u(z, \lambda)$, so for this study, the most important parameter is arguably $L_u(0^-, \lambda)$, i.e., the null depth estimation of the upwelling radiance. Unfortunately, with the instruments and deployment methodologies currently available, it is not practical to measure $L_u(0^-, \lambda)$ precisely at an infinitesimal depth below the surface. A profile of $L_u(z, \lambda)$ must, therefore, be measured over the upper few optical depths with sufficient accuracy to determine $K_L(z, \lambda)$ for $L_u(z, \lambda)$, and to propagate $L_u(z, \lambda)$ to the surface over a near-surface depth interval.

The percent differences (or uncertainties) between the three data processors in the calculation of $L_u(0^-, \lambda)$ is presented in Table 4†. There are several aspects of the intercomparisons which are worth noting:

- a) The smallest uncertainties are associated with the JRC and GSFC intercomparisons (the Satlantic intercomparisons are, on average, a little more than twice as large);

† In all of the results tables, the intercomparisons of the data processors based on the four instrument types (SO, LN, WP, and MN), are for the original 40-cast data set (usually the top three boxes of information in the table, but sometimes only the top box). The JG comparisons of different sampling locations (DO and SC), deployment methods (WC and FF), and concentration regimes (OT, MT, and ET), are for the extended 50-cast data set, and are always the bottom two boxes of information.

Table 4. A summary of the $\bar{\psi}$, Ψ , and Φ values for the computation of $L_u(0^-, \lambda)$.

Comparison	$\bar{\psi}(412)$	$\bar{\psi}(443)$	$\bar{\psi}(490)$	$\bar{\psi}(510)$	$\bar{\psi}(555)$	$\bar{\psi}(665)$	$\bar{\psi}(683)$	Ψ_{1-5}	Ψ_{6-7}	Ψ_{1-7}	$\Phi_{3/5}$
SO JG (40)	3.7	4.0	3.2	3.0	2.6	26.4	11.7	3.3	19.0	7.8	1.0
LN JG (40)	3.6	3.0	2.6	3.0	4.0	23.9	22.9	3.2	23.4	9.0	2.0
WP JG (40)	1.0	1.0	0.9	0.9	0.9	2.4	3.2	0.9	2.8	1.5	0.2
MN JG (40)	2.6	2.4	1.9	1.9	2.0	5.5	7.3	2.2	6.4	3.4	0.4
Average	2.7	2.6	2.1	2.2	2.4	14.6	11.3	2.4	12.9	5.4	0.9
SO JS (40)	12.8	24.0	9.7	9.3	8.5	48.7	31.3	12.9	41.3	20.6	2.0
LN JS (40)	7.0	6.4	5.4	5.6	6.9	43.1	42.2	6.3	41.0	16.1	6.6
WP JS (40)	1.6	1.3	1.0	1.1	1.2	3.7	4.9	1.3	4.3	2.1	0.2
MN JS (40)	6.9	5.7	4.0	3.9	3.8	10.8	10.2	4.9	10.5	6.5	0.3
Average	7.1	9.3	5.1	5.0	5.1	26.6	22.1	6.3	24.3	11.3	2.3
SO GS (40)	9.7	21.4	7.8	7.4	7.2	31.0	26.8	10.7	28.9	15.9	1.6
LN GS (40)	8.3	7.5	6.6	6.9	8.9	46.8	45.0	7.6	44.3	18.0	7.5
WP GS (40)	2.0	1.8	1.5	1.5	1.6	4.0	5.0	1.7	4.5	2.5	0.3
MN GS (40)	7.5	6.0	4.0	3.8	3.7	10.8	10.1	5.0	10.4	6.6	0.7
Average	6.9	9.2	5.0	4.9	5.3	23.1	21.7	6.3	22.0	10.7	2.5
DO JG (50)	2.9	2.8	2.5	2.6	3.0	25.9	21.9	2.7	23.9	8.8	1.5
SC JG (50)	1.8	1.7	1.4	1.4	1.4	4.0	5.2	1.5	4.6	2.4	0.3
WC JG (50)	2.1	2.3	1.8	1.8	1.7	18.5	12.7	1.9	15.6	5.8	0.6
FF JG (50)	2.7	2.5	2.2	2.3	3.0	16.0	17.4	2.5	16.7	6.6	1.4
OT JG (50)	1.6	1.5	1.6	1.8	2.7	25.5	28.7	1.8	27.1	9.1	1.8
MT JG (50)	2.1	2.0	1.8	1.9	2.4	13.4	12.7	2.0	13.0	5.2	0.8
ET JG (50)	3.7	3.7	2.7	2.6	2.2	15.5	7.4	3.0	11.4	5.4	0.7

Table 5. A summary of the $\bar{\psi}$, Ψ , and Φ values for the computation of $E_d(0^-, \lambda)$.

Comparison	$\bar{\psi}(412)$	$\bar{\psi}(443)$	$\bar{\psi}(490)$	$\bar{\psi}(510)$	$\bar{\psi}(555)$	$\bar{\psi}(665)$	$\bar{\psi}(683)$	Ψ_{1-5}	Ψ_{6-7}	Ψ_{1-7}	$\Phi_{3/5}$
SO JG (40)	4.4	4.8	4.7	4.9	5.5	8.6	18.0	4.9	13.3	7.3	1.6
LN JG (40)	6.5	7.9	5.7	6.4	8.3	20.3	24.3	7.0	22.3	11.4	4.3
WP JG (40)	1.0	0.8	0.8	1.0	0.9	1.5	1.6	0.9	1.5	1.1	0.7
MN JG (40)	1.7	1.5	2.2	2.3	1.8	2.7	1.9	1.9	2.3	2.0	1.1
Average	3.4	3.8	3.4	3.7	4.1	8.3	11.5	3.7	9.9	5.4	1.9
SO JS (40)	10.3	12.1	12.5	12.2	12.7	41.8	43.7	12.0	47.6	19.5	2.3
LN JS (40)	22.2	20.2	21.0	20.9	22.2	73.9	64.8	21.3	67.1	34.1	7.3
WP JS (40)	4.0	3.9	3.8	3.5	5.6	5.4	5.2	4.2	5.3	4.5	3.5
MN JS (40)	4.7	4.4	3.3	3.8	3.2	9.9	10.2	3.9	10.1	5.7	1.5
Average	10.3	10.2	10.1	10.1	10.9	32.8	31.0	10.3	32.5	15.9	3.7
SO GS (40)	7.5	9.1	9.8	9.7	10.0	35.5	34.3	9.2	39.9	15.6	1.9
LN GS (40)	26.4	25.0	23.9	23.9	28.6	80.7	76.8	25.5	77.5	40.1	10.3
WP GS (40)	3.8	4.3	4.0	3.7	5.9	5.8	5.9	4.3	5.8	4.8	3.2
MN GS (40)	5.4	5.1	4.2	4.4	4.7	11.2	10.8	4.8	11.0	6.5	2.3
Average	10.8	10.9	10.5	10.4	12.3	33.3	32.0	11.0	33.5	16.8	4.4
DO JG (50)	6.6	7.5	7.0	7.1	8.1	15.5	22.9	7.3	19.2	10.7	2.5
SC JG (50)	1.3	1.2	1.5	1.6	1.3	2.1	1.7	1.4	1.9	1.5	0.9
WC JG (50)	2.8	3.0	3.1	3.2	3.3	5.7	14.2	3.1	10.0	5.1	1.1
FF JG (50)	5.9	6.7	6.2	6.4	7.2	14.0	14.6	6.5	14.3	8.7	2.5
OT JG (50)	8.5	9.6	9.7	9.0	9.7	16.5	24.2	9.3	20.4	12.5	1.5
MT JG (50)	3.2	2.8	3.4	3.9	4.1	8.5	8.7	3.5	8.6	4.9	2.0
ET JG (50)	2.8	4.2	2.5	2.9	3.5	7.1	14.4	3.2	10.8	5.4	1.9

- b) All of the intercomparisons have maximum uncertainties in the red part of the spectrum (665 nm), with minimal uncertainties in the blue-green domain (490–510 nm) which increase towards the blue (412–443 nm);
- c) The band-ratio results are the smallest uncertainties (except for some of the Satlantic intercomparisons);
- d) The shallow coastal data (particularly the WiSPER data) have smaller uncertainties than the deep ocean data (most notably in the red wavelengths); and
- e) As a function of increasing chlorophyll *a* concentration (OT to MT to ET), there is a general increase in uncertainties in the blue-green part of the spectrum, but a decrease in the red wavelengths, and a decrease in the band-ratio uncertainties.

In terms of the desired 2.5% intercomparison objective, there are several cases where this threshold is satisfied. For the Satlantic processor, only the blue-green WP uncertainties and some of the band-ratio uncertainties are below 2.5%—most of the results are, on average, significantly above the threshold. For the JRC and GSFC processors, all of the WP, and many of the MN uncertainties, are below 2.5%, as are all of the band-ratio uncertainties. In addition, many of the shallow coastal plus winch and crane average results, as well as the oligotrophic and mesotrophic results, are to within 2.5% in the blue-green wavelengths, but all the red wavelengths results are above the 2.5% threshold.

1.5.2 $E_d(0^-)$

Profiles of the downward spectral irradiance, $E_d(z, \lambda)$, are required to compute the diffuse attenuation coefficient, $K_d(z, \lambda)$, and the irradiance reflectance, $R(\lambda)$. As with $L_u(0^-, \lambda)$, $E_d(0^-, \lambda)$ is usually determined by extrapolation over a near-surface depth interval from the profile data, in this case, $E_d(z, \lambda)$. The percent differences between the three data processors in the calculation of $E_d(0^-, \lambda)$ is presented in Table 5. The results partition immediately into two groups, irrespective of the processors being compared: a) the best results are associated with a stable reference (WP, MN, and SC), and b) the worst results are associated with an unstabilized reference (SO, LN, and DO).

The uncertainties associated with the Satlantic processor are significantly higher (on average by a factor of 3) than the intercomparisons between the JRC and GSFC processors, the differences in the red wavelengths are higher than the blue and green by more than a factor of 2 (on average), and the band-ratio uncertainties are always smaller than the individual wavelengths. In terms of the 2.5% threshold, the JG uncertainties for the shallow coastal data (WP, MN, and SC) are almost always to within 2.5%.

Regardless of the processors being intercompared, the SO and LN (DO) data are always associated with higher uncertainties, with the latter being the highest. When

coupled with the aforementioned shallow coastal data results, this produces very good results for the WC and SC data categories (the latter are always to within 2.5%), and poorer results for the DO and FF categories (which are only to within 2.5% for the band-ratio results). The uneven distribution of instrument types and deployment methods results in a distribution as a function of concentration regimes which is hard to interpret. The ET data have the smallest differences while the OT data have the largest, but this is because the former are dominated by the SC systems and the latter by the DO systems.

The overall poorer results obtained with the deep ocean data (SO and LN) is a consequence of two factors. First, most of these data are in clear water, so wave focusing effects can substantially influence where the top of the extrapolation interval is chosen (the greater vertical resolution of the SO data helps reduce this effect). Second, the data are from areas with deep mixed layers, so the bottom of the extrapolation interval is less constrained than that encountered in the shallow coastal environment. Taken together, these two factors can result in substantially different top and bottom depth intervals from different operators. If the number of points differ substantially and the total possible number of points in the extrapolation interval is not very large (possible with the high descent rates of free-fall instruments), this will effect the extrapolation process and, thus, the final $E_d(0^-, \lambda)$ estimate.

This point is well quantified by considering the average number of points in the extrapolation ranges for the JRC and GSFC processing (\bar{N}_J and \bar{N}_G , respectively) of the SO, LN, WP, and MN data:

$$\text{SO } \bar{N}_J = 214 \text{ and } \bar{N}_G = 345;$$

$$\text{LN } \bar{N}_J = 39 \text{ and } \bar{N}_G = 68;$$

$$\text{WP } \bar{N}_J = 208 \text{ and } \bar{N}_G = 216; \text{ and}$$

$$\text{MN } \bar{N}_J = 20 \text{ and } \bar{N}_G = 24.$$

The percent differences for these data (using the largest value as the reference number) are as follows: 38% (SO), 43% (LN), 4% (WP), and 14% (MN). The ranking of the JG results in terms of smallest-to-largest average percent differences is WP, MN, SO, and LN—so, the quality of the intercomparison is well correlated with how similarly the extrapolation intervals are defined.

Although it is easy to understand why the type of reference being used would influence the intercomparison of $E_d(0^+, \lambda)$ values, it is not so obvious as to why it influences the $E_d(0^-, \lambda)$ intercomparisons. The reason is a consequence of how the two variables are normally used during data processing. For most processors, the $E_d(0^-, \lambda)$ estimate from the in-water profile is properly adjusted for the influence of the air-sea interface and then compared with the above-water measurement of $E_d(0^+, \lambda)$. The two should agree to within a few percent, and in most circumstances, alternative (but valid) processing options are tried until they do. Consequently, there is usually a *steering* effect of the solar reference data on the estimation

Table 6. A summary of the $\bar{\psi}$, Ψ , and Φ values for the computation of $K_d(\lambda)$.

Comparison	$\bar{\psi}(412)$	$\bar{\psi}(443)$	$\bar{\psi}(490)$	$\bar{\psi}(510)$	$\bar{\psi}(555)$	$\bar{\psi}(665)$	$\bar{\psi}(683)$	Ψ_{1-5}	Ψ_{6-7}	Ψ_{1-7}	$\Phi_{3/5}$
SO JG (40)	3.6	4.9	7.5	7.8	7.7	4.1	7.3	6.3	5.7	6.1	3.1
LN JG (40)	27.7	32.9	27.2	18.0	25.6	8.5	9.7	34.7	9.1	22.8	21.2
WP JG (40)	2.4	2.4	3.7	4.4	4.8	1.8	1.9	3.5	1.8	3.1	3.4
MN JG (40)	4.0	4.5	11.6	15.3	11.0	3.0	2.2	9.3	2.6	7.4	3.2
Average	9.4	11.2	12.5	11.4	12.3	4.3	5.3	13.5	4.8	9.8	7.7
SO JS (40)	7.7	10.8	15.1	14.9	14.4	7.8	9.0	12.6	9.8	11.3	3.1
LN JS (40)	50.3	48.2	65.8	61.1	40.0	40.6	26.2	56.0	34.5	49.8	45.3
WP JS (40)	6.5	10.8	16.1	21.3	19.4	6.0	5.7	15.3	5.9	12.5	6.5
MN JS (40)	4.9	7.7	11.5	15.1	10.6	4.8	3.8	10.0	4.3	8.3	6.0
Average	17.4	19.4	27.1	28.1	21.1	14.8	11.2	23.5	13.6	20.5	15.2
SO GS (40)	5.2	6.9	9.5	9.3	9.3	6.2	7.6	8.0	8.1	7.7	1.5
LN GS (40)	58.7	51.5	57.5	55.3	42.7	38.2	29.5	56.5	35.7	51.3	52.9
WP GS (40)	7.5	12.1	17.5	24.3	22.5	7.2	6.6	17.3	6.9	14.1	6.2
MN GS (40)	7.8	9.5	18.8	23.5	18.0	5.4	4.4	15.5	4.9	12.5	8.0
Average	19.8	20.0	25.8	28.1	23.1	14.3	12.0	24.3	13.9	21.4	17.1
DO JG (50)	29.7	35.3	34.4	23.3	20.0	7.3	9.7	31.2	8.5	23.2	23.6
SC JG (50)	3.2	3.4	7.7	9.8	7.9	2.4	2.0	6.4	2.2	5.2	3.3
WC JG (50)	8.3	10.8	13.1	9.0	7.4	3.1	6.6	9.7	4.9	8.3	9.8
FF JG (50)	28.2	32.5	32.7	25.5	21.8	7.2	6.7	31.2	7.0	22.5	20.2
OT JG (50)	56.9	67.4	64.6	39.3	24.3	8.2	10.9	50.5	9.6	38.8	44.6
MT JG (50)	7.1	6.5	11.6	12.9	16.2	4.6	4.2	15.3	4.4	10.1	4.8
ET JG (50)	2.5	5.3	4.5	6.1	5.6	3.9	6.5	4.8	5.2	4.9	4.7

Table 7. A summary of the $\bar{\psi}$, Ψ , and Φ values for the computation of $K_L(\lambda)$.

Comparison	$\bar{\psi}(412)$	$\bar{\psi}(443)$	$\bar{\psi}(490)$	$\bar{\psi}(510)$	$\bar{\psi}(555)$	$\bar{\psi}(665)$	$\bar{\psi}(683)$	Ψ_{1-5}	Ψ_{6-7}	Ψ_{1-7}	$\Phi_{3/5}$
SO JG (40)	2.8	3.8	4.3	4.2	3.9	23.8	16.1	3.8	19.9	8.4	1.1
LN JG (40)	13.4	12.4	14.1	13.0	12.0	36.4	44.0	13.0	40.2	20.8	7.1
WP JG (40)	2.3	2.9	3.7	3.9	4.3	3.5	5.9	3.4	4.7	3.8	0.9
MN JG (40)	4.4	5.1	6.2	6.7	7.8	6.0	10.1	6.0	8.1	6.6	1.8
Average	5.7	6.0	7.1	7.0	7.0	17.4	19.0	6.6	18.2	9.9	2.7
DO JG (50)	9.6	10.9	12.2	10.6	9.3	36.3	39.1	10.5	37.7	18.3	6.0
SC JG (50)	3.3	4.0	4.9	5.3	6.1	4.7	8.0	4.7	6.4	5.2	1.4
WC JG (50)	3.8	4.7	5.2	4.9	4.4	21.2	19.9	4.6	20.6	9.2	2.0
FF JG (50)	9.9	11.0	12.8	11.6	11.0	25.8	32.4	11.3	29.1	16.3	6.0
OT JG (50)	13.2	15.6	17.7	14.6	11.7	45.8	54.1	14.6	50.0	24.7	10.6
MT JG (50)	5.7	6.2	7.7	7.8	8.5	17.3	22.1	7.2	19.7	10.8	2.5
ET JG (50)	3.9	4.3	4.3	4.2	4.0	13.8	9.6	4.2	11.7	6.3	1.0

of $E_d(0^-, \lambda)$. This point is developed more completely in Sect. 1.5.4 when the $E_d(0^+, \lambda)$ intercomparisons are made.

1.5.3 K_L and K_d

Diffuse attenuation coefficients are calculated from the vertical profiles of the in-water light field. The $L_u(z, \lambda)$, $E_d(z, \lambda)$, and $E_u(z, \lambda)$ data are used to calculate $K_L(\lambda)$, $K_d(\lambda)$, and $K_u(\lambda)$, respectively, which are needed to calculate (by linear extrapolation of the log-transformed data)

the null depth values of the corresponding optical parameters. Of the three attenuation coefficients, only $K_d(\lambda)$ is intercompared for all three processors; $K_L(\lambda)$ is only intercompared for the JRC and GSFC processors, because $K_L(\lambda)$ is not normally reported by the Satlantic processor (although it is calculated and used).

Given the importance of the attenuation coefficients to the derivation of the primary optical variables, it is important they be estimated as accurately as possible. Summaries of the intercomparison of the $K_d(\lambda)$ and $K_L(\lambda)$

values are presented in Tables 6 and 7, respectively. The smallest differences are associated with the JRC and GSFC intercomparisons. For the JG comparisons, the winch and crane data (WP and SO) are the best, and the free-fall data the worst (the LN data are notably poor). For the JS and GS comparisons, there is a mixture of best results between SO and MN instrument types; the LN results are always the worst, and in some cases, significantly so. In all cases, the band-ratio results are better than the spectral averages, but they are not always better than some individual wavelengths.

One quality control parameter that can be applied to the $K_d(\lambda)$ estimates is to compare them to $K_w(\lambda)$ values for pure water, $K_w(\lambda)$, computed from the Pope and Fry (1997) absorption data and the Morel (1974) backscatter values for pure water.† The intercomparison is made by calculating the percentage of casts for each processor and the deployment methods (WC and FF) for which $K_d(\lambda) < K_w(\lambda)$ (in the original 40-cast data set), and the results are shown in Fig. 11 as a function of wavelength. Noting that one cast equates to 5% in each 20-cast category within the plot (FF or WC), the WC data satisfy the quality control test except for the Satlantic results beyond the blue part of the spectrum, for which an increasingly large number of casts do not. All of the processors have difficulty with the FF data, for which there is a general increase in failures from the blue to the red domain. Although not shown in the plot, the majority of the failures come from the LN data (as inferred in Table 6).

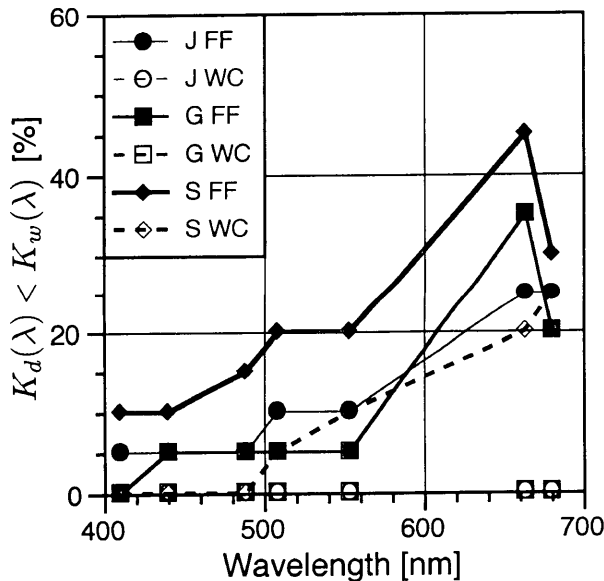


Fig. 11. The percentage of casts for which $K_d(\lambda) < K_w(\lambda)$ as a function of the data processors and deployment methods. The solid symbols and lines correspond to the FF category, and the open symbols and dashed lines correspond to the WC category.

† ProSoft posts warnings in the header records of the output file when $K_d < K_w$.

1.5.4 $E_d(0^+)$

Changing atmospheric conditions, particularly under cloud cover, leads directly to variability of the in-water light field which must be corrected to obtain accurate estimations of optical properties from irradiance or radiance profiles. First-order corrections for this variability can be made using above-water (on deck) measurements of solar irradiance, $E_d(0^+, \lambda)$. For the AMT and AAOT measurements, the emphasis is on collecting data only during clear-sky conditions, so the extra variance from atmospheric variability during optical profiling is minimized. Regardless of whether or not the in-water optical data are corrected for atmospheric variability on a point-by-point basis (Sect. 3.3.2.2), the $E_d(0^+, \lambda)$ data are needed to provide for the normalization of $L_W(\lambda)$ in the calculation of $R_{rs}(\lambda)$ and $[L_W(\lambda)]_N$.

Although not as notable as the results for $E_d(0^-, \lambda)$ (Sect. 1.5.2), the $E_d(0^+, \lambda)$ differences also partition into two groups, as shown in Table 8: a) those associated with a stable reference (WP, MN, and SC), and b) those associated with an unstabilized reference (SO, LN, and DO). Because all of the intercomparisons for the three processors are excellent—always to within 2.5%—it is easier to see this effect in the DO and SC intercomparisons for the JG extended data set. For these results, the unstabilized reference values are a factor of 5–6 larger with respect to the stabilized values (noting that this equates to a difference of approximately 1.0%); the band-ratio results are, however, to within 0.1% in either case. All of the OT data are from unstabilized references, so these results are the poorest, with some uncertainties approaching 2.5%.

As discussed earlier, a useful diagnostic as to the efficacy of the $E_d(0^-, \lambda)$ calculation is the ratio between the two with the latter adjusted for the effects of the air–sea interface: $E_d(0^-, \lambda) / [0.96 E_d(0^+, \lambda)]$. A comparison of the UPD values for this ratio is presented in Table 9. For all processors, the lowest differences occur for the stable references, WP and MN (SC), and the largest differences occur for the unstabilized references, SO and LN (DO), with the latter reaching very high differences for the JS and GS comparisons. The variance associated with choosing the top and bottom extrapolation intervals is included in these results, so the true effect of an unstabilized reference will not be known until the processing options are made more equal (Sects. 1.6.1 and 1.6.2).

1.5.5 R_{rs}

Derivations of $L_W(\lambda)$ from measurements of $L_u(z, \lambda)$ made in identical water conditions, but under different illumination conditions, will differ. This variability can be accounted for, in part, by adjusting $L_W(\lambda)$ using the $E_d(0^+, \lambda)$ measurement to derive the remote sensing reflectance, $R_{rs}(\lambda) = L_W(\lambda) / E_d(0^+, \lambda)$. This normalization of the illumination conditions makes $R_{rs}(\lambda)$ the primary

Table 8. A summary of the $\bar{\psi}$, Ψ , and Φ values for the computation of $E_d(0^+ \lambda)$.

Comparison	$\bar{\psi}(412)$	$\bar{\psi}(443)$	$\bar{\psi}(490)$	$\bar{\psi}(510)$	$\bar{\psi}(555)$	$\bar{\psi}(665)$	$\bar{\psi}(683)$	Ψ_{1-5}	Ψ_{6-7}	Ψ_{1-7}	$\Phi_{3/5}$
SO JG (40)	0.2	0.2	0.3	0.3	0.3	0.3	0.3	0.2	0.3	0.3	0.0
LN JG (40)	0.3	0.7	0.2	0.6	0.4	0.6	0.2	0.4	0.4	0.4	0.2
WP JG (40)	0.3	0.4	0.4	0.4	0.4	0.4	0.4	0.4	0.4	0.4	0.0
MN JG (40)	0.1	0.1	0.1	0.1	0.1	0.1	0.1	0.1	0.1	0.1	0.0
Average	0.2	0.3	0.2	0.3	0.3	0.3	0.2	0.3	0.3	0.3	0.1
SO JS (40)	1.0	1.0	1.0	0.9	1.0	0.9	0.9	1.0	0.9	1.0	0.1
LN JS (40)	0.5	0.9	1.3	1.4	1.9	1.3	1.2	1.2	1.2	1.2	0.6
WP JS (40)	0.7	0.8	0.7	0.7	0.7	0.7	0.7	0.7	0.7	0.7	0.0
MN JS (40)	0.2	0.2	0.2	0.2	0.2	0.2	0.2	0.2	0.2	0.2	0.0
Average	0.6	0.7	0.8	0.8	0.9	0.8	0.7	0.8	0.8	0.8	0.2
SO GS (40)	0.9	0.8	0.8	0.7	0.8	0.7	0.7	0.8	0.7	0.8	0.0
LN GS (40)	0.8	1.3	1.2	1.6	1.9	1.5	1.0	1.3	1.3	1.3	0.8
WP GS (40)	0.4	0.4	0.4	0.4	0.4	0.4	0.4	0.4	0.4	0.4	0.0
MN GS (40)	0.1	0.1	0.1	0.1	0.1	0.2	0.2	0.1	0.2	0.1	0.0
Average	0.5	0.7	0.6	0.7	0.8	0.7	0.6	0.7	0.6	0.7	0.2
DO JG (50)	1.0	1.2	1.1	1.2	1.2	1.3	1.2	1.1	1.2	1.2	0.1
SC JG (50)	0.2	0.2	0.2	0.2	0.2	0.2	0.2	0.2	0.2	0.2	0.0
WC JG (50)	1.2	1.3	1.4	1.4	1.5	1.5	1.5	1.3	1.5	1.4	0.1
FF JG (50)	0.2	0.4	0.2	0.3	0.3	0.3	0.2	0.3	0.3	0.3	0.1
OT JG (50)	1.8	2.0	2.2	2.2	2.3	2.4	2.4	2.1	2.4	2.2	0.1
MT JG (50)	0.2	0.4	0.2	0.4	0.3	0.3	0.2	0.3	0.3	0.3	0.1
ET JG (50)	0.3	0.3	0.3	0.3	0.4	0.4	0.4	0.3	0.4	0.3	0.0

Table 9. A summary of the $\bar{\psi}$, Ψ , and Φ values for the computation of $E_d(0^-, \lambda)/[0.96 E_d(0^+, \lambda)]$.

Comparison	$\bar{\psi}(412)$	$\bar{\psi}(443)$	$\bar{\psi}(490)$	$\bar{\psi}(510)$	$\bar{\psi}(555)$	$\bar{\psi}(665)$	$\bar{\psi}(683)$	Ψ_{1-5}	Ψ_{6-7}	Ψ_{1-7}	$\Phi_{3/5}$
SO JG (40)	4.4	4.8	4.9	5.1	5.6	8.7	18.2	5.0	13.4	7.4	1.7
LN JG (40)	6.5	8.5	5.8	6.2	8.3	20.5	24.2	7.1	22.3	11.4	4.5
WP JG (40)	1.3	1.1	1.1	1.3	1.2	1.7	1.8	1.2	1.8	1.4	0.7
MN JG (40)	1.7	1.5	2.2	2.3	1.8	2.8	1.9	1.9	2.3	2.0	1.1
Average	3.5	4.0	3.5	3.7	4.2	8.4	11.5	3.8	10.0	5.5	2.0
SO JS (40)	10.5	12.0	12.5	12.4	12.7	41.7	43.9	12.0	47.7	19.5	2.3
LN JS (40)	22.5	20.3	21.1	20.6	22.0	74.9	65.6	21.3	68.0	34.4	6.9
WP JS (40)	4.2	4.1	4.1	3.4	5.4	5.3	4.8	4.2	5.0	4.5	3.5
MN JS (40)	4.8	4.4	3.2	3.8	3.1	9.9	10.4	3.9	10.1	5.6	1.5
Average	10.5	10.2	10.2	10.0	10.8	32.9	31.2	10.3	32.7	16.0	3.6
SO GS (40)	7.6	8.9	9.7	9.6	9.9	35.5	34.5	9.1	40.0	15.6	1.9
LN GS (40)	26.9	25.3	23.5	22.9	28.6	81.5	77.5	25.5	78.2	40.3	10.6
WP GS (40)	3.8	4.3	4.1	3.4	5.6	5.6	5.7	4.3	5.6	4.6	3.2
MN GS (40)	5.4	5.1	4.2	4.4	4.7	11.2	11.0	4.7	11.1	6.6	2.3
Average	10.9	10.9	10.4	10.1	12.2	33.4	32.2	10.9	33.7	16.8	4.5
DO JG (50)	7.2	8.4	7.8	7.9	9.0	15.6	22.1	8.1	18.8	11.1	2.6
SC JG (50)	1.5	1.3	1.7	1.8	1.5	2.2	1.9	1.6	2.1	1.7	0.9
WC JG (50)	3.7	4.0	4.2	4.3	4.5	5.7	13.3	4.2	9.5	5.7	1.1
FF JG (50)	5.9	6.9	6.3	6.4	7.3	14.1	14.6	6.6	14.3	8.8	2.6
OT JG (50)	10.0	11.2	11.5	10.8	11.6	16.4	22.3	11.0	19.4	13.4	1.6
MT JG (50)	3.2	3.1	3.5	3.9	4.2	8.5	8.6	3.6	8.6	5.0	2.1
ET JG (50)	3.0	4.4	2.8	3.1	3.8	7.4	14.6	3.4	11.0	5.6	1.9

variable for estimating chlorophyll *a* concentration from *in situ* optical measurements. The OC2v2 algorithm, for example, uses $\log_{10} [R_{rs}(490)/R_{rs}(555)]$ as the input variable. In addition, the remote sensing reflectance is one of the primary variables relating the AOPs of seawater to the inherent optical properties (IOPs).

The excellent agreement between the processors in the calculation of $E_d(0^+, \lambda)$ (Sect. 1.5.4) suggests much of the variability in the derivation of $R_{rs}(\lambda)$ will be due to the differences in calculating $L_W(\lambda)$. Because the water-leaving radiance is computed as a simple constant times the upwelled radiance at null depth, $L_W(\lambda) = 0.54 L_u(0^-, \lambda)$, the differences in the $L_u(0^-, \lambda)$ comparisons will determine most of the $R_{rs}(\lambda)$ differences. The exceptions will be when the differences in $E_d(0^+, \lambda)$ were maximal, which will increase the differences above the levels found for $L_u(0^-, \lambda)$.

The uncertainties for the $R_{rs}(\lambda)$ intercomparisons are given in Table 10. As anticipated, the levels of agreement closely follow the values established for $L_u(0^-, \lambda)$ (Table 4):

1. The smallest differences are associated with the JG intercomparisons (the JS and GS intercomparisons are, on average, a little more than twice as large);
2. The maximum differences are in the red part of the spectrum (665 nm), with minimal differences in the blue-green (490–510 nm) which increase towards the blue (412–443 nm);
3. The band-ratio results are always the smallest differences (except for some of the Satlantic intercomparisons);
4. The shallow coastal data (particularly the WiSPER data) have smaller differences than the deep ocean data (most notably in the red wavelengths); and
5. The results as a function of increasing chlorophyll *a* concentration, are not as simply defined as before, because of the elevated differences in $E_d(0^+, \lambda)$ for the OT regime.

The 2.5% intercomparison objective is satisfied for numerous comparisons noted earlier. For comparisons with the Satlantic processor, only the blue-green WiSPER and some of the band-ratio uncertainties are below 2.5%—most of the results are, on average, significantly above the threshold. For the JG comparisons, all of the WiSPER, and some of the miniNESS differences, are below 2.5%, as are all of the band-ratio results. Many of the shallow coastal results satisfy the objective, but the winch and crane average results do not (except the band-ratio results), because of the elevated differences in the estimation of $E_d(0^+, \lambda)$. Aside from the band-ratio results, the only concentration regime with uncertainties below 2.5% is the mesotrophic regime (but only for the blue-green wavelengths).

1.5.6 $[L_W]_N$

The so-called normalized water-leaving radiance (Gordon and Clark 1981), $[L_W(\lambda)]_N$, is defined as the hypothetical water-leaving radiance that would be measured in

the absence of any atmospheric loss with a zenith sun at the mean Earth–sun distance. The latter is accomplished by adjusting $R_{rs}(\lambda)$ with the (time dependent) mean extraterrestrial solar irradiance, $F_0(\lambda, d)$, which is usually formulated to depend on the sequential day of the year (SDY), d .

The intercomparison of normalized water-leaving radiances for the different processors and data categories is presented in Table 11. Because $[L_W(\lambda)]_N$ is calculated directly from $R_{rs}(\lambda)$, the uncertainties for the former are expected to follow those of the latter (Table 10). Although there is general agreement in the patterns between the two, in terms of the spectral shapes and the relationships between the analysis categories (e.g., the concentration regimes), the magnitude of the uncertainties differ significantly, with the exception of the JG band-ratio results.

The most likely explanation for the increase in uncertainties is in the chosen values for the $F_0(\lambda)$ correction term: the JRC processor uses the Neckel and Labs (1984) values interpolated to specific center wavelengths (Sect. 3.3.2.8), while the GSFC processor uses the Neckel and Labs (1984) values weighted by the spectral response of the SeaWiFS bands (Sect. 2.4.4). Figure 12 shows the relationship between the GSFC and JRC $F_0(\lambda)$ values (the GSFC processor does not include a value for 683 nm, because this is not a SeaWiFS wavelength). There is a strong bias between the two processors with maximum differences in the blue (6.5% at 412 nm), intermediate differences in the green (3.2% at 510 nm), and minimum differences in the red (1.9% at 665 nm). The band-ratio results for the JRC and GSFC intercomparison of $F_0(\lambda)$ are very good—the maximum percent difference is 0.4%. The JG $R_{rs}(\lambda)$ band ratios are all less than 2.5%, so the excellent $F_0(\lambda)$ band ratios ensure very good $[L_W(\lambda)]_N$ band ratios.

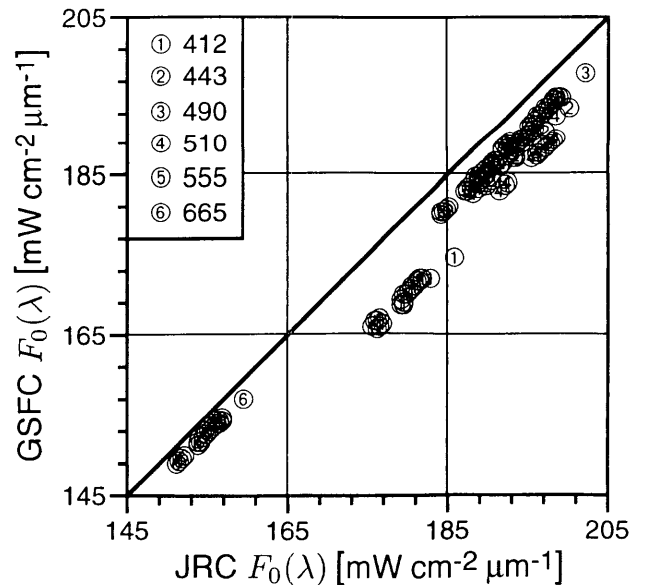


Fig. 12. A comparison of the JRC and GSFC determinations of $F_0(\lambda)$ (for the 50-cast data set).

Table 10. A summary of the $\bar{\psi}$, Ψ , and Φ values for the computation of $R_{rs}(\lambda)$.

Comparison	$\bar{\psi}(412)$	$\bar{\psi}(443)$	$\bar{\psi}(490)$	$\bar{\psi}(510)$	$\bar{\psi}(555)$	$\bar{\psi}(665)$	$\bar{\psi}(683)$	Ψ_{1-5}	Ψ_{6-7}	Ψ_{1-7}	$\Phi_{3/5}$
SO JG (40)	3.8	4.1	3.4	3.2	2.8	26.8	12.4	3.5	19.6	8.1	1.0
LN JG (40)	3.7	3.6	2.6	2.5	4.0	25.1	23.8	3.2	24.8	9.1	2.1
WP JG (40)	1.7	1.7	1.5	1.5	1.5	2.3	3.5	1.6	2.9	1.9	0.2
MN JG (40)	3.0	2.8	2.3	2.3	2.4	6.0	8.1	2.6	7.0	3.8	0.4
Average	3.0	3.0	2.5	2.4	2.7	15.0	11.9	2.7	13.6	5.7	0.9
SO JS (40)	13.4	13.2	10.0	9.6	8.6	46.3	32.8	10.9	40.9	18.0	2.0
LN JS (40)	7.0	7.0	6.5	6.7	8.4	44.7	43.5	7.1	42.5	17.1	7.2
WP JS (40)	2.0	1.8	1.6	1.6	1.7	3.3	4.5	1.8	3.9	2.4	0.2
MN JS (40)	7.5	6.2	4.6	4.5	4.3	11.3	10.7	5.4	11.0	7.0	0.3
Average	7.5	7.1	5.7	5.6	5.8	26.4	22.9	6.3	24.6	11.1	2.4
SO GS (40)	9.9	10.4	8.0	7.4	7.2	28.8	25.8	8.6	27.1	13.0	1.6
LN GS (40)	7.8	8.3	7.3	7.3	10.5	47.3	48.3	8.2	46.4	19.0	8.2
WP GS (40)	2.3	2.1	1.8	1.8	1.8	4.2	4.7	2.0	4.4	2.7	0.3
MN GS (40)	7.4	5.8	3.9	3.7	3.5	10.9	10.2	4.9	10.6	6.5	0.6
Average	6.9	6.7	5.2	5.1	5.7	22.8	22.2	5.9	22.1	10.3	2.7
DO JG (50)	3.5	3.6	3.1	3.2	3.9	25.8	21.6	3.5	23.8	9.2	1.7
SC JG (50)	2.3	2.2	1.9	1.9	2.0	4.1	5.8	2.1	4.9	2.9	0.3
WC JG (50)	3.3	3.5	3.1	3.1	3.0	17.2	12.1	3.2	14.6	6.5	0.7
FF JG (50)	2.9	2.7	2.2	2.4	3.3	16.7	18.0	2.7	17.7	6.9	1.5
OT JG (50)	2.9	2.9	3.1	3.7	4.6	24.0	26.8	3.4	25.4	9.7	1.8
MT JG (50)	2.4	2.5	2.1	2.0	2.7	13.3	13.8	2.3	13.9	5.5	0.9
ET JG (50)	4.1	4.1	3.1	3.0	2.6	15.9	7.6	3.4	11.8	5.8	0.7

Table 11. A summary of the $\bar{\psi}$, Ψ , and Φ values for the computation of $[L_W(\lambda)]_N$.

Comparison	$\bar{\psi}(412)$	$\bar{\psi}(443)$	$\bar{\psi}(490)$	$\bar{\psi}(510)$	$\bar{\psi}(555)$	$\bar{\psi}(665)$	$\bar{\psi}(683)$	Ψ_{1-5}	Ψ_{6-7}	Ψ_{1-7}	$\Phi_{3/5}$
SO JG (40)	8.0	5.2	3.9	5.6	3.2	29.0		5.2	29.0	9.1	0.9
LN JG (40)	6.1	4.8	3.5	4.9	4.3	27.1		4.7	27.1	8.1	2.2
WP JG (40)	7.2	4.5	3.5	4.0	3.6	2.9		4.6	2.9	4.3	0.3
MN JG (40)	8.2	5.6	4.8	4.5	4.8	8.1		5.6	8.1	6.0	0.4
Average	7.4	5.0	3.9	4.7	4.0	16.8		5.0	16.8	6.9	1.0
SO JS (40)	15.0	13.8	10.8	9.6	8.5	45.4	32.5	11.5	40.2	18.3	3.4
LN JS (40)	10.8	8.8	8.4	7.3	9.4	44.9	43.2	9.0	42.4	18.4	7.4
WP JS (40)	4.7	4.0	4.0	2.1	2.6	4.2	5.5	3.5	4.9	3.9	2.4
MN JS (40)	10.9	10.3	8.3	3.6	5.3	9.8	8.9	7.7	9.4	8.2	3.0
Average	10.3	9.2	7.9	5.7	6.5	26.1	22.6	7.9	24.2	12.2	4.1
SO GS (40)	8.6	9.6	7.7	6.4	6.3	27.8		7.7	27.8	10.7	3.2
LN GS (40)	7.6	8.3	7.5	6.7	10.2	47.9		8.0	47.9	14.1	8.5
WP GS (40)	3.6	2.7	2.3	4.1	2.9	5.9		3.1	5.9	3.6	2.6
MN GS (40)	6.3	6.4	4.7	3.8	3.7	10.2		5.0	10.2	5.8	3.0
Average	6.5	6.7	5.6	5.3	5.8	23.0		6.0	23.0	8.6	4.3
DO JG (50)	7.0	4.9	3.9	5.7	4.5	27.9		5.2	27.9	8.8	1.7
SC JG (50)	7.7	5.0	4.2	4.2	4.2	5.5		5.1	5.5	5.1	0.4
WC JG (50)	7.6	5.1	4.1	5.2	4.0	19.1		5.2	19.1	7.5	0.7
FF JG (50)	7.0	4.8	3.9	5.0	4.7	18.5		5.1	18.5	7.2	1.6
OT JG (50)	6.3	4.2	3.9	6.0	5.1	26.2		5.1	26.2	8.6	1.9
MT JG (50)	7.0	4.9	3.9	4.5	4.3	15.3		4.9	15.3	6.6	1.0
ET JG (50)	8.5	5.7	4.2	5.2	3.8	17.3		5.5	17.3	7.4	0.8

All of the individual spectral differences in Fig. 12 lie on straight lines, which suggests there is a deterministic, significant, difference in how the $F_0(\lambda)$ terms are chosen (this is also inferred by the band-ratio results). A comparison between the Satlantic and JRC processor is, however, somewhat different. The band-ratio results are all elevated, the overall average is 2.2%, and the maximum individual wavelength differences range from 7.7% at 412 nm, 3.2% at 510 nm, and 2.8% at 665 nm. When these are combined with the $R_{rs}(\lambda)$ differences, the $[L_W(\lambda)]_N$ uncertainties are all larger. Very similar results are seen for the Satlantic and GSFC comparisons.

Very few of the $[L_W(\lambda)]_N$ uncertainties are less than 2.5%. The only notable exceptions are the JG band-ratio results, and a few of the WP results. The range of differences is frequently small for the JG results, e.g., the DO, SC, WC, and FF results at 412 nm range from 7.0–7.7%, so if the $F_0(\lambda)$ calculations can be reconciled, there is every reason to believe these uncertainties can be significantly reduced. The latter is only partly true for the Satlantic comparisons, because the $R_{rs}(\lambda)$ uncertainties were frequently large, but there is certainly a chance to improve the WP intercomparisons.

1.5.7 $E_u(0^-)$ and $Q_n(0^-)$

$L_u(0^-, \lambda)$ and $E_u(0^-, \lambda)$ are related by the Q -factor. This permits an alternative approach for the calculation of $L_W(\lambda)$, based on applying the Q -factor to measurements of the irradiance reflectance, denoted $R(z, \lambda)$ and defined as $E_u(z, \lambda)/E_d(z, \lambda)$. The uncertainties associated with this approach are only explored to the extent that intercomparisons of $E_u(0^-, \lambda)$, $R(0^-, \lambda)$, and $Q_n(0^-, \lambda)$ are made for the JRC and GSFC processors (the Satlantic processor does not compute the Q -factor).

The $E_u(0^-, \lambda)$ uncertainties are presented in Table 12. The best agreement occurs for the shallow coastal data (WP and MN), which have overall uncertainties below 2.5% in the blue-green part of the spectrum, slightly above 2.5% in the red domain, and band ratios well below 2.5%. The deep ocean data are a mixture of low (LN) and high (SO) uncertainties, with universally high values in the red wavelengths. The poorer results for SO data are hard to explain, because this instrument produces more data per unit depth interval than LN. It is interesting to note a similar result for the $L_u(0^-, \lambda)$ results (Table 4), although it is not as significant. In comparison, the JG results for $E_d(0^-, \lambda)$, show the SO uncertainties are substantially lower than the LN uncertainties (Table 5).

The (unexpectedly) larger uncertainty with the SO data is the reason the FF category has a smaller average uncertainty than the WC category, and it produces a clear trend of increasing uncertainty with increasing chlorophyll *a* concentration (the SO data represent a significant portion of the ET data, 60% of all casts, as shown in Table 3). This is a clear example of how biases in sampling (and then

processing results) can influence the relationships between the different analysis categories.

The intercomparison results for determining $R(\lambda)$ are presented in Table 13. These are necessarily a combination of the $E_u(0^-, \lambda)$ and $E_d(0^-, \lambda)$ results, and there is a general elevation in uncertainties, even in the band-ratio results. Although the increase in uncertainties is sometimes small, there are some notable changes in the relationships among the categories: a) the SO results are now lower than the LN results, so the WC uncertainties are less than the FF uncertainties; and b) the uncertainties as a function of concentration regime are more uniform.

The Q -factor is the ratio between the upwelled irradiance and radiance, so intercomparisons of $Q_n(0^-, \lambda)$, which are presented in Table 14, will be a combination of Tables 12 and 4, respectively. The patterns of agreement for $Q_n(0^-, \lambda)$ closely follow the patterns established for $E_u(0^-, \lambda)$ except there is greater uniformity between the instrument types (the WC and FF results are very similar), there are much lower uncertainties in the red part of the spectrum, and there is less distinction as a function of concentration regime (the still anomalously high SO uncertainties elevate the ET results).

Out of all the in-water variables, the overall uncertainties for $Q_n(0^-, \lambda)$ are the lowest, and many of the various categories of uncertainty are to within 2.5%. This is a direct consequence of the two input variables, $L_u(0^-, \lambda)$ and $E_u(0^-, \lambda)$, being upwelled measurements, so they are largely free of any surface effects (which raise the uncertainties in the measurements).

1.5.8 Ancillary Variables

Variables not immediately associated with the optical fields, but important to the derivation of optical parameters, plus those variables by which optical parameters are evaluated are important to the understanding of a total uncertainty budget. Examples of such variables are the solar zenith angle, θ , and the total chlorophyll *a* concentration derived from the OC2v2 algorithm.

The Satlantic data submission did not include the solar zenith angle, so only JRC and GSFC θ values were intercompared. For all of the standard (40-cast) data, the uncertainty in θ had an overall average value of 0.7%; the minimum-to-maximum differences for these data were 0.0–2.3%. For the 10 casts used to extend the standard data set, all of which were deep casts in oligotrophic conditions, the average uncertainty in θ was 1.1%, and the minimum-to-maximum differences were 0.3–5.0% (most of the variance was attributed to slightly different reference times used in the computations).

The intercomparison of the OC2v2 determination of total chlorophyll *a* concentration between the three data processors and with the high performance liquid chromatography (HPLC) determination of total chlorophyll *a* is presented in Table 15. The most obvious result is that the

Table 12. A summary of the $\bar{\psi}$, Ψ , and Φ values for the computation of $E_u(0^-, \lambda)$.

Comparison	$\bar{\psi}(412)$	$\bar{\psi}(443)$	$\bar{\psi}(490)$	$\bar{\psi}(510)$	$\bar{\psi}(555)$	$\bar{\psi}(665)$	$\bar{\psi}(683)$	Ψ_{1-5}	Ψ_{6-7}	Ψ_{1-7}	$\Phi_{3/5}$
SO JG (40)	4.4	4.7	3.9	4.2	4.6	30.2	12.3	4.4	21.3	9.2	1.4
LN JG (40)	1.7	1.8	1.9	1.9	2.0	29.0	27.0	1.8	28.0	9.3	0.8
WP JG (40)	1.1	1.1	0.9	0.9	1.0	2.1	3.1	1.0	2.6	1.5	0.2
MN JG (40)	2.5	2.6	2.0	2.1	2.2	3.8	3.6	2.3	3.7	2.7	0.3
Average	2.4	2.5	2.2	2.3	2.4	16.3	11.5	2.4	13.9	5.7	0.7
DO JG (50)	2.3	2.3	2.1	2.4	2.9	32.0	25.6	2.4	28.8	9.9	1.4
SC JG (50)	1.8	1.8	1.5	1.5	1.6	2.9	3.4	1.6	3.2	2.1	0.2
WC JG (50)	2.5	2.6	2.2	2.3	2.8	22.4	15.4	2.5	18.9	7.2	1.1
FF JG (50)	1.7	1.7	1.6	1.7	2.0	18.6	17.8	1.8	18.2	6.5	0.8
OT JG (50)	0.6	0.5	0.6	0.9	1.9	34.0	34.8	0.9	34.4	10.5	1.7
MT JG (50)	2.1	2.1	1.8	1.9	2.1	14.7	13.0	2.0	13.8	5.4	0.4
ET JG (50)	3.3	3.7	3.0	3.1	3.3	16.8	6.4	3.3	11.6	5.7	1.0

Table 13. A summary of the $\bar{\psi}$, Ψ , and Φ values for the computation of $R(0^-, \lambda)$.

Comparison	$\bar{\psi}(412)$	$\bar{\psi}(443)$	$\bar{\psi}(490)$	$\bar{\psi}(510)$	$\bar{\psi}(555)$	$\bar{\psi}(665)$	$\bar{\psi}(683)$	Ψ_{1-5}	Ψ_{6-7}	Ψ_{1-7}	$\Phi_{3/5}$
SO JG (40)	3.2	3.4	3.3	4.1	4.6	21.8	21.4	3.7	21.6	8.8	2.1
LN JG (40)	7.6	9.1	7.0	7.6	9.0	15.2	26.1	8.0	20.7	11.6	3.7
WP JG (40)	1.3	1.3	1.1	1.4	1.1	2.4	3.3	1.2	2.8	1.7	0.6
MN JG (40)	2.0	2.3	3.2	3.4	3.0	5.0	3.9	2.8	4.4	3.2	1.2
Average	3.5	4.0	3.7	4.1	4.4	11.1	13.7	3.9	12.4	6.4	1.9
DO JG (50)	3.8	4.3	3.6	4.2	5.2	24.5	28.3	4.2	26.4	10.6	2.6
SC JG (50)	1.7	1.8	2.2	2.4	2.0	3.7	3.6	2.0	3.6	2.5	0.9
WC JG (50)	2.1	2.1	2.0	2.5	2.8	18.8	19.4	2.3	19.1	7.1	1.6
FF JG (50)	3.7	4.4	3.9	4.3	4.9	14.0	17.5	4.2	15.8	7.5	2.2
OT JG (50)	2.3	2.5	2.2	2.2	3.2	32.4	36.1	2.5	34.2	11.6	1.9
MT JG (50)	3.9	3.6	4.1	4.7	4.6	10.5	11.3	4.2	10.9	6.1	1.9
ET JG (50)	2.1	3.6	2.2	2.8	3.6	10.5	13.6	2.9	12.0	5.5	2.1

Table 14. A summary of the $\bar{\psi}$, Ψ , and Φ values for the computation of $Q_n(0^-, \lambda)$.

Comparison	$\bar{\psi}(412)$	$\bar{\psi}(443)$	$\bar{\psi}(490)$	$\bar{\psi}(510)$	$\bar{\psi}(555)$	$\bar{\psi}(665)$	$\bar{\psi}(683)$	Ψ_{1-5}	Ψ_{6-7}	Ψ_{1-7}	$\Phi_{3/5}$
SO JG (40)	3.6	3.6	3.5	4.1	4.1	6.2	9.1	3.8	7.6	4.9	0.7
LN JG (40)	2.6	2.2	2.0	2.4	2.9	6.2	6.4	2.4	6.3	3.5	1.4
WP JG (40)	1.0	0.9	0.7	0.7	0.7	1.2	1.3	0.8	1.2	0.9	0.1
MN JG (40)	1.6	1.2	1.2	1.4	1.6	3.7	4.8	1.4	4.3	2.2	0.4
Average	2.2	2.0	1.9	2.1	2.3	4.3	5.4	2.1	4.9	2.9	0.7
DO JG (50)	2.5	2.5	2.5	2.9	3.3	7.5	9.5	2.7	8.5	4.4	1.1
SC JG (50)	1.3	1.1	1.0	1.1	1.2	2.5	3.0	1.1	2.7	1.6	0.3
WC JG (50)	2.1	2.1	2.0	2.3	2.4	5.7	7.3	2.2	6.5	3.4	0.6
FF JG (50)	2.0	1.8	1.8	2.0	2.5	5.3	6.6	2.0	6.0	3.1	0.9
OT JG (50)	1.6	1.5	1.7	2.0	2.7	9.3	11.5	1.9	10.4	4.3	1.3
MT JG (50)	1.6	1.6	1.6	1.8	2.1	4.6	5.2	1.7	4.9	2.6	0.7
ET JG (50)	3.0	2.7	2.5	2.8	2.7	3.5	5.6	2.7	4.6	3.3	0.5

OC2v2 algorithm does a poor job and this is irrespective of the data processor being considered. Nonetheless, there are substantial differences between the data types, with the winch and crane results proving superior to the corresponding free-fall results, i.e., the SO results are better than the LN results, and the WP results are superior to the MN results.

Table 15. The intercomparison of the OC2v2 algorithm results between processors and with respect to the HPLC determination of C_{Ta} for the standard (40-cast) data set.

Data Type	OC2v2			HPLC		
	JG	JS	GS	J	G	S
SO	4.3	4.3	5.7	68.2	68.3	67.8
LN	6.9	26.4	29.2	86.1	80.4	95.2
WP	5.0	9.2	12.0	95.7	97.1	106.3
MN	6.9	2.6	9.2	110.3	109.7	110.3
Average	5.8	10.5	14.1	90.1	88.9	94.9

It is also clear that the deep ocean results (SO and LN) are better than the shallow coastal results (WP and MN). This is expected, because the OC2v2 algorithm was formulated from Case-1 (deep ocean) data (O'Reilly et al. 1998), and, in general, is not suitable for coastal waters. The uncertainty in the OC2v2 algorithm, based on the original data set used to create it, is approximately 30.8%. If the AMT data set is used as a separate control to evaluate this uncertainty, the uncertainty in the OC2v2 algorithm based on the full AMT matrix (not just the data subset used for DARR-00) is approximately 34.4% when no filtering for possibly spurious observations is applied to the data; if 24 stations, which appear as outliers are removed from the analysis (these usually correspond to unusual phytoplankton assemblages, highly heterogeneous water masses, etc.), the uncertainty is about 30.2%.

The good agreement between the original uncertainty estimated of the OC2v2 algorithm and that achieved with the AMT data matrix suggests the large uncertainties seen with the SO and LN data in Table 15 are anomalously high and a consequence of dealing with a small subsample from a much larger database.

1.5.9 V1 Summary

The standard results are hereafter referred to as the V1 results, and processing options not in keeping with the V1 options are referred to as *nonstandard*. A summary of the V1 processing uncertainties is presented in Table 16. The results are organized according to the primary variables and the three concentration regimes. The latter are included to investigate whether or not there is any dependence with respect to chlorophyll *a* concentration as a function of the processing options and, of course, the individual variables. It is important to remember the results for the concentration regimes are derived from the extended

(50-cast) data set and only involve the JRC and GSFC processors, whereas the individual parameter results are from the standard (40-cast) data set and all available processor combinations (the data sets involved are noted in the table alongside the two-letter processor codes). The principal V1 results are as follows (Tables 4–14 and 16):

1. The smallest uncertainties are associated with the JG intercomparisons (which, on average, are significantly less than the JS or GS results).
2. Many of the intercomparisons have maximum uncertainties in the red part of the spectrum (665 nm), with minimal uncertainties in the blue-green wavelengths (490–510 nm) which increase towards the blue domain (412–443 nm).
3. The band-ratio uncertainties are almost always the smallest, and are frequently less than 2.5%.
4. Most of the uncertainties exceed the 2.5% intercomparison objective, but the JG uncertainties for $L_u(0^-)$, $E_d(0^+)$, R_{rs} , $E_u(0^-)$, and $Q_n(0^-)$ are less than or close to 2.5% for many of the blue-green wavelengths.
5. The shallow coastal data (in particular the WiSPER data) have smaller uncertainties than the deep ocean data (most notably for the red wavelengths).
6. The winch and crane data (especially the WiSPER data) have smaller uncertainties than the free-fall data (most notably in the red part of the spectrum).
7. The uncertainties in the diffuse attenuation coefficients, K_L and K_d , exceed the uncertainties in the corresponding extrapolated (null depth) radiometric measurements, $L_u(0^-)$ and $E_d(0^-)$, respectively.
8. As a function of increasing chlorophyll *a* concentration (OT to MT to ET), there is a general increase in uncertainties in the blue-green part of the spectrum, but a decrease in the red wavelengths, and a decrease in the band-ratio uncertainties (note the very large uncertainties for the K_d OT results).

In addition to following the evolution in the aforementioned principal results, the subsequent analyses are concerned with the following objectives (documented below in Sects. 1.6.1–1.6.4):

- a) Determine if results converge (i.e., the uncertainties approach zero) as the JRC and GSFC processing options are made more similar;
- b) Quantify the level of uncertainty associated with the processing options; and
- c) Establish which of the final uncertainties for the data products are within the 1.0% or 2.5% objectives set at the beginning of the DARR-00 activity.

As an easily referenced indicator of the convergence process, the final row in Table 16 gives the averages of all the

Table 16. A summary of the $\bar{\psi}$, Ψ , and Φ values for the computation of the V1 primary variables.

Comparison		$\bar{\psi}(412)$	$\bar{\psi}(443)$	$\bar{\psi}(490)$	$\bar{\psi}(510)$	$\bar{\psi}(555)$	$\bar{\psi}(665)$	$\bar{\psi}(683)$	Ψ_{1-5}	Ψ_{6-7}	Ψ_{1-7}	$\Phi_{3/5}$
$L_u(0^-)$	JG (40)	2.7	2.6	2.1	2.2	2.4	14.6	11.3	2.4	12.9	5.4	0.9
	JS (40)	7.1	9.3	5.1	5.0	5.1	26.6	22.1	6.3	24.3	11.3	2.3
	GS (40)	6.9	9.2	5.0	4.9	5.3	23.1	21.7	6.3	22.0	10.7	2.5
OT	JG (50)	1.6	1.5	1.6	1.8	2.7	25.5	28.7	1.8	27.1	9.1	1.8
MT	JG (50)	2.1	2.0	1.8	1.9	2.4	13.4	12.7	2.0	13.0	5.2	0.8
ET	JG (50)	3.7	3.7	2.7	2.6	2.2	15.5	7.4	3.0	11.4	5.4	0.7
K_L	JG (40)	5.7	6.0	7.1	7.0	7.0	17.4	19.0	6.6	18.2	9.9	2.7
OT	JG (50)	13.2	15.6	17.7	14.6	11.7	45.8	54.1	14.6	50.0	24.7	10.6
MT	JG (50)	5.7	6.2	7.7	7.8	8.5	17.3	22.1	7.2	19.7	10.8	2.5
ET	JG (50)	3.9	4.3	4.3	4.2	4.0	13.8	9.6	4.2	11.7	6.3	1.0
$E_d(0^-)$	JG (40)	3.4	3.8	3.4	3.7	4.1	8.3	11.5	3.7	9.9	5.4	1.9
	JS (40)	10.3	10.2	10.1	10.1	10.9	32.8	31.0	10.3	32.5	15.9	3.7
	GS (40)	10.8	10.9	10.5	10.4	12.3	33.3	32.0	11.0	33.5	16.8	4.4
OT	JG (50)	8.5	9.6	9.7	9.0	9.7	16.5	24.2	9.3	20.4	12.5	1.5
MT	JG (50)	3.2	2.8	3.4	3.9	4.1	8.5	8.7	3.5	8.6	4.9	2.0
ET	JG (50)	2.8	4.2	2.5	2.9	3.5	7.1	14.4	3.2	10.8	5.4	1.9
K_d	JG (40)	9.4	11.2	12.5	11.4	12.3	4.3	5.3	13.5	4.8	9.8	7.7
	JS (40)	17.4	19.4	27.1	28.1	21.1	14.8	11.2	23.5	13.6	20.5	15.2
	GS (40)	19.8	20.0	25.8	28.1	23.1	14.3	12.0	24.3	13.9	21.4	17.1
OT	JG (50)	56.9	67.4	64.6	39.3	24.3	8.2	10.9	50.5	9.6	38.8	44.6
MT	JG (50)	7.1	6.5	11.6	12.9	16.2	4.6	4.2	15.3	4.4	10.1	4.8
ET	JG (50)	2.5	5.3	4.5	6.1	5.6	3.9	6.5	4.8	5.2	4.9	4.7
$E_d(0^+)$	JG (40)	0.2	0.3	0.2	0.3	0.3	0.3	0.2	0.3	0.3	0.3	0.1
	JS (40)	0.6	0.7	0.8	0.8	0.9	0.8	0.7	0.8	0.8	0.8	0.2
	GS (40)	0.5	0.7	0.6	0.7	0.8	0.7	0.6	0.7	0.6	0.7	0.2
OT	JG (50)	1.8	2.0	2.2	2.2	2.3	2.4	2.4	2.1	2.4	2.2	0.1
MT	JG (50)	0.2	0.4	0.2	0.4	0.3	0.3	0.2	0.3	0.3	0.3	0.1
ET	JG (50)	0.3	0.3	0.3	0.3	0.4	0.4	0.4	0.3	0.4	0.3	0.0
R_{rs}	JG (40)	3.0	3.0	2.5	2.4	2.7	15.0	11.9	2.7	13.6	5.7	0.9
	JS (40)	7.5	7.1	5.7	5.6	5.8	26.4	22.9	6.3	24.6	11.1	2.4
	GS (40)	6.9	6.7	5.2	5.1	5.7	22.8	22.2	5.9	22.1	10.3	2.7
OT	JG (50)	2.9	2.9	3.1	3.7	4.6	24.0	26.8	3.4	25.4	9.7	1.8
MT	JG (50)	2.4	2.5	2.1	2.0	2.7	13.3	13.8	2.3	13.9	5.5	0.9
ET	JG (50)	4.1	4.1	3.1	3.0	2.6	15.9	7.6	3.4	11.8	5.8	0.7
$[L_w]_N$	JG (40)	7.4	5.0	3.9	4.7	4.0	16.8		5.0	16.8	6.9	1.0
	JS (40)	10.3	9.2	7.9	5.7	6.5	26.1	22.6	7.9	24.2	12.2	4.1
	GS (40)	6.5	6.7	5.6	5.3	5.8	23.0		6.0	23.0	8.6	4.3
OT	JG (50)	6.3	4.2	3.9	6.0	5.1	26.2		5.1	26.2	8.6	1.9
MT	JG (50)	7.0	4.9	3.9	4.5	4.3	15.3		4.9	15.3	6.6	1.0
ET	JG (50)	8.5	5.7	4.2	5.2	3.8	17.3		5.5	17.3	7.4	0.8
$E_u(0^-)$	JG (40)	2.4	2.5	2.2	2.3	2.4	16.3	11.5	2.4	13.9	5.7	0.7
	OT	JG (50)	0.6	0.5	0.6	0.9	1.9	34.0	0.9	34.4	10.5	1.7
	MT	JG (50)	2.1	2.1	1.8	1.9	2.1	14.7	2.0	13.8	5.4	0.4
ET	JG (50)	3.3	3.7	3.0	3.1	3.3	16.8	6.4	3.3	11.6	5.7	1.0
$Q_n(0^-)$	JG (40)	2.2	2.0	1.9	2.1	2.3	4.3	5.4	2.1	4.9	2.9	0.7
	OT	JG (50)	1.6	1.5	1.7	2.0	2.7	9.3	1.9	10.4	4.3	1.3
	MT	JG (50)	1.6	1.6	1.6	1.8	2.1	4.6	1.7	4.9	2.6	0.7
ET	JG (50)	3.0	2.7	2.5	2.8	2.7	3.5	5.6	2.7	4.6	3.3	0.5
All	JG (40)	4.1	4.1	4.0	4.0	4.2	10.8	9.5	4.3	10.6	5.8	1.8

Table 17. The GSFC and JRC processing options as a function of the processing version number. The selection of the extrapolation intervals is indicated with a one-letter code: G for GSFC and J for JRC, i.e., a G indicates the processing interval was set by the configuration for the GSFC data processor, and a J means it was set by the configuration for the JRC processor.

Ver- sion No.	Extrapolation Intervals								Tilt		$E_d(0^+)$		Outlier		Fitting	
	GSFC				JRC				Filtering		Normalized		Filtering		Function	
	SO	LN	WP	MN	SO	LN	WP	MN	GSFC	JRC	GSFC	JRC	GSFC	JRC	GSFC	JRC
1	G	G	G	G	J	J	J	J	No	Yes	No	Yes	No	Yes	Linear	Linear
2	G	G	J	J	G	G	J	J	No	Yes	No	Yes	No	Yes	Linear	Linear
3	G	G	J	J	G	G	J	J	Yes	Yes	No	No	No	Yes	Linear	Linear
4	G	G	J	J	G	G	J	J	Yes	Yes	No	No	Yes†	Yes	Robust	Linear
5	G	G	J	J	G	G	J	J	No	Yes	No	No	No	No	Linear	Linear

† Partial outlier rejection from the robust fitting function which reduces the weight of data points with a large standard deviation.

primary variables presented for the standard JG comparisons, i.e., only the 40-cast data set is used. The convergence in the extended (50-cast) data set is discerned from the concentration regime results.

1.6 RESULTS–NONSTANDARD

Nonstandard options to the JRC and GSFC processors were executed to investigate differences in the V1 inter-comparison by processing profile data with nonstandard options. The results from the subsequent changes to the standard processing options are identified as follows:

V2 For the JRC processor, the only change with respect to the standard processing options was to use the extrapolation intervals for the SeaOPS and LoCNESS data as defined by the GSFC processing. Similarly, for the GSFC processor, the only change was to use the extrapolation intervals for the WiSPER and miniNESS data as defined by the JRC processing. No changes were made to the Satlantic processing configuration.

V3 In addition to the V2 changes, no $E_d(0^+)$ normalization was used with the JRC processor (the JRC processor still filtered the data for outliers and the GSFC processor did not), and the GSFC processor used a 5° tilt filter (as did the JRC processor). No changes were made to the Satlantic processing configuration.

The JRC and GSFC processors were very similar for the V3 configurations—the only difference between the two was the JRC processor used outlier filtering and the GSFC processor did not (which potentially affects a small amount of data in each cast). These options were then used as a baseline to explore two different aspects of the processing:

V4 In addition to the V3 changes, the GSFC processor was changed to use a robust linear fit, which weights the data in the extrapolation interval to minimize the significance of data points with higher variance.

No changes were made to the Satlantic processing configuration.

V5 In addition to the V3 changes, the GSFC processor did not use a tilt filter, and the JRC processor did not filter the data for outliers. No changes were made to the Satlantic processing configuration.

A summary of the options used with the GSFC and JRC processors for each processing version is given in Table 17.

1.6.1 V2 Summary

The only change made for the V2 processing was to use the same extrapolation intervals for the JRC and GSFC processors. A summary of the effects of this change is shown in Table 18. In comparison to the V1 results (Table 16), there are substantial improvements in most of the JG variables. No changes were made to the Satlantic processor, and the JS and GS uncertainties are largely unchanged. The most significant aspects of the improvements are the uncertainties are lower at all wavelengths and they are spectrally flatter. Given the largest uncertainties for the V1 results are in the red domain, the largest improvements with the V2 processing are in the red domain.

Because the JG values for the V2 results are spectrally more uniform, Ψ_{1-5} , Ψ_{6-7} , and $\Phi_{3/5}$ are appropriate variables for summarizing the improvements derived from identical extrapolation intervals (the \downarrow symbol represents a reduction in uncertainty with respect to the V1 values):

$$L_u(0^-) \quad \Psi_{1-5} = 0.5(\downarrow 1.9)\%, \quad \Psi_{6-7} = 1.7(\downarrow 11.2)\%, \quad \text{and} \\ \Phi_{3/5} = 0.1(\downarrow 0.8)\%;$$

$$K_L \quad \Psi_{1-5} = 0.8(\downarrow 5.8)\%, \quad \Psi_{6-7} = 2.0(\downarrow 16.2)\%, \quad \text{and} \\ \Phi_{3/5} = 0.4(\downarrow 2.3)\%;$$

$$E_d(0^-) \quad \Psi_{1-5} = 1.2(\downarrow 2.5)\%, \quad \Psi_{6-7} = 2.5(\downarrow 7.4)\%, \quad \text{and} \\ \Phi_{3/5} = 0.3(\downarrow 1.6)\%;$$

$$K_d \quad \Psi_{1-5} = 3.2(\downarrow 10.3)\%, \quad \Psi_{6-7} = 0.8(\downarrow 4.0)\%, \quad \text{and} \\ \Phi_{3/5} = 1.6(\downarrow 6.1)\%;$$

$$E_d(0^+) \quad \Psi_{1-5} = 0.3(\downarrow 0.0)\%, \quad \Psi_{6-7} = 0.3(\downarrow 0.0)\%, \quad \text{and} \\ \Phi_{3/5} = 0.1(\downarrow 0.0)\%;$$

Table 18. A summary of the $\bar{\psi}$, Ψ , and Φ values for the computation of the V2 primary variables.

Comparison		$\bar{\psi}(412)$	$\bar{\psi}(443)$	$\bar{\psi}(490)$	$\bar{\psi}(510)$	$\bar{\psi}(555)$	$\bar{\psi}(665)$	$\bar{\psi}(683)$	Ψ_{1-5}	Ψ_{6-7}	Ψ_{1-7}	$\Phi_{3/5}$
$L_u(0^-)$	JG (40)	0.7	0.6	0.5	0.5	0.5	1.8	1.7	0.5	1.7	0.9	0.1
	JS (40)	6.9	9.2	5.0	5.0	5.3	23.2	21.9	6.3	22.4	10.8	2.4
	GS (40)	6.5	8.9	4.8	4.7	5.2	23.0	21.7	6.0	21.9	10.5	2.4
OT	JG (50)	0.6	0.6	0.6	0.7	0.8	4.2	5.1	0.7	4.7	1.8	0.4
MT	JG (50)	0.5	0.5	0.4	0.4	0.4	2.1	1.9	0.4	2.0	0.9	0.1
ET	JG (50)	0.9	0.8	0.6	0.6	0.5	1.0	0.8	0.7	0.9	0.8	0.1
K_L	JG (40)	0.8	0.8	0.9	0.9	0.8	1.8	2.2	0.8	2.0	1.2	0.4
	OT JG (50)	3.3	4.0	4.2	3.7	2.5	5.7	7.1	3.5	6.4	4.3	2.4
	MT JG (50)	1.1	1.2	1.3	1.1	1.0	2.2	2.9	1.1	2.6	1.5	0.5
	ET JG (50)	0.3	0.4	0.4	0.4	0.4	0.5	0.4	0.4	0.5	0.4	0.1
$E_d(0^-)$	JG (40)	1.2	1.2	1.2	1.2	1.4	2.2	2.8	1.2	2.5	1.6	0.3
	JS (40)	11.3	11.2	11.0	10.9	12.7	32.4	31.3	11.4	32.8	16.9	4.3
	GS (40)	10.7	10.6	10.1	10.2	11.8	32.9	31.6	10.7	33.2	16.5	4.3
	OT JG (50)	2.5	2.6	2.6	2.7	2.8	3.6	2.9	2.6	3.3	2.8	0.3
	MT JG (50)	1.1	1.1	1.0	1.0	1.3	2.0	2.0	1.1	2.0	1.4	0.3
	ET JG (50)	0.9	0.9	1.1	0.9	1.2	2.0	3.9	1.0	3.0	1.6	0.1
K_d	JG (40)	2.8	3.4	4.2	3.2	2.9	0.8	0.9	3.2	0.8	2.5	1.6
	JS (40)	19.1	20.2	25.5	26.3	21.8	14.0	11.9	23.6	13.7	20.8	16.6
	GS (40)	18.9	19.4	23.8	25.3	20.7	13.9	11.6	22.6	13.5	20.1	16.8
	OT JG (50)	10.8	12.5	12.3	7.5	4.5	1.1	0.8	9.5	0.9	7.1	7.8
	MT JG (50)	2.3	3.0	3.4	3.2	2.9	1.0	0.8	3.0	0.9	2.3	1.1
	ET JG (50)	0.4	0.8	2.4	1.5	2.2	0.4	0.9	1.5	0.6	1.2	0.5
$E_d(0^+)$	JG (40)	0.2	0.3	0.2	0.3	0.3	0.3	0.2	0.3	0.3	0.3	0.1
	JS (40)	0.6	0.7	0.8	0.8	0.9	0.8	0.7	0.8	0.8	0.8	0.2
	GS (40)	0.6	0.7	0.6	0.7	0.8	0.7	0.6	0.7	0.6	0.7	0.2
	OT JG (50)	1.9	2.0	2.2	2.2	2.3	2.4	2.4	2.1	2.4	2.2	0.1
	MT JG (50)	0.2	0.4	0.2	0.4	0.3	0.3	0.2	0.3	0.3	0.3	0.1
	ET JG (50)	0.3	0.3	0.3	0.3	0.3	0.4	0.3	0.3	0.4	0.3	0.0
R_{rs}	JG (40)	1.4	1.3	1.2	1.3	1.1	3.2	2.7	1.3	2.9	1.7	0.2
	JS (40)	7.3	7.0	5.8	5.7	6.2	23.0	21.9	6.4	22.2	10.6	2.6
	GS (40)	6.5	6.4	5.1	4.9	5.6	22.5	22.2	5.7	22.0	10.1	2.6
	OT JG (50)	2.5	2.6	2.8	2.8	3.0	8.6	7.2	2.7	7.9	4.2	0.7
	MT JG (50)	1.2	1.2	1.1	1.2	1.0	3.3	2.9	1.2	3.1	1.7	0.3
	ET JG (50)	1.8	1.6	1.5	1.5	1.4	2.0	1.4	1.6	1.7	1.6	0.1
$[L_w]_N$	JG (40)	7.2	4.3	3.6	4.9	3.6	3.8		4.7	3.8	4.6	0.4
	JS (40)	10.3	9.2	8.0	5.7	7.0	22.6	21.6	8.0	21.9	11.8	4.2
	GS (40)	6.1	6.5	5.4	5.1	5.6	22.4		5.7	22.4	8.3	4.2
	OT JG (50)	7.1	4.7	4.3	6.4	4.6	5.3		5.4	5.3	5.4	0.5
	MT JG (50)	7.0	4.0	3.5	4.5	3.4	4.0		4.5	4.0	4.4	0.4
	ET JG (50)	7.7	4.7	3.7	5.4	3.9	3.6		5.1	3.6	4.8	0.3
$E_u(0^-)$	JG (40)	0.7	0.7	0.6	0.6	0.6	2.5	2.2	0.6	2.3	1.1	0.1
	OT JG (50)	0.4	0.4	0.5	0.6	0.7	4.7	5.0	0.5	4.8	1.8	0.2
	MT JG (50)	0.7	0.7	0.7	0.7	0.8	3.1	3.1	0.7	3.1	1.4	0.2
	ET JG (50)	0.7	0.6	0.4	0.4	0.4	0.9	0.6	0.5	0.7	0.6	0.1
$Q_n(0^-)$	JG (40)	0.4	0.4	0.4	0.5	0.5	1.0	1.0	0.4	1.0	0.6	0.2
	OT JG (50)	0.3	0.3	0.3	0.4	0.5	2.4	2.8	0.4	2.6	1.0	0.3
	MT JG (50)	0.4	0.5	0.5	0.6	0.7	1.2	1.2	0.5	1.2	0.7	0.2
	ET JG (50)	0.4	0.3	0.3	0.3	0.3	0.4	0.4	0.3	0.4	0.3	0.0
All	JG (40)	1.7	1.4	1.4	1.5	1.3	1.9	1.7	1.5	1.9	1.6	0.4

$$R_{rs} \Psi_{1-5} = 1.3(\downarrow 1.4)\%, \Psi_{6-7} = 2.0(\downarrow 11.6)\%, \text{ and } \Phi_{3/5} = 0.2(\downarrow 0.7)\%;$$

$$[L_W]_N \Psi_{1-5} = 4.7(\downarrow 0.3)\%, \Psi_{6-7} = 3.8(\downarrow 13.0)\%, \text{ and } \Phi_{3/5} = 0.4(\downarrow 0.6)\%;$$

$$E_u(0^-) \Psi_{1-5} = 0.6(\downarrow 1.8)\%, \Psi_{6-7} = 2.3(\downarrow 11.6)\%, \text{ and } \Phi_{3/5} = 0.1(\downarrow 0.6)\%;$$

$$Q_n(0^-) \Psi_{1-5} = 0.4(\downarrow 1.7)\%, \Psi_{6-7} = 1.0(\downarrow 3.9)\%, \text{ and } \Phi_{3/5} = 0.2(\downarrow 0.5)\%; \text{ and}$$

$$\text{All JG } \Psi_{1-5} = 1.5(\downarrow 2.8)\%, \Psi_{6-7} = 1.9(\downarrow 8.7)\%, \text{ and } \Phi_{3/5} = 0.4(\downarrow 1.4)\%.$$

Note the $E_d(0^+)$ uncertainties are the only ones that are unchanged.

In terms of the individual parameters, the largest reductions are in the red wavelengths, except for the K_d values for which the largest change is in the blue-green domain. The majority of the V2 uncertainties are less than 2.5%, and almost all of the band-ratio uncertainties are less than 1.0%. The exceptions are $E_d(0^-)$ at 683 nm, K_d for 412–555 nm, and $[L_W]_N$ for 412–683 nm. This excellent level of agreement is well summarized by the overall JG averages (along the very bottom of Table 18) which are all less than 2.5% (note the overall band-ratio average is less than 1.0%). The excellent JG uncertainties are a result of using the same extrapolation intervals with the JRC and GSFC different processors.

There is still a dependence in the uncertainties as a function of the concentration regimes. In general, the JG uncertainties decrease with increasing chlorophyll *a* concentration. Exceptions to this are the R_{rs} , $[L_W]_N$, blue-green $E_d(0^+)$, and blue-green $L_u(0^-)$ results for which the largest uncertainties are associated with the concentration regime end points (OT and ET). The $E_u(0^-)$ and the blue-green $Q_n(0^-)$ results show almost no dependence as a function of concentration regime.

1.6.2 V3 Summary

The only changes made for the V3 processing with respect to the V2 processing was to remove the $E_d(0^+)$ normalization usually used by the JRC processor, and to include 5° tilt filtering for the GSFC processor. A summary of the effects of these changes is shown in Table 19. In comparison to the V2 results (Table 18), there are improvements in most of the JG variables, but they are not as substantial as the changes between the V1 and V2 results—the Satlantic processor was not changed, so the JS and GS uncertainties are, again, largely unchanged.

The most significant aspect of the improvements is the the majority of the JG uncertainties are at the 1.0% level or less (the \uparrow symbol represents an increase in uncertainty with respect to the V2 values):

$$L_u(0^-) \Psi_{1-5} = 0.3(\downarrow 0.2)\%, \Psi_{6-7} = 0.5(\downarrow 1.2)\%, \text{ and } \Phi_{3/5} = 0.0(\downarrow 0.1)\%;$$

$$K_L \Psi_{1-5} = 0.2(\downarrow 0.6)\%, \Psi_{6-7} = 0.3(\downarrow 1.7)\%, \text{ and } \Phi_{3/5} = 0.0(\downarrow 0.4)\%;$$

$$E_d(0^-) \Psi_{1-5} = 0.5(\downarrow 0.7)\%, \Psi_{6-7} = 1.4(\downarrow 1.1)\%, \text{ and } \Phi_{3/5} = 0.2(\downarrow 0.1)\%;$$

$$K_d \Psi_{1-5} = 0.7(\downarrow 2.5)\%, \Psi_{6-7} = 0.4(\downarrow 0.4)\%, \text{ and } \Phi_{3/5} = 0.4(\downarrow 1.2)\%;$$

$$E_d(0^+) \Psi_{1-5} = 0.2(\downarrow 0.1)\%, \Psi_{6-7} = 0.2(\downarrow 0.1)\%, \text{ and } \Phi_{3/5} = 0.1(\downarrow 0.0)\%;$$

$$R_{rs} \Psi_{1-5} = 1.0(\downarrow 0.3)\%, \Psi_{6-7} = 2.1(\uparrow 0.1)\%, \text{ and } \Phi_{3/5} = 0.2(\downarrow 0.0)\%;$$

$$[L_W]_N \Psi_{1-5} = 4.6(\downarrow 0.1)\%, \Psi_{6-7} = 3.0(\downarrow 0.8)\%, \text{ and } \Phi_{3/5} = 0.4(\downarrow 0.0)\%;$$

$$E_u(0^-) \Psi_{1-5} = 0.2(\downarrow 0.4)\%, \Psi_{6-7} = 0.5(\downarrow 1.8)\%, \text{ and } \Phi_{3/5} = 0.0(\downarrow 0.1)\%;$$

$$Q_n(0^-) \Psi_{1-5} = 0.2(\downarrow 0.2)\%, \Psi_{6-7} = 0.3(\downarrow 0.7)\%, \text{ and } \Phi_{3/5} = 0.0(\downarrow 0.2)\%; \text{ and}$$

$$\text{All JG } \Psi_{1-5} = 0.9(\downarrow 0.6)\%, \Psi_{6-7} = 1.0(\downarrow 0.9)\%, \text{ and } \Phi_{3/5} = 0.1(\downarrow 0.3)\%.$$

All of the JG band-ratio uncertainties are below 1.0%—in fact, the overall band-ratio average is 0.1%. Almost all of the spectral uncertainties are at the 1.0% level or less, except a) the red $E_d(0^-)$ and R_{rs} values, b) some of the blue-green R_{rs} values are at 1.1%, and c) all of the $[L_W]_N$ values are greater than 2.5%. All of the spectral overall averages are at the 1.0% level or less, except at 412 nm for which the overall average is 1.2%.

There are still spectral dependencies in the results, but most of these are weak. For example, the difference between the maximum and minimum $L_u(0^-)$ uncertainty is 0.3%. Exceptions to this are seen for $E_d(0^-)$ and R_{rs} in the red domain, and $[L_W]_N$ in the blue-green. Overall, the difference between the maximum and minimum uncertainties for 412–683 nm is 0.5%, with most of the difference coming from the larger overall uncertainty at 412 nm.

The convergence of the processors is well quantified by considering the average difference in the number of points in the extrapolation ranges, $\Delta\bar{N}$, for the JRC and GSFC V3 processing of the SO, LN, WP, and MN data (the average number of points in the extrapolation range is given in parentheses):

$$\text{SO } \Delta\bar{N} = 5 \text{ (34)},$$

$$\text{LN } \Delta\bar{N} = 3 \text{ (61)},$$

$$\text{WP } \Delta\bar{N} = 2 \text{ (209)}, \text{ and}$$

$$\text{MN } \Delta\bar{N} = 0 \text{ (20)}.$$

Although the $\Delta\bar{N}$ values are small, the use of identical extrapolation ranges and very similar processing options does not result in exactly the same number of points in the extrapolation interval. The worst case is with Sea-OPS, but this is an instrument that is going up and down as a result of wave action (acting on the ship) as it is deployed. The surging motion can occur at an extrapolation boundary, and how the processors deal with the addition of new data after the boundary is first encountered can be different. The best case is with miniNESS data, where

Table 19. A summary of the $\bar{\psi}$, Ψ , and Φ values for the computation of the V3 primary variables.

Comparison		$\bar{\psi}(412)$	$\bar{\psi}(443)$	$\bar{\psi}(490)$	$\bar{\psi}(510)$	$\bar{\psi}(555)$	$\bar{\psi}(665)$	$\bar{\psi}(683)$	Ψ_{1-5}	Ψ_{6-7}	Ψ_{1-7}	$\Phi_{3/5}$
$L_u(0^-)$	JG (40)	0.4	0.3	0.2	0.2	0.2	0.5	0.4	0.3	0.5	0.3	0.0
	JS (40)	6.8	9.1	5.0	4.9	5.3	23.2	21.9	6.3	22.3	10.8	2.4
	GS (40)	6.6	9.0	4.9	4.8	5.2	23.0	21.8	6.1	22.2	10.7	2.4
OT	JG (50)	0.1	0.1	0.1	0.2	0.3	1.1	1.3	0.2	1.2	0.5	0.1
MT	JG (50)	0.1	0.1	0.1	0.1	0.1	0.2	0.2	0.1	0.2	0.1	0.0
ET	JG (50)	0.8	0.7	0.5	0.5	0.5	1.1	0.6	0.6	0.9	0.7	0.1
K_L	JG (40)	0.2	0.2	0.2	0.2	0.2	0.3	0.4	0.2	0.3	0.2	0.0
	OT JG (50)	0.4	0.5	0.4	0.4	0.3	0.8	1.2	0.4	1.0	0.6	0.3
	MT JG (50)	0.1	0.1	0.2	0.2	0.1	0.3	0.4	0.1	0.3	0.2	0.1
	ET JG (50)	0.2	0.2	0.2	0.2	0.2	0.4	0.3	0.2	0.4	0.2	0.0
$E_d(0^-)$	JG (40)	0.6	0.6	0.5	0.5	0.5	1.2	1.7	0.5	1.4	0.8	0.2
	JS (40)	11.2	11.2	11.0	10.9	12.7	32.4	31.3	11.4	32.8	16.9	4.3
	GS (40)	11.2	11.2	10.8	10.8	12.5	32.9	32.0	11.3	33.4	17.0	4.3
	OT JG (50)	0.2	0.2	0.3	0.3	0.3	0.6	0.4	0.3	0.5	0.3	0.1
	MT JG (50)	0.3	0.3	0.3	0.3	0.4	0.7	0.7	0.3	0.7	0.4	0.1
	ET JG (50)	1.0	1.0	0.9	0.7	0.8	2.0	3.5	0.9	2.8	1.4	0.2
K_d	JG (40)	0.5	0.6	0.9	0.8	0.7	0.4	0.4	0.7	0.4	0.6	0.4
	JS (40)	19.1	20.3	25.6	26.5	22.0	14.1	11.9	23.8	13.7	20.9	16.6
	GS (40)	19.0	20.3	25.4	26.3	21.8	14.0	11.9	23.6	13.7	20.7	16.9
	OT JG (50)	0.9	1.1	1.3	0.9	0.6	0.2	0.2	1.0	0.2	0.7	0.7
	MT JG (50)	0.6	0.7	1.0	1.2	1.0	0.4	0.3	0.9	0.3	0.7	0.3
	ET JG (50)	0.3	0.4	0.8	0.4	0.4	0.4	0.6	0.5	0.5	0.5	0.6
$E_d(0^+)$	JG (40)	0.1	0.3	0.2	0.3	0.2	0.2	0.2	0.2	0.2	0.2	0.1
	JS (40)	0.5	0.6	0.7	0.7	0.8	0.7	0.6	0.7	0.6	0.6	0.2
	GS (40)	0.6	0.7	0.6	0.7	0.8	0.7	0.6	0.7	0.6	0.7	0.2
	OT JG (50)	1.5	1.6	1.8	1.8	1.8	1.9	1.9	1.7	1.9	1.8	0.1
	MT JG (50)	0.1	0.3	0.1	0.3	0.2	0.3	0.1	0.2	0.2	0.2	0.1
	ET JG (50)	0.2	0.2	0.2	0.2	0.2	0.2	0.2	0.2	0.2	0.2	0.0
R_{rs}	JG (40)	1.1	1.1	1.0	1.1	1.0	2.0	2.2	1.0	2.1	1.3	0.2
	JS (40)	7.2	6.9	5.6	5.6	6.1	22.9	21.9	6.3	22.1	10.6	2.6
	GS (40)	6.6	6.5	5.1	5.0	5.6	22.2	21.8	5.8	21.6	10.1	2.6
	OT JG (50)	1.8	2.0	2.1	2.2	2.2	6.5	5.0	2.1	5.7	3.1	0.4
	MT JG (50)	0.8	0.9	0.8	1.0	0.8	1.8	2.1	0.9	2.0	1.2	0.2
	ET JG (50)	1.5	1.4	1.2	1.2	1.2	1.9	1.2	1.3	1.5	1.4	0.1
$[L_w]_N$	JG (40)	7.1	4.2	3.4	4.8	3.5	3.0		4.6	3.0	4.3	0.4
	JS (40)	10.3	9.1	7.9	5.6	6.8	22.6	21.5	8.0	21.8	11.7	4.1
	GS (40)	6.2	6.6	5.6	5.0	5.6	22.4		5.8	22.4	8.3	4.2
	OT JG (50)	6.4	4.0	3.6	5.6	3.9	3.6		4.7	3.6	4.5	0.3
	MT JG (50)	6.8	3.9	3.4	4.4	3.3	2.6		4.4	2.6	4.1	0.4
	ET JG (50)	7.5	4.6	3.6	5.3	3.8	3.6		5.0	3.6	4.7	0.3
$E_u(0^-)$	JG (40)	0.3	0.2	0.2	0.2	0.2	0.5	0.4	0.2	0.5	0.3	0.0
	OT JG (50)	0.0	0.0	0.0	0.0	0.0	0.2	0.5	0.0	0.4	0.1	0.0
	MT JG (50)	0.2	0.2	0.1	0.1	0.2	0.4	0.4	0.2	0.4	0.2	0.0
	ET JG (50)	0.5	0.4	0.3	0.3	0.3	0.8	0.5	0.4	0.6	0.4	0.1
$Q_n(0^-)$	JG (40)	0.2	0.2	0.2	0.2	0.2	0.3	0.3	0.2	0.3	0.2	0.0
	OT JG (50)	0.1	0.1	0.1	0.2	0.2	1.0	1.4	0.2	1.2	0.5	0.1
	MT JG (50)	0.2	0.1	0.1	0.1	0.2	0.2	0.3	0.1	0.2	0.2	0.0
	ET JG (50)	0.3	0.3	0.3	0.3	0.3	0.3	0.3	0.3	0.3	0.3	0.0
All	JG (40)	1.2	0.8	0.8	0.9	0.7	0.9	0.7	0.9	1.0	0.9	0.1

the vertical resolution and extrapolation range are minimized. Between these two, the processors are basically differing by one or two points at each extrapolation boundary. Differences at this level are to be expected, because the processors can be using different numerical precision in the calculation of depth, absolute or nearest neighbor limits can be employed for the boundaries, etc.

Although there are variables for which the uncertainties either increase or decrease with increasing concentration, the majority do not show a significant dependence, i.e., the difference between the maximum and minimum uncertainty for the OT, MT, and ET results is usually less than 1.0%. Notable exceptions are $E_d(0^+)$, R_{rs} , and $[L_W]_N$. The $E_d(0^+)$ result is associated with maximum uncertainties in the OT data which are composed solely of deep ocean data using unstabilized references. The R_{rs} result is due to maximal uncertainties in the ET $L_u(0^-)$ data and the OT $E_d(0^+)$ data. The $[L_W]_N$ result is a consequence of the aforementioned differences in the $\bar{F}_0(\lambda)$ coefficients.

The DO, SC, WC, and FF partitioning of the V3 JG results (using the 50-cast data set) are presented in Fig. 13. The dashed lines set the 2.5% intercomparison objective and the dotted lines the 1.0% objective (plotted within the 4% uncertainty range achieved with DARR-94, except for the normalized water-leaving radiance which has an expanded scale). In terms of the uncertainty levels, the variables can be separated into three groups: the first group is composed of variables with uncertainties always less than 1.0%, i.e., K_L , $E_u(0^-)$, and $Q_n(0^-)$; the second group has uncertainties frequently below 1%, with a few wavelengths slightly above 1%, i.e., $L_u(0^-)$, $E_d(0^-)$, K_d , $E_d(0^+)$, and $R(0^-)$; and the third group has uncertainties persistently above 1%, and even 2.5%, i.e., R_{rs} and $[L_W]_N$.

The uncertainties within the first group are so small and so similar, the differences within the various categories are probably not significant. There are, however, two notable results associated with this group: a) the largest uncertainties are in the red wavelengths, and b) the Q_n -factor is the only multivariate (i.e., normalized) parameter with uncertainties persistently below the 1.0% level.

Within the second group, the differences between the various categories are more substantial: a) the shallow coastal data usually have lower uncertainties than the deep ocean data; b) the free-fall data usually have lower uncertainties than the winch and crane data; and c) the SC and FF $L_u(0^-)$, $E_d(0^-)$, $E_d(0^+)$, and $R(0^-)$ uncertainties are always less than 1.0% (even though the corresponding DO and WC values are not).

The third group is important, because it consists of parameters central to calibration and validation activities, $[L_W]_N$ and R_{rs} , respectively. Unfortunately, both variables are associated with the largest uncertainties. The normalized water-leaving radiances have large uncertainties, because of the differences in $\bar{F}_0(\lambda)$, as discussed in Sect. 1.5.6. The R_{rs} uncertainties are only large for the DO and WC categories—the SC uncertainties are always

less than 1.0%, and the FF uncertainties are less than 1.0% in the blue-green domain (including the band-ratio value).

There is also a general result supported by all three groups: the SC and FF uncertainties are less than the DO and WC values, respectively. The lower uncertainties with the SC data are a consequence of comparatively higher uncertainties for the SO data. The processing uncertainties for the JG (40-cast) data sets organized according to the four instrument types, are presented in Table 20 along with samples of the SO and LN uncertainties for the 50-cast data set. These samples show the differences between the two data sets for the SO and LN results are small and the general properties of the data (e.g., spectral dependence, overall averages, band ratios, etc.) are similar.

For the $L_u(0^-)$, $E_d(0^-)$, R_{rs} , $E_u(0^-)$, and $Q_n(0^-)$ variables, SO uncertainties are significantly larger than the LN, WP, and MN uncertainties. If the SO uncertainties are ignored, the latter three usually agree to within 0.5% (except for the red R_{rs} wavelengths).

The K_L , $E_d(0^+)$, $[L_W]_N$, and $R(0^+)$ uncertainties in Table 20 do not show any significant dependence as a function of the instrument type. Interestingly, the SO K_L uncertainties are not distinguishable from the other instrument types even though the SO $L_u(0^-)$ uncertainties are. The low $E_d(0^+)$ uncertainties suggest the difference between stabilized and unstabilized references does not effect the processing uncertainties (when the processing options are made similar). The $[L_W]_N$ uncertainties do not show a strong sensitivity to instrument type, but the smallest values are usually associated with the LN data. In comparison, the $R(0^+)$ uncertainties also do not show a strong sensitivity to instrument type, but the largest values are usually associated with the LN data.

As was seen with the K_L and $L_u(0^-)$ data, the K_d uncertainties do not follow the instrument dependence for $E_d(0^-)$: the largest K_d uncertainties are associated with the WP data, whereas the largest $E_d(0^-)$ uncertainties are for the SO data. Given the direct importance of the attenuation coefficients in determining the extrapolated (null depth) values, it is interesting that the uncertainties for the two are not always commensurate. As with the V1 and V2 results, the K_d uncertainties in the red domain are significantly smaller than the blue-green uncertainties.

The effect of processor convergence on the intercomparison of the OC2v2 determination of total chlorophyll *a* between the JRC and GSFC data processors is as follows:

SO 2.7%,
LN 7.0%,
WP 5.2%, and
MN 7.2%,

with an overall average of 5.5%. These are very similar to the V1 results (Table 15), so even though the intercomparison of many of the primary optical variables has improved significantly, the net effect on the derived (OC2v2) chlorophyll concentration is minimal. For comparison purposes,

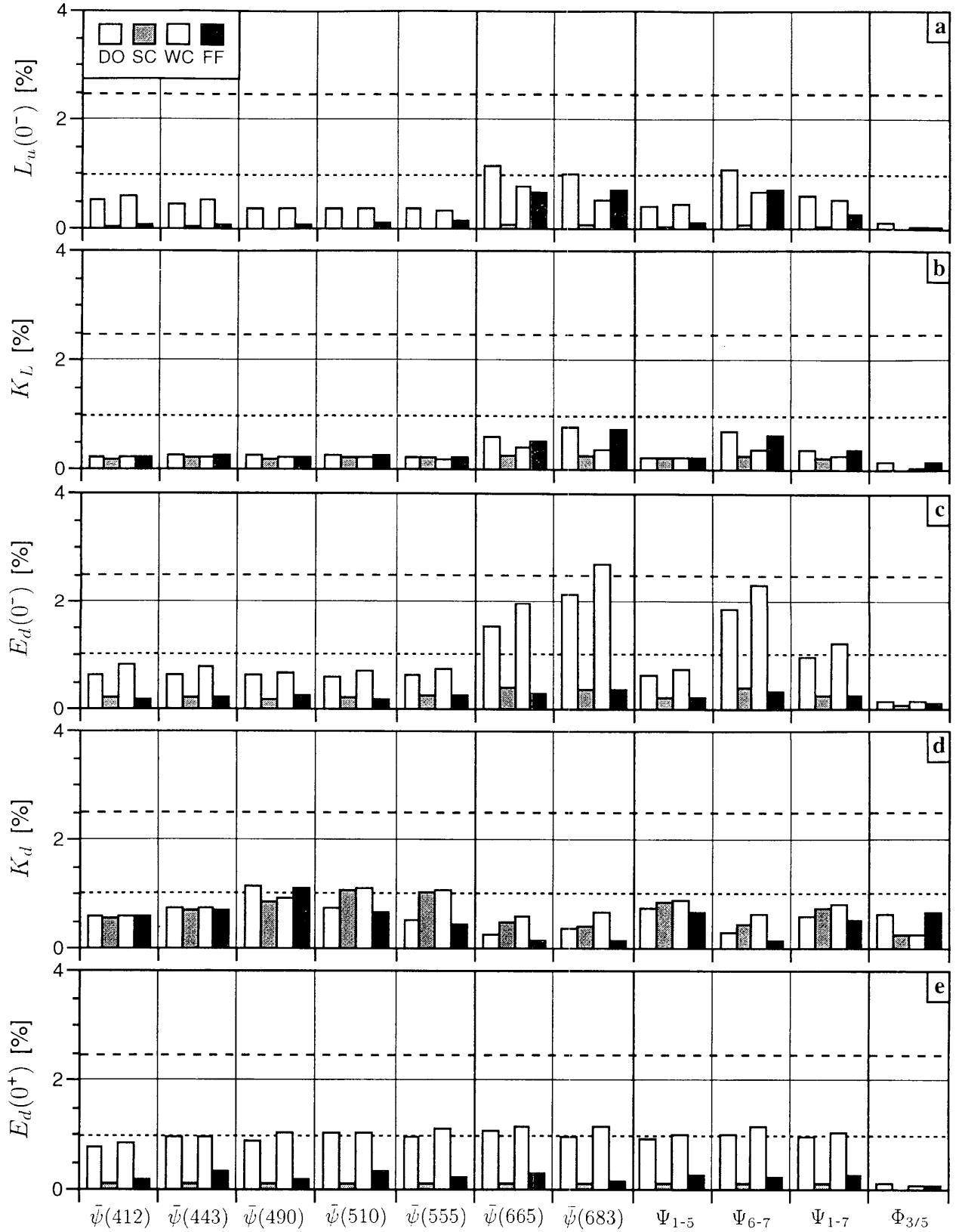


Fig. 13. Average V3 processing uncertainties in the primary JG intercomparison variables for the DO (light gray bars), SC (dark gray bars), WC (white bars), and FF (black bars) data categories: a) $L_u(0^-)$, b) K_L , c) $E_d(0^-)$, d) K_d , and e) $E_d(0^+)$.

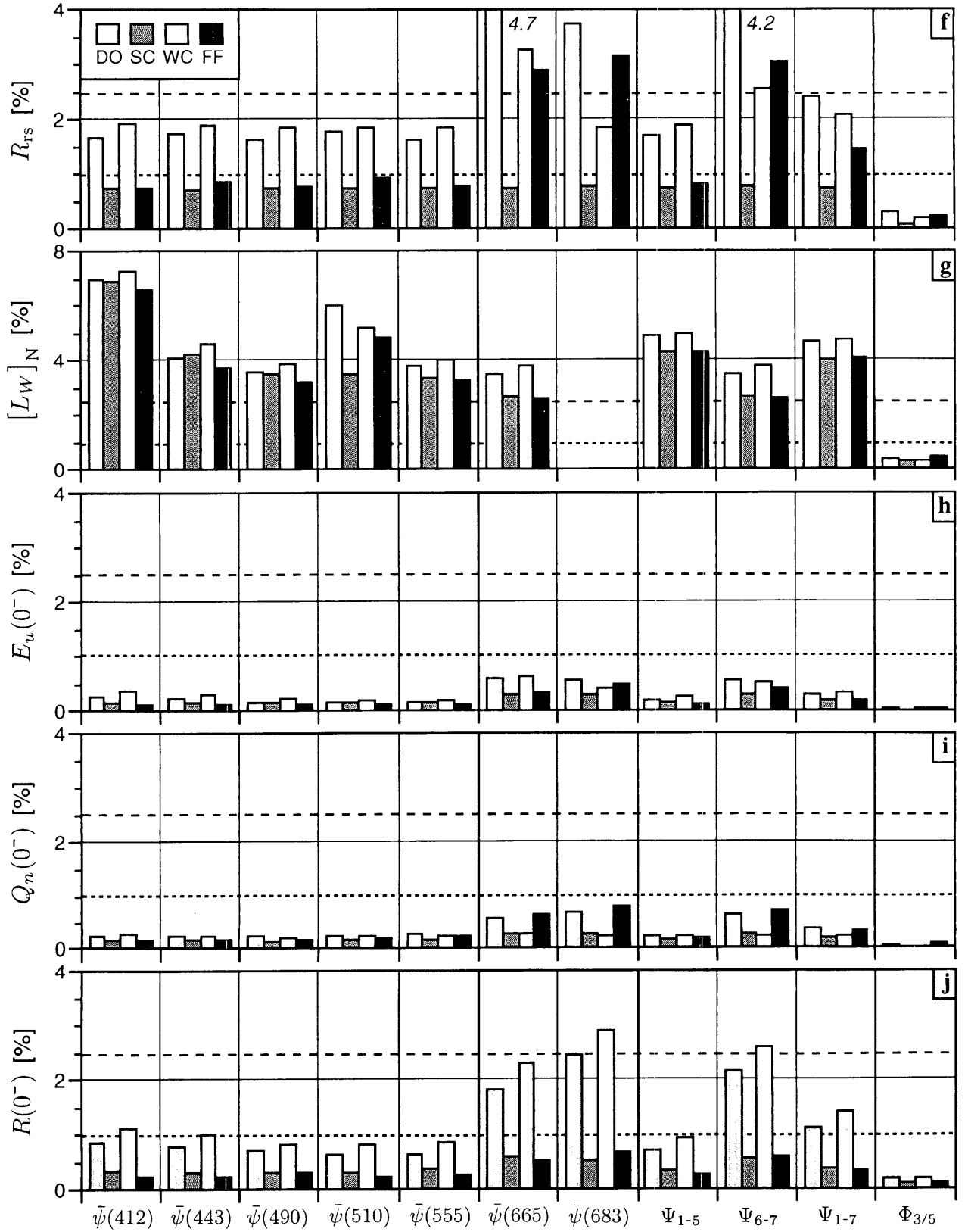


Fig. 13. (cont.) Average V3 processing uncertainties in the primary JG intercomparison variables for the DO (light gray bars), SC (dark gray bars), WC (white bars), and FF (black bars) data categories: f) R_{rs} , g) $[L_w(\lambda)]_N$, h) $E_u(0^-)$, i) $Q_n(0^-)$, and j) $R(0^-)$.

Table 20. A summary of the $\bar{\psi}$, Ψ , and Φ values for the V3 primary variables. The comparisons are for the JG 40-cast data set, with samples from the 50-cast data set, organized according to the four instrument types.

Comparison		$\bar{\psi}(412)$	$\bar{\psi}(443)$	$\bar{\psi}(490)$	$\bar{\psi}(510)$	$\bar{\psi}(555)$	$\bar{\psi}(665)$	$\bar{\psi}(683)$	Ψ_{1-5}	Ψ_{6-7}	Ψ_{1-7}	$\Phi_{3/5}$
$L_u(0^-)$	SO (40)	1.3	1.2	0.9	0.8	0.8	1.6	1.0	1.0	1.3	1.1	0.1
	LN (40)	0.1	0.1	0.1	0.1	0.1	0.4	0.3	0.1	0.4	0.2	0.0
	WP (40)	0.1	0.0	0.0	0.0	0.0	0.1	0.1	0.0	0.1	0.1	0.0
	MN (40)	0.0	0.0	0.0	0.0	0.0	0.1	0.1	0.0	0.1	0.0	0.0
	SO (50)	1.0	0.9	0.7	0.6	0.6	1.3	0.9	0.8	1.1	0.9	0.1
	LN (50)	0.1	0.1	0.1	0.2	0.2	1.0	1.1	0.2	1.0	0.4	0.1
K_L	SO (40)	0.1	0.1	0.1	0.1	0.1	0.5	0.4	0.1	0.4	0.2	0.1
	LN (40)	0.1	0.2	0.2	0.2	0.2	0.3	0.5	0.2	0.4	0.2	0.1
	WP (40)	0.3	0.4	0.3	0.4	0.4	0.4	0.4	0.3	0.4	0.4	0.0
	MN (40)	0.1	0.1	0.1	0.1	0.1	0.1	0.1	0.1	0.1	0.1	0.0
$E_d(0^-)$	SO (40)	1.4	1.3	1.1	1.2	1.2	3.4	5.3	1.2	4.4	2.1	0.1
	LN (40)	0.4	0.4	0.5	0.4	0.4	0.5	0.7	0.4	0.6	0.5	0.3
	WP (40)	0.4	0.4	0.4	0.4	0.5	0.8	0.7	0.4	0.7	0.5	0.2
	MN (40)	0.0	0.0	0.0	0.0	0.0	0.1	0.1	0.0	0.1	0.0	0.0
K_d	SO (40)	0.2	0.2	0.4	0.4	0.4	0.3	0.7	0.3	0.5	0.4	0.1
	LN (40)	0.7	0.8	1.6	0.8	0.5	0.1	0.2	0.8	0.2	0.6	1.0
	WP (40)	1.1	1.3	1.6	2.0	2.0	0.9	0.8	1.6	0.8	1.4	0.4
	MN (40)	0.1	0.0	0.1	0.1	0.1	0.1	0.1	0.1	0.1	0.1	0.0
	SO (50)	0.2	0.3	0.4	0.4	0.4	0.4	0.6	0.3	0.5	0.4	0.1
	LN (50)	0.9	1.1	1.7	1.0	0.7	0.2	0.2	1.0	0.2	0.8	1.1
$E_d(0^+)$	SO (40)	0.1	0.1	0.2	0.2	0.2	0.2	0.2	0.1	0.2	0.2	0.0
	LN (40)	0.2	0.7	0.2	0.6	0.4	0.6	0.2	0.4	0.4	0.4	0.2
	WP (40)	0.2	0.2	0.2	0.2	0.2	0.2	0.2	0.2	0.2	0.2	0.0
	MN (40)	0.0	0.0	0.0	0.0	0.0	0.0	0.0	0.0	0.0	0.0	0.0
R_{rs}	SO (40)	2.1	1.9	1.6	1.5	1.4	2.8	1.9	1.7	2.3	1.9	0.2
	LN (40)	0.7	1.1	0.9	1.2	0.9	3.9	5.2	1.0	4.6	2.0	0.4
	WP (40)	0.8	0.7	0.8	0.7	0.8	0.7	0.8	0.8	0.7	0.7	0.1
	MN (40)	0.7	0.7	0.7	0.7	0.8	0.8	0.8	0.7	0.8	0.8	0.1
	SO (50)	2.8	2.8	2.7	2.7	2.7	5.3	2.7	2.8	4.0	3.1	0.3
	LN (50)	0.7	0.9	0.8	1.1	0.8	4.2	4.6	0.9	4.4	1.9	0.3
$[L_w]_N$	SO (40)	8.0	4.8	3.8	6.5	4.1	4.0	0.0	5.5	4.0	5.2	0.3
	LN (40)	6.5	3.4	3.0	5.8	3.2	2.5	0.0	4.4	2.5	4.1	0.6
	WP (40)	7.0	4.3	3.3	3.8	3.4	2.6	0.0	4.4	2.6	4.1	0.3
	MN (40)	6.7	4.2	3.6	3.3	3.4	2.7	0.0	4.2	2.7	4.0	0.4
	SO (50)	7.4	4.9	4.3	6.3	4.6	4.6	0.0	5.5	4.6	5.3	0.3
	LN (50)	6.6	3.5	3.0	5.8	3.2	2.6	0.0	4.4	2.6	4.1	0.4
$E_u(0^-)$	SO (40)	0.8	0.7	0.5	0.4	0.4	1.3	0.7	0.5	1.0	0.7	0.1
	LN (40)	0.0	0.0	0.0	0.0	0.0	0.3	0.4	0.0	0.4	0.1	0.0
	WP (40)	0.1	0.1	0.0	0.0	0.0	0.1	0.1	0.1	0.1	0.1	0.0
	MN (40)	0.3	0.3	0.2	0.3	0.3	0.5	0.5	0.3	0.5	0.3	0.0
$Q_n(0^-)$	SO (40)	0.5	0.5	0.4	0.4	0.4	0.4	0.4	0.5	0.4	0.4	0.0
	LN (40)	0.0	0.0	0.0	0.1	0.1	0.1	0.1	0.1	0.1	0.1	0.0
	WP (40)	0.0	0.0	0.0	0.0	0.0	0.1	0.1	0.0	0.1	0.1	0.0
	MN (40)	0.2	0.2	0.2	0.2	0.3	0.5	0.5	0.2	0.5	0.3	0.0
$R(0^-)$	SO (40)	0.1	0.1	0.2	0.2	0.2	0.2	0.2	0.1	0.2	0.2	0.0
	LN (40)	0.2	0.7	0.2	0.6	0.4	0.6	0.2	0.4	0.4	0.4	0.2
	WP (40)	0.2	0.2	0.2	0.2	0.2	0.2	0.2	0.2	0.2	0.2	0.0
	MN (40)	0.0	0.0	0.0	0.0	0.0	0.0	0.0	0.0	0.0	0.0	0.0

the JS and GS average uncertainties for the OC2v2 intercomparison are 12.2 and 14.2%, respectively, which are very similar to the V1 results.

1.6.3 V4 Summary

The only change made for the V4 processing with respect to the V3 processing was to use a robust linear fit for the GSFC processor. The robust linear fit weights the data in the extrapolation interval to minimize the significance of data points with higher variance, which acts as a mild form of outlier rejection. The effects of this change are presented in Table 21. In comparison to the very low uncertainties achieved with the V3 results (Table 19), there are comparatively large increases in the uncertainties of the JG variables—the Satlantic processor was not changed, so the JS and GS uncertainties are, again, largely unchanged.

The most significant aspect of the change in uncertainties for the V4 processing is the majority of the JG uncertainties are no longer at the 1.0% level or less, although many are to within 2.5%:

$$\begin{aligned}
 L_u(0^-) \quad \Psi_{1-5} &= 0.8(\uparrow 0.5)\%, \quad \Psi_{6-7} = 2.2(\uparrow 1.7)\%, \text{ and} \\
 &\quad \Phi_{3/5} = 0.5(\uparrow 0.5)\%; \\
 K_L \quad \Psi_{1-5} &= 1.5(\uparrow 1.3)\%, \quad \Psi_{6-7} = 2.2(\uparrow 1.9)\%, \text{ and} \\
 &\quad \Phi_{3/5} = 1.1(\uparrow 1.1)\%; \\
 E_d(0^-) \quad \Psi_{1-5} &= 2.8(\uparrow 2.3)\%, \quad \Psi_{6-7} = 3.8(\uparrow 2.4)\%, \text{ and} \\
 &\quad \Phi_{3/5} = 2.2(\uparrow 2.0)\%; \\
 K_d \quad \Psi_{1-5} &= 6.4(\uparrow 5.7)\%, \quad \Psi_{6-7} = 2.0(\uparrow 1.6)\%, \text{ and} \\
 &\quad \Phi_{3/5} = 8.9(\uparrow 8.5)\%; \\
 E_d(0^+) \quad \Psi_{1-5} &= 0.2(\uparrow 0.0)\%, \quad \Psi_{6-7} = 0.2(\uparrow 0.0)\%, \text{ and} \\
 &\quad \Phi_{3/5} = 0.1(\uparrow 0.0)\%; \\
 R_{rs} \quad \Psi_{1-5} &= 1.2(\uparrow 0.2)\%, \quad \Psi_{6-7} = 3.0(\uparrow 0.9)\%, \text{ and} \\
 &\quad \Phi_{3/5} = 0.5(\uparrow 0.3)\%; \\
 [L_W]_N \quad \Psi_{1-5} &= 4.6(\uparrow 0.0)\%, \quad \Psi_{6-7} = 4.1(\uparrow 1.1)\%, \text{ and} \\
 &\quad \Phi_{3/5} = 0.6(\uparrow 0.2)\%; \\
 E_u(0^-) \quad \Psi_{1-5} &= 0.7(\uparrow 0.5)\%, \quad \Psi_{6-7} = 2.5(\uparrow 2.0)\%, \text{ and} \\
 &\quad \Phi_{3/5} = 0.4(\uparrow 0.4)\%; \\
 Q_n(0^-) \quad \Psi_{1-5} &= 0.9(\uparrow 0.7)\%, \quad \Psi_{6-7} = 2.3(\uparrow 2.0)\%, \text{ and} \\
 &\quad \Phi_{3/5} = 0.6(\uparrow 0.6)\%; \text{ and} \\
 \text{All JG} \quad \Psi_{1-5} &= 2.1(\uparrow 1.2)\%, \quad \Psi_{6-7} = 2.5(\uparrow 1.5)\%, \text{ and} \\
 &\quad \Phi_{3/5} = 1.7(\uparrow 1.6)\%.
 \end{aligned}$$

The R_{rs} and $[L_W]_N$ uncertainties are not very different in terms of the percent increase of the V4 results with respect to the V3 results. The $E_d(0^+)$ uncertainties are unchanged, because there is nothing in the robust linear fitting that can influence the calculation of $E_d(0^+)$. The R_{rs} and $[L_W]_N$ are not strongly altered (from a percent change point of view), because the normalizing variable, $E_d(0^+)$, is unchanged, and the absolute increases in the $L_u(0^-)$ uncertainties are proportionately smaller, particularly for $[L_W]_N$.

Although the JG $L_u(0^-)$ and K_L uncertainties show similar increases, the increases in the $E_d(0^-)$ and K_d uncertainties are considerably different. This shows the type

of fit is sensitive to the amount of noise in the data—the $E_d(0^-)$ data are noisier than the $L_u(0^-)$ data, because of wave focusing effects. This can also be seen in the concentration regime data. The $L_u(0^-)$ uncertainties do not show a clear trend as a function of concentration, but the $E_d(0^-)$ uncertainties decrease as concentration increases.

In most cases, the band-ratio uncertainties are much less than the spectral uncertainties, and most are less than 1.0%. The notable exception is the K_d results for which the band-ratio uncertainty is very large and responsible for increasing the overall band-ratio uncertainty above 1.0% (but still within 2.5%). The latter is caused by the significantly larger K_d uncertainties in the blue-green domain.

The sensitivity of the primary variables to chlorophyll *a* concentration is a mixture of increasing and decreasing uncertainties as a function of increasing concentration. Perhaps the most significant results in this regard are the very large K_d uncertainties in the OT and even the MT regimes. This points to the difficulty of estimating the slope of the log-transformed light data in clear waters where surface effects add a considerable amount of noise to the data.

1.6.4 V5 Summary

The primary purpose of the V5 processing configuration was to investigate the importance of filtering on the uncertainties, so the GSFC processor was set to its usual configuration (no tilt filtering and no outlier filtering), and the JRC processor was changed slightly: tilt filtering was enabled (as usual), but outlier filtering was disabled (usually outlier filtering was enabled). A summary of the processing options is given in Table 17, and the effects of the V5 changes is shown in Table 22. In comparison to the V3 results (Table 19), there are increases in uncertainties for most of the JG variables, but they are not as substantial as the changes seen with the V4 results (Table 21)—the Satlantic processor was not modified, so the JS and GS uncertainties remain largely unchanged.

The most significant aspect of the change in uncertainties for the V5 processing with respect to the V3 processing is there is an overall increase in uncertainty values, but the majority of the JG uncertainties for the blue-green wavelengths are within, or close to, the 1.0% level, and most of the uncertainties in the red domain are less than 2.5%:

$$\begin{aligned}
 L_u(0^-) \quad \Psi_{1-5} &= 0.5(\uparrow 0.2)\%, \quad \Psi_{6-7} = 1.7(\uparrow 1.2)\%, \text{ and} \\
 &\quad \Phi_{3/5} = 0.1(\uparrow 0.1)\%; \\
 K_L \quad \Psi_{1-5} &= 0.7(\uparrow 0.5)\%, \quad \Psi_{6-7} = 1.9(\uparrow 1.6)\%, \text{ and} \\
 &\quad \Phi_{3/5} = 0.3(\uparrow 0.3)\%; \\
 E_d(0^-) \quad \Psi_{1-5} &= 1.2(\uparrow 0.7)\%, \quad \Psi_{6-7} = 2.4(\uparrow 1.0)\%, \text{ and} \\
 &\quad \Phi_{3/5} = 0.3(\uparrow 0.1)\%; \\
 K_d \quad \Psi_{1-5} &= 3.0(\uparrow 2.3)\%, \quad \Psi_{6-7} = 0.8(\uparrow 0.4)\%, \text{ and} \\
 &\quad \Phi_{3/5} = 1.5(\uparrow 1.1)\%; \\
 E_d(0^+) \quad \Psi_{1-5} &= 0.2(\uparrow 0.0)\%, \quad \Psi_{6-7} = 0.2(\uparrow 0.0)\%, \text{ and} \\
 &\quad \Phi_{3/5} = 0.1(\uparrow 0.0)\%;
 \end{aligned}$$

Table 21. A summary of the $\bar{\psi}$, Ψ , and Φ values for the computation of the V4 primary variables.

Comparison		$\bar{\psi}(412)$	$\bar{\psi}(443)$	$\bar{\psi}(490)$	$\bar{\psi}(510)$	$\bar{\psi}(555)$	$\bar{\psi}(665)$	$\bar{\psi}(683)$	Ψ_{1-5}	Ψ_{6-7}	Ψ_{1-7}	$\Phi_{3/5}$
$L_u(0^-)$	JG (40)	0.9	0.8	0.8	0.8	0.8	2.2	2.2	0.8	2.2	1.2	0.5
	JS (40)	6.8	9.1	5.0	4.9	5.3	23.2	21.9	6.3	22.3	10.8	2.4
	GS (40)	6.7	9.0	4.9	4.8	5.3	23.4	22.1	6.2	22.5	10.8	2.3
	OT JG (50)	0.4	0.6	0.6	0.7	1.2	6.2	7.1	0.7	6.7	2.4	1.2
	MT JG (50)	0.5	0.5	0.6	0.6	0.7	2.0	1.9	0.6	1.9	1.0	0.4
	ET JG (50)	1.5	1.3	1.0	1.0	0.9	2.3	2.0	1.1	2.1	1.4	0.5
K_L	JG (40)	0.9	1.2	1.7	1.6	1.9	1.7	2.6	1.5	2.2	1.7	1.1
	OT JG (50)	1.1	2.0	2.4	2.0	3.0	6.8	9.0	2.1	7.9	3.8	3.3
	MT JG (50)	1.1	1.2	2.0	2.1	2.2	1.8	2.5	1.7	2.1	1.8	0.8
	ET JG (50)	0.7	0.9	0.9	0.9	1.0	1.2	1.4	0.9	1.3	1.0	0.6
$E_d(0^-)$	JG (40)	2.6	2.8	2.7	3.0	2.7	3.3	4.2	2.8	3.8	3.0	2.2
	JS (40)	11.2	11.2	11.0	10.9	12.7	32.4	31.3	11.4	32.8	16.9	4.3
	GS (40)	11.1	11.1	10.7	11.0	12.4	33.8	32.2	11.3	33.8	17.0	5.2
	OT JG (50)	4.0	4.2	4.7	5.0	5.1	4.0	5.3	4.6	4.6	4.6	2.7
	MT JG (50)	2.8	2.6	2.8	3.5	3.4	3.8	4.1	3.0	3.9	3.3	2.3
	ET JG (50)	2.0	2.7	2.0	1.7	1.5	2.7	4.7	2.0	3.7	2.5	1.6
K_d	JG (40)	4.2	5.4	10.1	6.7	5.7	1.7	2.3	6.4	2.0	5.1	8.9
	JS (40)	19.1	20.3	25.6	26.5	22.0	14.1	11.9	23.8	13.7	20.9	16.6
	GS (40)	19.5	18.9	28.4	26.3	23.5	14.6	12.3	24.2	14.2	21.3	21.2
	OT JG (50)	19.5	20.1	19.4	10.6	7.4	1.3	1.1	15.4	1.2	11.3	13.2
	MT JG (50)	5.8	7.2	12.8	9.0	8.0	2.4	3.2	8.6	2.8	6.8	11.8
	ET JG (50)	1.1	2.0	3.2	2.6	2.4	0.9	1.3	2.3	1.1	1.9	2.4
$E_d(0^+)$	JG (40)	0.1	0.3	0.2	0.3	0.2	0.2	0.2	0.2	0.2	0.2	0.1
	JS (40)	0.5	0.6	0.7	0.7	0.8	0.7	0.6	0.7	0.6	0.6	0.2
	GS (40)	0.6	0.7	0.6	0.7	0.8	0.7	0.6	0.7	0.6	0.7	0.2
	OT JG (50)	1.5	1.6	1.8	1.8	1.8	1.9	1.9	1.7	1.9	1.8	0.1
	MT JG (50)	0.1	0.3	0.1	0.3	0.2	0.3	0.1	0.2	0.2	0.2	0.1
	ET JG (50)	0.2	0.2	0.2	0.2	0.2	0.2	0.2	0.2	0.2	0.2	0.0
R_{rs}	JG (40)	1.2	1.2	1.0	1.3	1.2	3.0	3.1	1.2	3.0	1.7	0.5
	JS (40)	7.2	6.9	5.6	5.6	6.1	22.9	21.9	6.3	22.1	10.6	2.6
	GS (40)	6.7	6.5	5.2	5.0	5.6	23.1	22.4	5.8	22.4	10.3	2.6
	OT JG (50)	1.7	1.9	2.2	2.4	3.0	6.5	7.7	2.2	7.1	3.6	1.2
	MT JG (50)	1.0	1.1	0.9	1.2	1.1	2.9	3.3	1.1	3.1	1.6	0.3
	ET JG (50)	1.7	1.5	1.3	1.5	1.3	2.9	1.9	1.5	2.4	1.7	0.5
$[L_w]_N$	JG (40)	7.0	4.0	3.4	4.9	3.7	4.1		4.6	4.1	4.5	0.6
	JS (40)	10.3	9.1	7.9	5.6	6.8	22.6	21.5	8.0	21.8	11.7	4.1
	GS (40)	6.3	6.7	5.6	5.0	5.6	22.7		5.8	22.7	8.4	4.1
	OT JG (50)	6.2	3.7	3.3	5.4	4.6	8.0		4.6	8.0	5.2	1.5
	MT JG (50)	6.9	4.0	3.4	4.5	3.6	3.7		4.5	3.7	4.4	0.5
	ET JG (50)	7.2	4.2	3.7	5.5	3.6	4.2		4.8	4.2	4.7	0.5
$E_u(0^-)$	JG (40)	0.7	0.7	0.7	0.6	0.7	3.1	2.0	0.7	2.5	1.2	0.4
	OT JG (50)	0.4	0.4	0.3	0.4	0.4	8.2	7.0	0.4	7.6	2.4	0.4
	MT JG (50)	0.7	0.7	0.8	0.7	0.8	2.9	2.1	0.8	2.5	1.3	0.4
	ET JG (50)	0.6	0.7	0.6	0.5	0.6	2.5	1.2	0.6	1.9	1.0	0.4
$Q_n(0^-)$	JG (40)	0.9	0.9	0.9	0.9	0.9	2.1	2.4	0.9	2.3	1.3	0.6
	OT JG (50)	0.6	0.5	0.7	0.7	1.2	3.4	4.2	0.7	3.8	1.6	1.3
	MT JG (50)	0.6	0.8	1.0	0.9	1.0	2.4	2.9	0.8	2.6	1.3	0.5
	ET JG (50)	1.2	1.2	0.9	1.0	0.8	1.5	1.6	1.0	1.5	1.2	0.6
All	JG (40)	2.1	1.9	2.4	2.2	2.0	2.4	2.4	2.1	2.5	2.2	1.7

Table 22. A summary of the $\bar{\psi}$, Ψ , and Φ values for the computation of the V5 primary variables.

Comparison		$\bar{\psi}(412)$	$\bar{\psi}(443)$	$\bar{\psi}(490)$	$\bar{\psi}(510)$	$\bar{\psi}(555)$	$\bar{\psi}(665)$	$\bar{\psi}(683)$	Ψ_{1-5}	Ψ_{6-7}	Ψ_{1-7}	$\Phi_{3/5}$
$L_u(0^-)$	JG (40)	0.6	0.6	0.4	0.4	0.5	1.8	1.7	0.5	1.7	0.8	0.1
	JS (40)	6.8	9.1	5.0	4.9	5.3	23.1	21.8	6.2	22.3	10.8	2.4
	GS (40)	6.5	8.9	4.8	4.7	5.2	23.0	21.7	6.0	21.9	10.5	2.4
OT	JG (50)	0.4	0.4	0.4	0.5	0.6	4.0	5.0	0.4	4.5	1.6	0.4
MT	JG (50)	0.5	0.5	0.4	0.4	0.4	2.1	1.9	0.4	2.0	0.9	0.1
ET	JG (50)	0.9	0.8	0.6	0.6	0.5	1.0	0.7	0.7	0.8	0.7	0.1
K_L	JG (40)	0.7	0.7	0.7	0.6	0.6	1.6	2.1	0.7	1.9	1.0	0.3
	OT JG (50)	1.2	1.5	1.5	1.7	1.3	4.9	6.3	1.4	5.6	2.6	0.8
	MT JG (50)	1.0	1.0	1.0	0.9	0.8	2.1	2.7	0.9	2.4	1.3	0.5
	ET JG (50)	0.2	0.2	0.2	0.2	0.2	0.4	0.3	0.2	0.3	0.2	0.0
$E_d(0^-)$	JG (40)	1.2	1.2	1.2	1.1	1.4	2.1	2.8	1.2	2.4	1.6	0.3
	JS (40)	11.3	11.3	11.0	11.0	12.7	32.3	31.3	11.4	32.8	16.9	4.3
	GS (40)	10.7	10.6	10.1	10.2	11.8	32.9	31.6	10.7	33.2	16.5	4.3
	OT JG (50)	2.4	2.5	2.5	2.6	2.7	3.4	3.0	2.5	3.2	2.7	0.3
	MT JG (50)	1.1	1.1	1.0	1.0	1.3	2.1	2.0	1.1	2.0	1.4	0.3
	ET JG (50)	0.8	0.8	1.0	0.8	1.0	1.6	3.8	0.9	2.7	1.4	0.1
K_d	JG (40)	2.8	3.3	4.0	3.0	2.6	0.8	0.8	3.0	0.8	2.4	1.5
	JS (40)	19.1	20.4	25.7	26.6	22.1	14.1	11.9	23.8	13.7	20.9	16.6
	GS (40)	18.9	19.4	23.8	25.3	20.7	13.9	11.6	22.6	13.5	20.1	16.8
	OT JG (50)	8.3	9.5	9.3	5.8	3.5	0.9	0.6	7.3	0.7	5.4	5.9
	MT JG (50)	2.3	3.0	3.3	3.0	2.7	1.0	0.8	2.9	0.9	2.3	1.1
	ET JG (50)	0.2	0.5	2.1	1.3	1.8	0.3	0.8	1.2	0.5	1.0	0.3
$E_d(0^+)$	JG (40)	0.1	0.2	0.1	0.2	0.2	0.2	0.1	0.2	0.2	0.2	0.1
	JS (40)	0.5	0.6	0.7	0.7	0.8	0.7	0.6	0.7	0.6	0.7	0.2
	GS (40)	0.6	0.7	0.6	0.7	0.8	0.7	0.6	0.7	0.6	0.7	0.2
	OT JG (50)	1.5	1.6	1.7	1.8	1.8	1.9	1.9	1.7	1.9	1.8	0.1
	MT JG (50)	0.1	0.3	0.1	0.3	0.2	0.3	0.1	0.2	0.2	0.2	0.1
	ET JG (50)	0.1	0.2	0.2	0.2	0.2	0.2	0.2	0.2	0.2	0.2	0.0
R_{rs}	JG (40)	1.3	1.2	1.1	1.2	1.0	3.1	2.6	1.2	2.8	1.6	0.2
	JS (40)	7.2	6.8	5.6	5.6	6.1	22.9	21.8	6.3	22.1	10.5	2.6
	GS (40)	6.5	6.4	5.1	4.9	5.6	22.5	22.2	5.7	22.0	10.1	2.6
	OT JG (50)	2.1	2.3	2.4	2.4	2.5	8.1	6.7	2.3	7.4	3.8	0.7
	MT JG (50)	1.2	1.1	1.0	1.2	1.0	3.2	2.9	1.1	3.1	1.6	0.3
	ET JG (50)	1.6	1.5	1.3	1.3	1.2	1.9	1.2	1.4	1.5	1.4	0.1
$[L_W]_N$	JG (40)	7.2	4.2	3.5	4.9	3.6	3.8		4.7	3.8	4.5	0.4
	JS (40)	10.3	9.1	7.9	5.6	6.8	22.6	21.5	8.0	21.8	11.7	4.1
	GS (40)	6.1	6.5	5.4	5.1	5.6	22.4		5.7	22.4	8.3	4.2
	OT JG (50)	6.7	4.3	3.9	5.9	4.2	4.8		5.0	4.8	5.0	0.5
	MT JG (50)	7.0	4.0	3.5	4.5	3.4	3.9		4.5	3.9	4.4	0.4
	ET JG (50)	7.6	4.7	3.7	5.4	3.9	3.6		5.0	3.6	4.8	0.3
$E_u(0^-)$	JG (40)	0.7	0.6	0.5	0.5	0.6	2.4	2.1	0.6	2.3	1.1	0.1
	OT JG (50)	0.2	0.2	0.2	0.3	0.4	4.5	4.8	0.3	4.6	1.5	0.2
	MT JG (50)	0.7	0.7	0.6	0.7	0.8	3.1	3.0	0.7	3.1	1.4	0.2
	ET JG (50)	0.6	0.6	0.4	0.4	0.3	0.8	0.5	0.5	0.7	0.5	0.1
$Q_n(0^-)$	JG (40)	0.4	0.4	0.4	0.5	0.5	1.0	1.0	0.4	1.0	0.6	0.2
	OT JG (50)	0.3	0.3	0.3	0.4	0.4	2.4	2.8	0.3	2.6	1.0	0.3
	MT JG (50)	0.4	0.5	0.5	0.6	0.7	1.1	1.2	0.5	1.2	0.7	0.2
	ET JG (50)	0.4	0.3	0.3	0.3	0.3	0.4	0.3	0.3	0.4	0.3	0.0
All	JG (40)	1.7	1.4	1.3	1.4	1.2	1.9	1.7	1.4	1.9	1.5	0.4

$$\begin{aligned}
R_{rs} \quad \Psi_{1-5} &= 1.2(\uparrow 0.2)\%, \quad \Psi_{6-7} = 2.8(\uparrow 0.7)\%, \text{ and} \\
&\quad \Phi_{3/5} = 0.2(\uparrow 0.0)\%; \\
[L_W]_N \quad \Psi_{1-5} &= 4.7(\uparrow 0.1)\%, \quad \Psi_{6-7} = 3.8(\uparrow 0.8)\%, \text{ and} \\
&\quad \Phi_{3/5} = 0.4(\uparrow 0.0)\%; \\
E_u(0^-) \quad \Psi_{1-5} &= 0.6(\uparrow 0.4)\%, \quad \Psi_{6-7} = 2.3(\uparrow 1.8)\%, \text{ and} \\
&\quad \Phi_{3/5} = 0.1(\uparrow 0.1)\%; \\
Q_n(0^-) \quad \Psi_{1-5} &= 0.4(\uparrow 0.2)\%, \quad \Psi_{6-7} = 1.0(\uparrow 0.7)\%, \text{ and} \\
&\quad \Phi_{3/5} = 0.2(\uparrow 0.2)\%; \text{ and} \\
\text{All JG} \quad \Psi_{1-5} &= 1.4(\uparrow 0.5)\%, \quad \Psi_{6-7} = 1.9(\uparrow 0.9)\%, \text{ and} \\
&\quad \Phi_{3/5} = 0.4(\uparrow 0.3)\%.
\end{aligned}$$

Note that in many cases, the increases in uncertainties due to filtering differences is approximately one half (or more) of the uncertainty levels achieved when the processors were the most similar (V3).

As was seen with the V4 and V3 comparisons, the V5 $E_d(0^+)$, R_{rs} , and $[L_W]_N$ uncertainties are very similar to the V3 results, particularly in terms of the percent increases of the V5 results with respect to the V3 results. Again, the $E_d(0^+)$ uncertainties are actually unchanged, and the R_{rs} and $[L_W]_N$ are not strongly altered (from a percent change point of view), because the normalizing variable, $E_d(0^+)$, is unchanged, and the absolute increases in the $L_u(0^-)$ uncertainties are proportionately smaller, particularly for $[L_W]_N$.

The K_L uncertainties are similar to the $L_u(0^-)$ uncertainties, both in magnitude and spectral dependence. The K_d uncertainties are larger than the $E_d(0^-)$ uncertainty values, and have an inverted spectral dependence, i.e., when one is maximal, the other is minimal. With the exception of the K_d results, the band-ratio uncertainties are much less than the spectral uncertainties, and always less than 1.0%.

1.7 DISCUSSION

The most significant changes in the application of the various JRC and GSFC processing options occur from the progression from the V1, V2, and then V3 options. A summary of the evolution in uncertainties for the primary intercomparison variables is shown in Fig. 14 (the dashed and dotted lines set the 2.5% and 1.0% intercomparison objectives, respectively). The figure shows a significant reduction in processing uncertainties as a function of the processing versions (V1 to V3) except for the $E_d(0^+)$ and $[L_W(\lambda)]_N$ variables. The former are small to begin with and stay small, and the latter are large to begin with and stay large. Another exception is some of the band-ratio results. The $L_u(0^-)$, R_{rs} , $[L_W(\lambda)]_N$, and $E_u(0^-)$ band-ratio uncertainties are less than 1.0% for the V1 processing and remain so up through the V3 processing.

Other aspects to note from Fig. 14 are as follows:

1. The most significant improvement is seen in the red wavelengths, except for K_d which has the largest improvement in the blue-green domain;
2. All of the uncertainties are reduced to within 1.0% for the V3 processing except for the $E_d(0^-)$ red wavelengths, all the $[L_W(\lambda)]_N$ values, and the R_{rs} values in the red domain;
3. In terms of overall averages, the 1.0% objective is achieved at all wavelengths except at 412 nm which is slightly above 1.0%; and
4. The largest improvement occurs for the V1 to V2 progression, i.e., making the extrapolation ranges the same has the strongest influence in reducing processing uncertainties.

The uncertainties of the three processors based on the V3 processing of four of the most important primary variables are presented in Fig. 15. The $L_u(0^-)$ results (Fig. 15a) show the lowest uncertainties with the Satlantic processor are for the shallow coastal data, and in all cases, the largest uncertainties are for the red wavelengths—none of the Satlantic uncertainties are below 1.0%, although, the blue-green WiSPER wavelengths are within 2.5%. The average band-ratio uncertainty, $\Phi_{3/5}$, for both Satlantic intercomparisons are, however, below 2.5% (Table 19). The JG uncertainties are always below 2.5%, and mostly below 1.0% except for the blue and red SeaOPS data. The K_d uncertainties (Fig. 15b) show much higher overall uncertainties with respect to the Satlantic processor, particularly for the LoCNESS data set where every wavelength has an uncertainty above 25%. None of the Satlantic uncertainties are below 2.5%, whereas all of the JG uncertainties are, and most of the JG uncertainties are to within 1.0% (the primary exception are the WiSPER data).

The R_{rs} uncertainties (Fig. 15c) are similar to the $L_u(0^-)$ results, especially for the Satlantic intercomparisons. The lowest uncertainties with the Satlantic processor are for the shallow coastal data, and in all cases, the largest uncertainties are for the red wavelengths—none of the Satlantic uncertainties are below 1.0%, although, the blue-green WiSPER wavelengths are within 2.5%. Again, the overall band-ratio results are much improved and are a little larger than 2.5% (Table 19). Almost all of the JG uncertainties are below 2.5% (except for red deep ocean wavelengths), and the majority of the uncertainties are below 1.0% (all of the shallow coastal wavelengths are within 1.0%).

In terms of the identified processing configurations, the JRC and GSFC processors were the most similar for the V3 options, and the minimum uncertainties, both individually and from an overall perspective, were seen with the V3 results.

The V4 processing results show the type of fit used to estimate the slope of the log-transformed data in the extrapolation interval is correlated with the amount of noise in the data, thus, the noisier $E_d(0^-)$ data (from wave focusing effects) are more sensitive to the extrapolation process. This can also be seen in the concentration regime

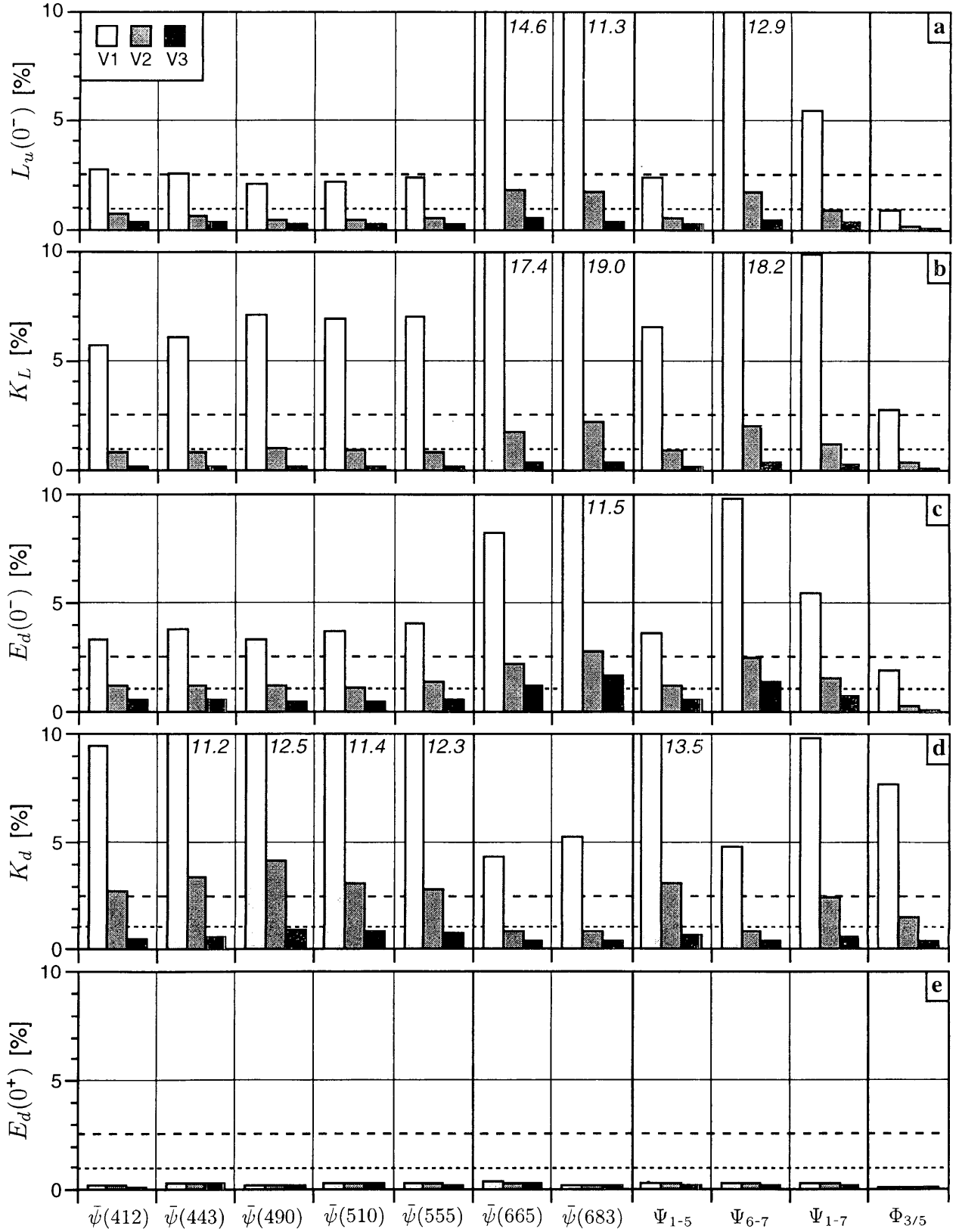


Fig. 14. Average uncertainties in the primary intercomparison variables for the V1 (light gray bars), V2 (dark gray bars), and V3 (black bars) JG processing: a) $L_u(0^-)$, b) K_L , c) $E_d(0^-)$, d) K_d , and e) $E_d(0^+)$.

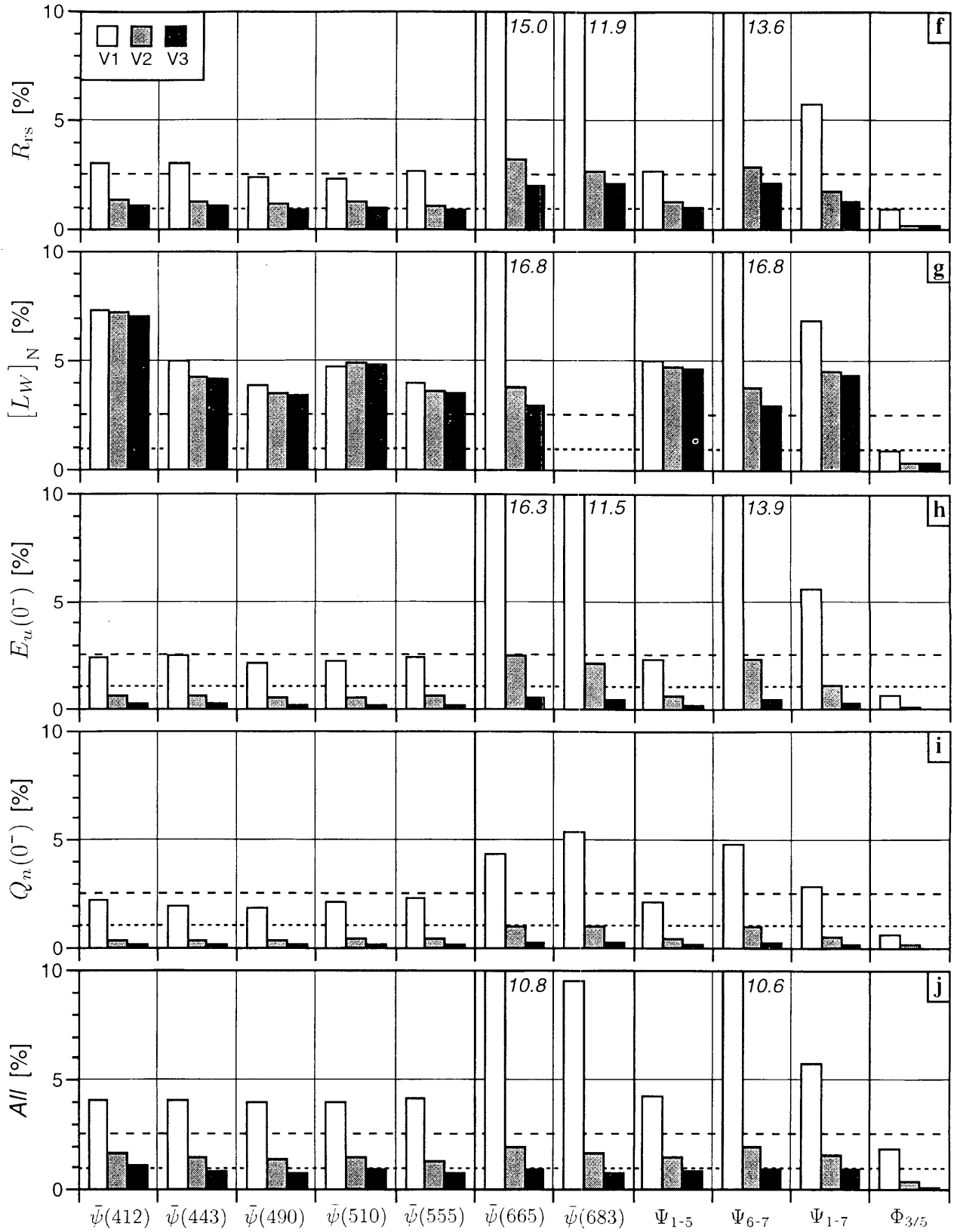


Fig. 14. (cont.) Average uncertainties in the primary intercomparison variables for the V1 (light gray bars), V2 (dark gray bars), and V3 (black bars) JG processing: f) R_{rs} , g) $[L_W(\lambda)]_N$, h) $E_u(0^-)$, i) $Q_n(0^-)$, and j) all the variables.

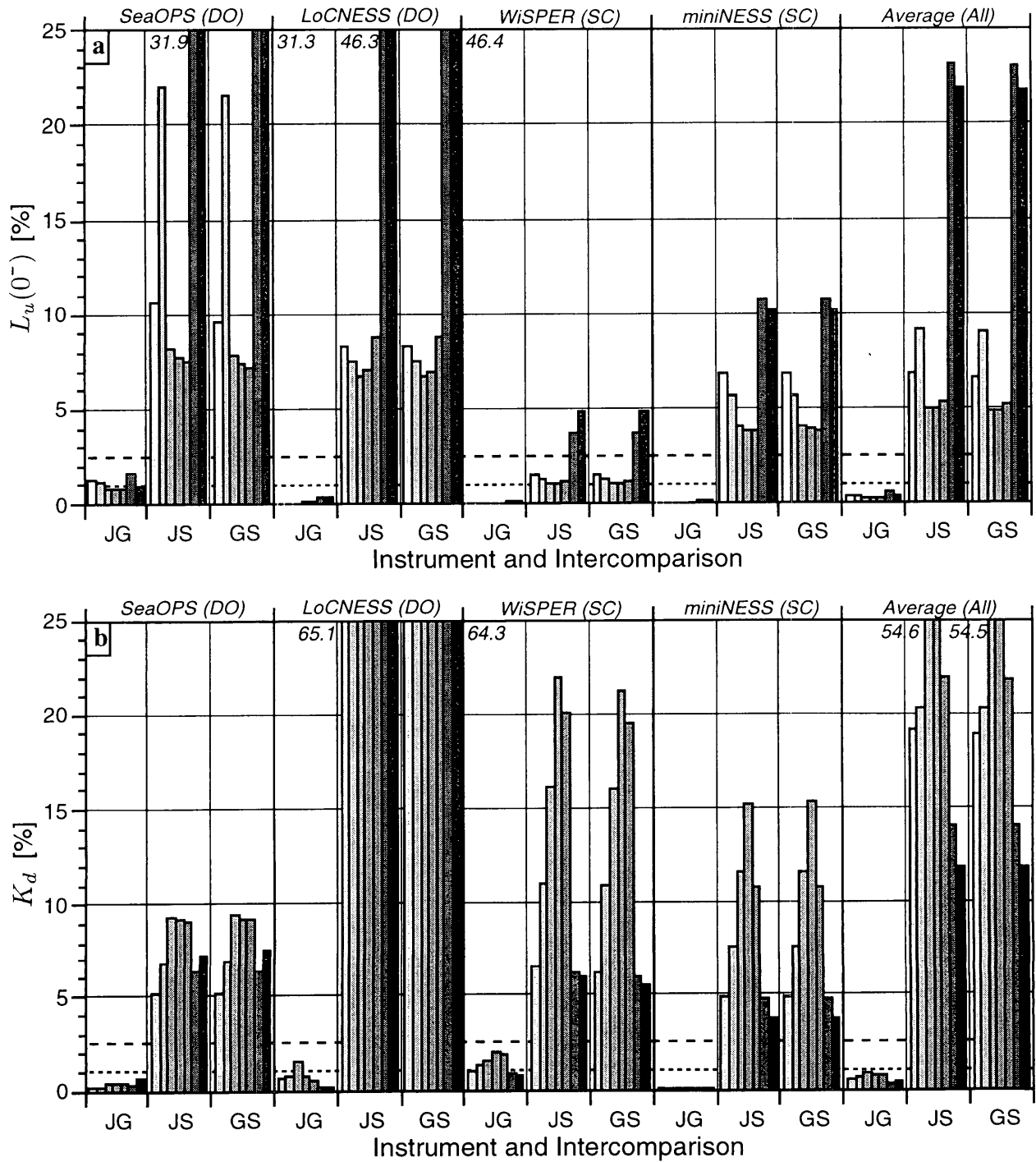


Fig. 15. The average V3 processing uncertainties for the JG, JS, and GS intercomparisons of a) $L_u(0^-)$ and b) K_d . The dashed line sets the 2.5% intercomparison objective and the dotted line the 1.0% objective. Uncertainties above 25% are shown clipped at the 25% level, and the maximum uncertainty achieved is given at the top of the panel to the side of the clipped bars. The individual wavelengths are shown as the sequential bars with varying intensities of gray (going from left to right, blue is light gray and red is dark gray). The instrument (and deployment) codes are given along the top of the subpanels. The overall average of all the data (40 casts) is given in the right-most three intercomparisons.

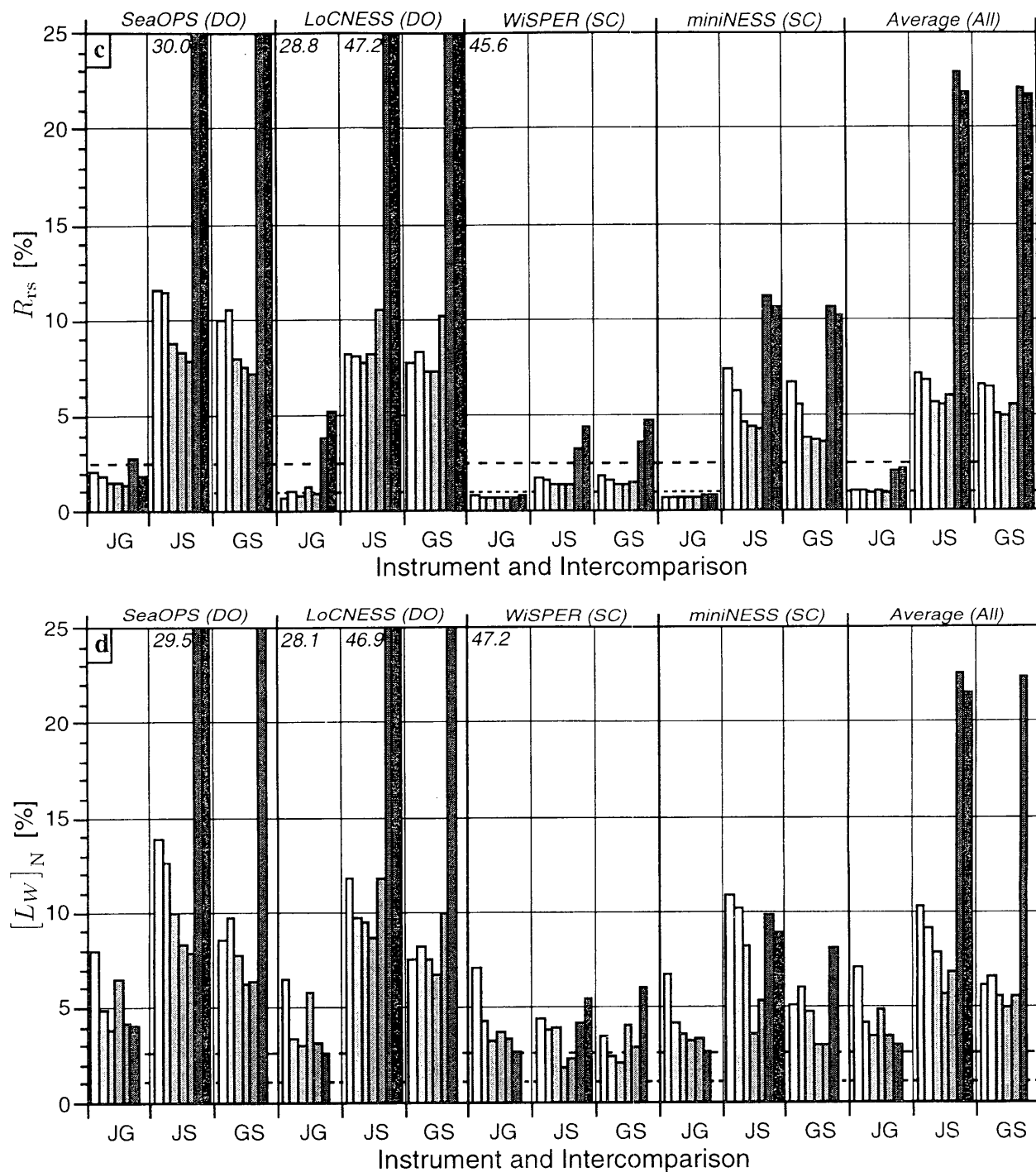


Fig. 15 (cont.). The average V3 processing uncertainties for the JG, JS, and GS intercomparisons of c) R_{rs} and d) $[L_W(\lambda)]_N$. The dashed line sets the 2.5% intercomparison objective and the dotted line the 1.0% objective. Uncertainties above 25% are shown clipped at the 25% level, and the maximum uncertainty achieved is given at the top of the panel to the side of the clipped bars. The individual wavelengths are shown as the sequential bars with varying intensities of gray (going from left to right, blue is light gray and red is dark gray). The instrument (and deployment location) codes are given along the top of the subpanels. The overall average of all the data (40 casts) is given in the right-most three intercomparisons.

data, wherein the $E_d(0^-)$ uncertainties normally increase as the chlorophyll concentration decreases.

The V5 results show that differences in filtering techniques can account for a significant percentage of the uncertainty budgets. In many cases, the increases in uncertainties due to filtering differences was approximately one half (or more) of the uncertainty levels achieved when the processors were the most similar (V3).

The overall sensitivity of the primary variables to chlorophyll *a* concentration depends primarily on the processing options. As the JG processors converged, any dependence on concentration weakened except for the aforementioned larger K_d uncertainties in clear waters (the OT and even the MT regimes).

In most instances, the band-ratio uncertainties are much less than the spectral uncertainties. Furthermore, once the processors were made more similar (i.e., converged), almost all of the band-ratio uncertainties were less than 1.0%. The largest band-ratio uncertainties are associated with the K_d results, which are maximal in the blue-green wavelength domain.

1.8 CONCLUSIONS

From the strict point of view of data processing, the most obvious conclusion from this study is that when separate groups process data in ways they consider appropriate, this can lead to unacceptable uncertainties (greater than 2.5%) in the final products used for calibration and validation activities. Although *in situ* data are probably the best approach for vicarious calibrations, it is important to note the uncertainties associated with the products derived from *in situ* data can be relatively high if different data processors are used.

There are several other aspects of this study that are relevant to calibration and validation activities:

1. The persistently lower $L_u(0^-)$ uncertainties with respect to the $[L_W(\lambda)]_N$ uncertainties suggest the validation of satellite radiometric data and the vicarious calibration of space sensors might be best accomplished with $L_W(\lambda)$ data collected at a time very close to the satellite overpass (which may be used without any normalization).
2. Although a database constructed with processed data from a wide source of contributors will have substantially higher uncertainties than a database constructed with raw data processed with a single processor, the OC2v2 results are not very dependent on the processing options, because band ratios regularly provide reduced uncertainties with respect to individual spectral uncertainties.
3. Data sets for mean $F_0(\lambda)$ used in the computation of $[L_W(\lambda)]_N$ should be chosen in agreement with those used for satellite data processing to remove systematic uncertainties in vicarious calibrations and in product validations.
4. Because of the large uncertainties associated with the selection of extrapolation intervals, techniques should be developed to support the objective selection of the limits for extrapolation intervals, as an attempt to standardize the selection of parameters used for the determination of subsurface values.
5. Data collection from stabilized (i.e., fixed or gimbaled) platforms should be emphasized, and the vertical resolution of the in-water instruments should be maximized (either with a low descent speed or a high data rate).

Chapter 2

The GSFC Data Processing System

STÉPHANE MARITORENA

*UCSB Institute for Computational Earth System Science
Santa Barbara, California*

STANFORD B. HOOKER

*NASA Goddard Space Flight Center
Greenbelt, Maryland*

ABSTRACT

The GSFC data processing system was designed to calculate apparent optical properties from underwater profiles of upward and downward irradiance, as well as upwelling radiance, from a wide variety of open ocean regimes. The full processing involves three steps: a) the calibration of the data, b) the establishment of the extrapolation interval, and c) the derivation of the final data products. In the first step, special files containing dark voltages are used to remove detector offsets and apply a pressure tare to the depth sensor. The second step is done interactively while viewing all the optical and ancillary (sensor tilts, fluorescence, etc.) fields. The final step is usually executed in batch mode using a file of extrapolation limits created in the second step. All of the code is written in the IDL programming environment.

2.1 INTRODUCTION

The GSFC processing software was developed to support the activities of the SeaWiFS Field Team whose main objectives are a) the vicarious calibration of the space-borne sensor, b) the validation of the algorithms used to generate the SeaWiFS data products, and c) the evaluation of the instruments and protocols used for in-water radiometric measurements. Between September 1995 and April 1999, most of the field campaigns conducted by the SeaWiFS Field Team were performed during AMT cruises (Aiken et al. 2000). The codes described here were initially developed to process the AMT radiometric data for SeaWiFS calibration and validation purposes. The processing system was designed to produce, in near-real time, all the quantities (direct or indirect) that can be derived from radiance or irradiance optical profiles conducted in the water column.

During the AMT cruises, the SeaWiFS Field Team deployed a variety of commercial and prototype optical sampling systems built by Satlantic, Inc. These instruments included winch and crane, as well as free-fall deployment platforms, with 2 or 3 optical sensors on each system, and 7 or 13 channels in each sensor. The former are capable of sampling the closest to the surface (especially during the up cast when the instruments are emerging from the mostly undisturbed deep part of the cast), and the sensors are located at very nearly the same depth; the latter cannot

return near-surface measurements for all sensors because of the tilting of the profiler during its initial *righting* period immediately after release, and the sensors at each end of the profiler are usually separated from one another by a vertical distance of approximately 1–2 m. The primary water type sampled during the AMT cruises was clear, deep ocean, Case-1 conditions, although a large range (approximately three decades) in chlorophyll *a* concentrations was sampled after six cruises.

The diversity in sampling equipment, a preponderance of deep casts (as much as 200 m) in clear water (Case-1 conditions), the availability of coincident solar reference data, and the high quality of the in-water data were the governing forces behind the design of the GSFC processor. There was no need for a self-shading correction capability, a bottom correction scheme, or any other data handling requirements usually associated with the coastal (predominantly Case-2) environment, so these were not included as processing options.

For the sake of efficiency, the same core of code was adapted for all instruments and configurations, which also share a variety of utility programs. The processing code is written in IDL and has three main components:

- A calibration module for the conversion of the raw data (counts) to physical units, which also generates an ASCII file containing the calibrated data for each cast plus a vertically binned file;

- A visualization module that plots the various data fields as a function of depth; and
- A module that generates the surface values, that is, it extrapolates the underwater data to the surface and computes quantities relevant to ocean color and marine optics studies.

For the DARR-00 exercise, some minor modifications were made to the codes, so the processing system could handle the formats of the JRC data.

2.2 DATA COLLECTION

The emphasis during SeaWiFS Field Team deployments is to use instruments with absolute calibrations, traceable to the National Institute of Standards and Technology (NIST), and state-of-the art sampling and optical measurement protocols. For each deployment, every effort is made to limit, as much as possible, experimental (ship shadow, superstructure reflections, instrument instability, etc.) and environmental (sea and sky state) perturbations in the measurements. Under most circumstances, the data were collected in Case-1 waters (Morel and Prieur 1977) during stable sky conditions. To ensure a full optical characterization of the euphotic zone, the profiles were usually deployed to a depth that included the 1.0% light level and the deep chlorophyll maximum.

For each cast, two instruments are used: one collects the in-water data in the euphotic zone as a profiling system, and the second one simultaneously records the above-water incident solar irradiance. The free-fall profiling systems are deployed far enough from the ship to avoid ship perturbations, the winch system uses a crane with sufficient reach over the side of the ship to significantly reduce contamination of the in-water data from ship perturbations, and for both systems, the surface reference is installed in a location chosen to minimize the possible influence of the ship's superstructure.

In addition to the *in situ* measurements, dark signals are recorded at least once a day for all light sensors. Dark levels for sensors are generally recorded for 3 min before or after a series of in-water profiles. While on deck, the profiler is kept under a white sheet that is regularly rinsed off to ensure the temperature is more similar to that encountered during sampling. The dark data for the pressure sensor is also used as a pressure tare to ensure accurate depth readings during the in-water cast.

The radiometric measurements always include the a) upwelled radiance, $L_u(z, \lambda)$; b) downward irradiance, $E_d(z, \lambda)$; and c) incident total (direct plus diffuse) solar irradiance, $E_d(0^+, \lambda)$. For most cruises, a third sensor is used to measure the upward irradiance, $E_u(z, \lambda)$. Ancillary in-water measurements are used to ensure the quality of the data or to understand the light measurements in terms of the basic water column properties. These extra measurements include the two-axis tilts of the sensor, fluorescence, plus water temperature and conductivity.

2.3 DATA FORMAT

The SeaWiFS Field Team has developed its own data acquisition software, so the format of the raw data are different from that of the optical equipment manufacturer. The raw data (profile, surface reference, and dark measurements) are stored in ASCII, tab-delimited files composed of a header section followed by a line-by-line data block containing the digitized measurements (Fig. 16). Keywords are used at the start of each header entry which are terminated with the at-sign (@). This architecture follows the design used with SeaBASS, which is the primary *in situ* database for the SeaWiFS Project (Hooker et al. 1994).

The header section includes a number of values associated with the configuration of the data acquisition module, the so-called DATA-100, plus a variety of entries which identify the optical sensors used, experimental information, calibration documentation, etc. Note the use of an explicitly decoded Gregorian date—the month is spelled out—to prevent any time confusion. The data block begins with a header line and is followed by the sequentially numbered data lines. Explicit keywords for the beginning and ending of the data block are not needed, because it starts after the `/end_header@` keyword, and ends with the (platform-dependent) end-of-file (EOF) character.

A data line begins with a sequential record number and a Greenwich Mean Time (GMT) time stamp based on the SDY. The format for the latter is `yyyy ddd hh mm ss.ss`, where `yyyy` is the year, `ddd` is the SDY, `hh` is the (24-hour) hour of the day, `mm` is the minutes of the hour, and `ss.ss` is the seconds of the minute (to within 0.01 s). The digitized sensor counts appear after the time stamp, which are followed by three quality control variables: `Framecount` is a sequential (circular) counter provided by the analog-to-digital converter unit, `Checksum`, and `BadChecksum` parameters.

2.4 PROCESSING STEPS

For most applications, the raw data are considered as the lowest level, the so-called *level-0* data. The basic architecture of the GSFC processor is to convert these data to calibrated values, the so-called *level-1* data. The level-1 data are then used to calculate the final data products. Typically, four raw data files are used to process a cast: the in-water data, the solar reference data, the dark measurements of the in-water profiler, and the dark measurements of the surface reference for that cast or station.

2.4.1 Data Conversion

The first step of the GSFC data processing system is the transformation of the raw data into physical units for all measured parameters. For each parameter, the stability of the dark measurements is controlled (coefficient of variation, i.e., standard deviation divided by the mean, less than 0.01% for the radiometric data) and the mean dark

```

/begin_header<cr>
/sat_prefix=SAT<cr>
/instrument_id=OCP<cr>
/serial_no=0011<cr>
/samples_avg=1<cr>
/start_date=1999MAY10<cr>
/affiliations=GSFC<cr>
/investigators=STANFORD.B.HOOKER<cr>
/experiment=AMT.8<cr>
/data_type=CAST<cr>
/column_headers=Sample_No,GMT_Time_Stamp,Ed1,...,Lu1,...,Eu1,...,Temp_irr,Pressure,Tilt_X,Tilt_Y,
Temp_w,Cond,Fluor,FrameCount,Checksum,BadChecksum<cr>
/sequence_number=10<cr>
/ad_port_1=OCI_ED.050<cr>
/ad_port_2=OCR_LU.036<cr>
/ad_port_3=OCI_EU.048<cr>
/end_header@<cr>
Sample_No GMT_Time_Stamp Ed1...Lu1...Eu1 Temp_irr Pressure Tilt_X Tilt_Y
Temp_w Cond Fluor FrameCount Checksum BadChecksum<cr>
1 1999 130 1414 36.72...44295...50021 50441 40064 32233 32696 32459 37013 56515 33350 54 62 0<cr>
2 1999 130 1414 36.89...41733...50340 50421 40065 32258 32927 32500 37017 56519 33356 55 68 0<cr>
3 1999 130 1414 37.05...42239...50774 50401 40064 32285 33133 32585 37023 56525 33354 56 78 0<cr>
4 1999 130 1414 37.20...40577...51217 50429 40065 32312 33254 32737 37026 56525 33351 57 220 0<cr>
5 1999 130 1414 37.36...43097...51209 50429 40066 32341 33390 32923 37028 56527 33355 58 97 0<cr>
6 1999 130 1414 37.56...46355...50924 50403 40066 32369 33547 33105 37029 56530 33364 59 100 0<cr>
7 1999 130 1414 37.72...48256...50629 50382 40066 32395 33643 33230 37032 56531 33356 60 2 0<cr>
8 1999 130 1414 37.87...48696...50102 50347 40067 32422 33698 33349 37034 56533 33361 61 30 0<cr>
9 1999 130 1414 38.02...50337...49611 50220 40067 32449 33762 33428 37034 56534 33364 62 233 0<cr>
...

```

Fig. 16. An example SeaWiFS Field Team LoCNESS data file. The `/begin_header` keyword denotes the start of the header section which ends with the `/end_header@` keyword. The first line after the latter is a header line for the data block, and all subsequent lines are data lines. Explicit carriage returns, `<cr>`, are shown, because some lines are displayed as wrapped entries (they continue onto a following line), and others as abbreviated entries (they contain the “...” sequences, which indicate omitted values).

value is computed. The calibration files for each of the sensors involved in a particular instrument are read, and the relevant calibration coefficients are extracted.

The raw data are converted to physical units based on a formulation given by the manufacturer of the sensor. For example, the i th sample for a radiometric sensor at center wavelength λ , are converted to physical units according to the following equation:

$$\mathfrak{G}(\lambda, t_i) = C_c(\lambda) I_f(\lambda) [V(\lambda, t_i) - \bar{D}(\lambda)], \quad (4)$$

where $\mathfrak{G}(\lambda, t_i)$ is the calibrated value from the GSFC processor, for which \mathfrak{G} is replaced by $E_d(z)$, $E_u(z)$, $L_u(z)$, or $E_d(0^+)$; $C_c(\lambda)$ is the calibration coefficient; $I_f(\lambda)$ is the immersion factor†; $V(\lambda, t_i)$ is the raw voltage (in digital counts) measured by the instrument at time t_i (which also

sets the depth, z); and $\bar{D}(\lambda)$ is the average dark value (in digital counts) measured during a special *dark cast* with the caps on the radiometer.

Of the ancillary data available with the SeaOPS and LoCNESS profiling systems, the tilt of the profiler with respect to the vertical, φ , is important in ensuring the quality of the optical data:

$$\varphi = \tan^{-1} \sqrt{\tan^2 \varphi_x + \tan^2 \varphi_y} \quad (5)$$

where φ_x and φ_y are the x - and y -axis tilts, respectively, with respect to the vertical coordinate.

The dark calculations and the transformation into physical units are done for the profiler and the reference successively. The two calibrated data sets are then combined into a unique ASCII file. The matchup between the in-water and reference data are based on the time stamp of each sensor record which must agree within a time interval, δt , defined by the user. The default value for δt is set for

† The coefficient accounting for the change in sensor responsivity when the in-air calibration is applied to in-water measurements ($I_f = 1$ for above-water sensors).

an agreement of less than 0.1 s. This value is based on the sampling frequency of the light sensors which is 6 Hz, thus, each sample is generated and acquired within 167 ms, so a δt value of 0.1 s is approximately one-half the sampling interval.

An ASCII file containing the entire (unbinned) profile is then generated. It includes depth, radiometric measurements from the profiler and the reference, and all other available ancillary data. With the exception of the temporal match-up filter between the in-water and surface reference data, no other filtering is applied to the unbinned level-1 data. After the combined (unbinned) file is completed, a vertically binned file is also generated. The vertical bin size, δz , is defined by the user (the default value for δz is 1 m). For this binned file, filtering of the data can be applied based on the two-axis tilts of the instruments during the cast. Threshold values for these angles can be set by the user resulting in the rejection of the data line if the threshold value is exceeded (the default tilt threshold is 10°).

2.4.2 Data Visualization

Although the profiles can be optionally displayed during the calibration step, the GSFC processing system has a specific data visualization module that allows the calibrated data to be plotted for whatever depth range the user specifies. The default graphic window displays six panels: 1) the $L_u(z, \lambda)$ profile, 2) the $E_d(z, \lambda)$ profile, 3) the $E_d(0^+, \lambda)$ data (plotted as a function of time, but correlated with the corresponding in-water measurements), 4) the two-axis tilt profiles, 5) the temperature and conductivity profiles, and, 6) the fluorescence profile. Other combinations of plots are possible and user definable.

The visualization module permits a visual inspection of all the measured parameters. Because the data can be displayed for any desired depth interval, the visualization module is very useful for defining what depth range should be used to perform subsurface extrapolations to the surface, which is required to determine the values of some parameters at null depth, $z = 0^-$. In the GSFC processing system, the selection of these depth ranges by the data analyst is a necessary step before any extrapolations can be achieved—there is no automated method for such a selection.

The selection of the data is based on the examination of the upper part of the profile (0 to 5–30 m depending on the clarity of the water). The data analyst selects the depth range to be used in the extrapolations (defined by an upper and a lower depth threshold) based on the characteristics of the radiometric and ancillary data. The stability of the $E_d(0^+, \lambda)$ data (no clouds or other perturbations), the linearity of the $L_u(z, \lambda)$ data (in semi-log space), two-axis tilts, the characteristics of the mixed-layer depth, and the features of the fluorescence profile are all taken into account in that selection. There is some obvious subjectivity

in this part of the process, because two different analysts might interpret the profiles in different ways, which would probably result in different depth threshold selections.

A completely objective or automated procedure in the depth selection process is almost impossible to achieve and, in any case, is not considered desirable for two reasons: a) in the vicarious calibration process, each *in situ* observation is potentially very precious, because only a few matchups are usually derived from each week of field work (Hooker and McClain 2000), so each cast must be processed to the highest standard possible; and b) automated procedures tend to produce biases or nonstochastic offsets in the data, which would add an unnatural variance to the algorithm validation database.

Generally, the data in the first 1–2 m below the surface cannot be safely used, because of excessive sensor tilts and surface contamination effects (bubbles, foam, wave focusing, etc.). When correctly trimmed, free-fall profilers generally reach their vertical stability after 1–2 m of descent. Aside from the characteristics of the $E_d(0^+, \lambda)$ data, the lower depth to be used in the extrapolation range depends mostly on the clarity of the water. In clear water, the lower limit can be as deep as 20 m, while in more turbid waters, this limit can be very shallow (less than 4 m).

One limitation of the GSFC data processing system is that it was not designed to generate accurate results for wavelengths which are strongly influenced by water absorption (i.e., $\lambda > 570$ nm). When water absorption is strong, the red bands require very specific, and generally very shallow, depth ranges for the extrapolations to be meaningful. Because the SeaWiFS validation effort was initially focused on the first five SeaWiFS bands, no specific processing was developed for the red channels. Furthermore, as good data are generally collected once the L_u sensor is 2–3 m deep in the water column, this may frequently be too deep to allow a relevant extrapolation of the red channels. The null depth values of the red channels are, therefore, acknowledged to be less accurate than the blue and green bands.

2.4.3 In-Water Data Products

Once the depths for the extrapolation intervals have been selected, the values at null depth are calculated for the $L_u(z, \lambda)$, $E_u(z, \lambda)$, and $E_d(z, \lambda)$ data. This step also involves the computation of various other derived parameters above or beneath the sea surface interface. These parameters, and how they are calculated, are described below.

The first step of the in-water computations consists of a series of regression calculations performed, at each wavelength, between the depth (corrected for any difference between the position of the pressure sensor and that of the individual light sensors) and the log-transformed (natural logs) radiometric data. These regressions generate the $L_u(0^-, \lambda)$, $E_d(0^-, \lambda)$, and $E_u(0^-, \lambda)$ values, as well as the diffuse attenuation coefficients for the subsurface region (the extrapolation range): a) downward irradiance,

$K_{E_d}(z_0, \lambda)$; b) upwelled radiance, $K_{L_u}(z_0, \lambda)$; and c) up-ward irradiance, $K_{E_u}(z_0, \lambda)$.

This approach assumes a good linear relationship between the log-transformed (natural log) radiometric data and the depth, such that

$$\ln [\mathfrak{G}(z, \lambda)] = \ln [\mathfrak{G}(z_0, \lambda)] - K_{\mathfrak{G}}(z_0, \lambda) dz, \quad (6)$$

where, again, \mathfrak{G} is either L_u , E_d , or E_u and $dz = z - z_0$.

The slope of the regression provides the diffuse attenuation coefficients, while the exponential of the intercept gives the $L_u(0^-, \lambda)$, $E_d(0^-, \lambda)$, and $E_u(0^-, \lambda)$ values. By default, the processing program uses a classic least-squares method for the regressions, but a robust least absolute deviation method (Press et al. 1992), can also be used. For the latter, possible outliers (noisy points with a larger variance) have a reduced weight in the analysis.

The subsurface Q -factor at null depth derived from the in-water (nadir-viewing) instruments, $Q_n(0^-, \lambda)$, is computed as

$$Q_n(0^-, \lambda) = \frac{E_u(0^-, \lambda)}{L_u(0^-, \lambda)}. \quad (7)$$

2.4.4 Above-Water Data Products

The $L_u(0^-, \lambda)$ value is transmitted through the sea surface to derive the upwelled radiance leaving the sea surface, the so-called *water-leaving* radiance, $L_W(\lambda)$, according to Austin (1974):

$$L_W(\lambda) = \frac{1 - \rho(\lambda, \vartheta)}{n_w^2(\lambda)} L_u(0^-, \lambda), \quad (8)$$

where $\rho(\lambda, \vartheta)$ is the Fresnel surface reflectance at the ϑ nadir angle and $n_w(\lambda)$ is the refractive index of seawater (all the in-water instruments use nadir-viewing radiance sensors for which $\vartheta = 0^\circ$).

Except for a very rough sea surface or a high sun zenith angle, the transmission term in (8), $(1 - \rho(\lambda, \vartheta))n_w^{-2}(\lambda)$, varies only slightly in magnitude and wavelength (Austin 1980). The coefficient 0.54 has been shown (Mobley 1999) to be appropriate under most situations for transmitting the normal radiance from below, to above, the sea surface (Mobley 1999), so (8) is rewritten as:

$$L_W(\lambda) = 0.54 L_u(0^-, \lambda). \quad (9)$$

The only directly measured above-water parameter is the incident solar irradiance. The stability of the light field for the time period matching the chosen extrapolation range is characterized by the coefficient of variation in the corresponding $E_d(0^+, \lambda)$ values. The spectral means of the $E_d(0^+, \lambda)$ values for the extrapolation time period, $\bar{E}_d(0^+, \lambda)$, are used for the normalization of $L_W(\lambda)$ which results in a quantity, the remote-sensing reflectance,

$R_{rs}(\lambda)$, that can be considered independent of the variations of the incident solar radiation:

$$R_{rs}(\lambda) = \frac{L_W(\lambda)}{\bar{E}_d(0^+, \lambda)}. \quad (10)$$

Another commonly used quantity is the normalized water-leaving radiance defined for *in situ* measurements as:

$$[L_W(\lambda)]_N = F_0(\lambda) R_{rs}(\lambda), \quad (11)$$

where F_0 is the mean extraterrestrial solar irradiance corrected for the Earth-sun distance which depends on the SDY, d , i.e., $F_0 = \bar{F}_0(\lambda)\delta_0(d)$. The Earth-sun distance correction is computed as

$$\delta_0(d) = \left[1.0 + 0.0167 \cos \left(\frac{2\pi(d-3)}{365} \right) \right]^2. \quad (12)$$

The $\bar{F}_0(\lambda)$ values used with the GSFC processor are interpolated from the Neckel and Labs (1984) data set, but weighted by the spectral response of the SeaWiFS bands.

2.4.5 Ancillary Data Products

The extrapolation module also calculates several other parameters:

1. The solar zenith angle (computed from the average time measured during the extrapolation interval);
2. The thickness of the mixed-layer depth (as determined by a drop of 0.1°C in four consecutive 1 m depth bins) and the mean mixed-layer depth temperature;
3. The surface PAR values;
4. The depths of the 10%, 1%, and 0.1% surface PAR values;
5. The depth of the chlorophyll maximum (determined from the fluorescence profile); and
6. The surface chlorophyll *a* concentration as estimated by the OC2 and OC4 algorithms.

For any particular cruise or experiment, the surface data and other derived quantities are saved in ASCII files.

2.5 SUMMARY

The GSFC data processing system has been developed to analyze the radiometric and ancillary data collected for calibration and validation purposes by the SeaWiFS Field Team. The processor includes 3 major steps: a) the conversion of the raw data to (calibrated) physical units, b) the visualization of the calibrated data and, c) the calculation of the surface values for ocean color quantities and other ancillary data. The codes can process data collected by Satlantic OCR-200, OCI-200, OCR-1000, and OCI-1000 sensors. Several options can be selected throughout the

processing procedure: tilt filtering threshold, data visualization scaling, vertical bin size, extrapolation interval depth range, and the type of regression used for the extrapolation. The final step of the processing generates the following products: $L_u(0^-, \lambda)$, $E_d(0^-, \lambda)$, $E_u(0^-, \lambda)$, $E_d(0^+, \lambda)$, $K_d(\lambda)$, $K_L(\lambda)$, $K_u(\lambda)$, $R_{rs}(\lambda)$, $[L_W(\lambda)]_N$, and $Q_n(0^-, \lambda)$. Several ancillary data (temperature, conductivity, fluorescence, etc.) are used to estimate PAR, MLD, DCM, sun zenith angle, etc. The processor is written in the IDL programming environment.

ACKNOWLEDGMENTS

All SeaWiFS Field Team data are acquired and recorded using software developed by J. Brown (University of Miami) and the SeaWiFS Project. The testing and implementation of the GSFC data processor and acquisition systems were accomplished during AMT cruises. The stewardship of the AMT Program and the collection of the optical data have been a high priority for J. Aiken (Plymouth Marine Laboratory); his diligence and commitment has been essential to the high quality and quantity of the optical data collected.

Chapter 3

The JRC Data Processing System

DAVIDE D'ALIMONTE

GIUSEPPE ZIBORDI

JEAN-FRANÇOIS BERTHON

*Marine Environment Unit, Space Applications Institute
Joint Research Centre of the European Commission
Ispra, Italy*

ABSTRACT

The JRC Data Processor was developed for the analysis of field data collected in coastal and marine regions in support of ocean color calibration and validation activities. The code specifically supports the calibration, formatting, visualization, and processing of in-water optical profiles of $L_u(z, \lambda)$, $E_d(z, \lambda)$, and $E_u(z, \lambda)$ collected with the Satlantic seven-channel OCR-200 and OCI-200 sensor series. The user can define a variety of options which permit the selection of the extrapolation interval for the computation of the near-surface values, and the removal of outliers through statistical filtering. Relevant features include the possibility to minimize measurement perturbations such as instrument self shading, bottom effects, and superstructure shading (although the latter is restricted to measurements performed at the *Acqua Alta* Oceanographic Tower site in the northern Adriatic Sea). Each step of the processing is supported by the graphic presentation of intermediate results. Output products are the subsurface values $L_u(0^-, \lambda)$, $E_d(0^-, \lambda)$, and $E_u(0^-, \lambda)$; the diffuse attenuation coefficients $K_d(\lambda)$, $K_L(\lambda)$, and $K_u(\lambda)$; plus the derived products $R(0^-, \lambda)$, $R_{rs}(\lambda)$, $[L_W(\lambda)]_N$, and $Q_n(0^-, \lambda)$.

3.1 INTRODUCTION

The JRC Data Processor is a comprehensive software package for field data analysis. It was developed within the Coastal Atmosphere and Sea Time-Series (CoASTS) project (Zibordi et al. 2001) to support ocean color calibration and validation activities. The processor ensures handling of marine and atmospheric measurements and, specifically, the analysis of in-water optical profile data.

An important feature of the processor is the capability for removing measurement perturbations, like instrument self shading, bottom effects, and tower shading [the latter correction is specific to data collected at the *Acqua Alta* Oceanographic Tower site (Zibordi et al. 2001)]. This makes the code well suited for the processing of oceanic, as well as coastal, data. The processor is composed of a data calibration and formatting program plus a data filtering and processing program, and uses a graphical user interface (GUI) to interactively define the processing settings.

The data calibration and formatting program has five main functions:

1. Ingestion of ASCII raw (i.e., level-0) data in different formats;
2. Calibration of the data, including dark correction for light sensors and pressure tare for depth sensors;

3. Screening of data as a function of a user-selectable tilt threshold;
4. Visualization of data as a function of depth; and
5. Creation of the level-1 (output) data files.

The DARR-00 exercise also required the implementation of specific routines for ingesting the GSFC ASCII raw data.

The data filtering and processing program has six main functions:

- i) Definition of extrapolation intervals for the computation of subsurface values and bottom reflectances;
- ii) Selection of normalization methods for in-water data with respect to above-water reference measurements;
- iii) Filtering of outlier data in the subsurface extrapolation interval, and removal of data below the noise threshold (defined as the radiance or irradiance given by 5 digital counts);
- iv) Correction for perturbation effects;
- v) Visualization of data as a function of depth together with extrapolated (surface and bottom) values; and
- vi) Creation of the level-2 (output) binned data and products.

All of the output files are in ASCII format, and can be quickly and easily used by the user.

3.2 DATA REQUIREMENTS

The JRC optical processor was primarily designed to support the analysis of data collected by Satlantic optical systems composed of multiple seven-channel OCR-200 and OCI-200 sensors to measure $L_u(z, \lambda)$, $E_d(z, \lambda)$, $E_u(z, \lambda)$, and $E_d(0^+, \lambda)$. The analysis of in-water profile data requires the following ancillary data:

- Dark data for the calibration process (including setting the pressure tare);
- Seawater absorption, $a(\lambda)$;
- Seawater single scattering albedo, $\omega(\lambda)$; and
- The diffuse-to-direct solar irradiance ratio, $r(\lambda)$.

The latter is obtained from

$$r(\lambda) = \frac{E_i(0^+, \lambda)}{E_d(0^+, \lambda) - E_i(0^+, \lambda)}, \quad (13)$$

where $E_i(0^+, \lambda)$ is the diffuse solar irradiance (for the correction of perturbation effects).

3.3 DATA PROCESSING STEPS

Data processing includes two steps: i) data calibration and formatting to convert the raw data from counts (level-0 data) to physical units (level-1 data); and ii) data filtering and processing to remove outliers and create the level-2 data products. During each step, for each optical profile, the user can define processing parameters, which are stored in an *information file* and can be reloaded for subsequent automated reprocessing.

3.3.1 Calibration and Formatting

Data calibration and formatting involves five steps: ingestion, calibration, screening, display, and output.

3.3.1.1 Data Ingestion

Input data for the calibration and formatting program include several ASCII files: i) the in-water radiance and irradiance files; ii) the reference above-water irradiance file; iii) the calibration files for the in-water and above-water devices (i.e., radiometers, pressure sensors, and tilt sensors); and iv) the dark data for the in-water and above-water radiometers. Specific ingestion routines ensure ingestion of profile and reference data in different formats.

3.3.1.2 Data Calibration

The absolute calibration of the primary radiometric quantities, $L_u(z, \lambda)$, $E_d(z, \lambda)$, $E_u(z, \lambda)$, and $E_d(0^+, \lambda)$, are obtained from:

$$\mathfrak{J}(\lambda, t_i) = C_c(\lambda) I_f(\lambda) [V(\lambda, t_i) - \bar{D}(\lambda)], \quad (14)$$

where $\mathfrak{J}(\lambda, t_i)$ is the calibrated value from the JRC processor, for which \mathfrak{J} is replaced by $E_d(z)$, $E_u(z)$, $L_u(z)$, or $E_d(0^+)$; $C_c(\lambda)$ is the calibration coefficient; $I_f(\lambda)$ is the immersion factor; $V(\lambda, t_i)$ is the raw voltage (in digital counts) measured by the instrument at time t_i (which also sets the depth, z); and $\bar{D}(\lambda)$ is the average dark value (in digital counts) measured at least once a day during a special *dark cast* with the system in air and caps on the radiometer.

3.3.1.3 Data Screening

An optional capability for screening the data as a function of the instrument tilt (i.e., removing data above a tilt threshold value which can be set by the user) is computed from $\varphi = \tan^{-1} \sqrt{\tan^2 \varphi_x + \tan^2 \varphi_y}$, where φ_x and φ_y are the two-axis tilts with respect to the vertical coordinate. The threshold for data rejection, φ_0 , is user-selectable and has a default value of $\varphi_0 = 5^\circ$.

3.3.1.4 Data Display

Calibrated profiles, i.e., $L_u(z, \lambda)$, $E_d(z, \lambda)$, and $E_u(z, \lambda)$, can be displayed, together with tilts as a function of depth in logarithmic scale. $E_d(0^+, \lambda)$ is displayed as a function of the depth of the coincident in-water profile data. This easily ensures the identification of artifacts, which may affect the optical profile data.

3.3.1.5 Output Data Format

The output data are stored using the Coastal Region Long-Term Measurements for Colour Remote Sensing Development and Validation (COLORS) data format† which is composed of four blocks of information:

- The *header block* contains geographic and temporal information, in addition to codes identifying the methods used during data collection;
- The *calibration block* contains information on the measurement systems, the sensors heads, and the calibration coefficients for each sensor;
- The *data block description* provides the list of quantities in the data block and the units assigned to each of them; and
- The *data block* contains the in-water data as a function of depth together with the related above-water reference data, tilts, and time stamps.

An example of the COLORS data format, for optical profile data, is given in Fig. 17.

† The COLORS data can be reviewed on the World Wide Web at <http://marine.ie/datacentre/projects/colors/>.

```

/begin_header<cr>
/site_code=P<cr>
/method_code=04A005,04A004,04A003,04A003<cr>
/parameters=subsurface_upwelling_spectral_irradiance,subsurface_downwelling_spectral_irradiance,
surface_downwelling_spectral_irradiance,subsurface_upwelling_irradiance<cr>
/latitude[deg]=45.3139<cr>
/longitude[deg]=12.5083<cr>
/mean_sounding[m]=17.00<cr>
/sampling_date=12111999<cr>
/start_time[GMT]=09:11:15<cr>
/end_time[GMT]=09:11:36<cr>
/station_ref=P630302P<cr>
/calibration_block<cr>
instrument_id=SATLANTIC_OCP#016,SATLANTIC_MVD#054<cr>
calibration_date=01071999<cr>
Lu_sensor_id=067<cr>
Ed_sensor_id=097<cr>
Es_sensor_id=129<cr>
Eu_sensor_id=109<cr>
Lu_depth_off=-0.098<cr>
Ed_depth_off=-0.258<cr>
Es_depth_off=0.0<cr>
Eu_depth_off=0.763<cr>
!Variable Lambda      Coe0      Coe1      Coe2      Coe3      Coe4<cr>
Depth      -999.9    32588.7    6.4830e-003    0.00      0      0<cr>
LU412      412.5     32775.6    1.7770e-006    1.75      0      0<cr>
...
ED412      412.3     32783.0    6.1497e-005    1.52      0      0<cr>
...
ES412      412.1     32779.1    9.6073e-005    1.00      0      0<cr>
...
EU412      412.5     32770.5    4.1442e-006    1.52      0      0<cr>
...
EU685      683.2     32774.0    2.2731e-006    1.38      0      0<cr>
/datablock_description<cr>
/fields=seq_number,sampling_depth[m],sampling_time[hh:mm:ss:ssss],SUR_ATX[deg],...<cr>
/n_fields=35<cr>
/n_records=94<cr>
/default=-9,-9.99,-99:-99:-99:-9999,-9.99,-9.99,-9.99,-9.99,-9.99999999,...,-9.99999999<cr>
/delimiter=comma<cr>
!Related CoASTS files=p63d3a.ocp,p63s3b.ocp,p63d3a.mvd,p63s3b.mvd<cr>
!Calibration files=ocpd.cal,mvdd.cal<cr>
/end_header<cr>
/begin_data<cr>
1,0.21,09:11:19:4060,0.00,0.00, 4.06,-1.30,0.00685499,...,0.00735924<cr>
2,0.86,09:11:20:5680,0.00,0.00, 4.64, 0.58,0.00557378,...,0.00507873<cr>
3,0.99,09:11:20:7380,0.00,0.00, 3.65, 2.18,0.00542140,...,0.00458938<cr>
4,1.08,09:11:20:8980,0.00,0.00, 2.28, 2.65,0.00511975,...,0.00405297<cr>
5,1.23,09:11:21:0680,0.00,0.00, 1.02, 2.08,0.00472793,...,0.00356675<cr>
6,1.37,09:11:21:2390,0.00,0.00,-0.32, 1.11,0.00436408,...,0.00312759<cr>
...
/end_data<cr>

```

Fig. 17. An example COLORS data file. The header section begins with the `/begin_header` keyword and ends with `/end_header`. Similarly, the data block begins with the `/begin_data` keyword and ends with `/end_data`.

3.3.2 Filtering and Processing

The primary purpose of the filtering options with the processor are to deal with data outliers and to correct for *in situ* perturbations to the light field.

3.3.2.1 Extrapolation Intervals

The appropriate selection of the extrapolation interval, is the key element in extracting accurate subsurface data from in-water profiles. In coastal water, where optical stratifications may occur in the first few meters of the water column, an inappropriate selection of the extrapolation interval can induce large uncertainties in the final products. Although default values can be defined, the identification of an *optimum* extrapolation range satisfying the requirement for a linear decay of $\ln [\mathfrak{J}(z, \lambda)]$ is made by the operator on a cast-by-cast basis.

In addition to the subsurface extrapolation interval, the selection of a bottom extrapolation interval is required to estimate bottom reflectance from profile data, when the correction for bottom effects is needed.

3.3.2.2 Normalization of In-Water Data

In-water radiometric quantities can be normalized with respect to $E_d(0^+, \lambda, t)$, with t explicitly expressing the dependence with time, according to

$$\mathfrak{J}(z, \lambda, t_0) = \mathfrak{J}(z, \lambda, t) \frac{E_d(0^+, \lambda, t_0)}{E_d(0^+, \lambda, t)}, \quad (15)$$

where $\mathfrak{J}(z, \lambda, t_0)$ identifies the radiometric quantity as it would have been taken at all depths z at the same time t_0 ; $E_d(0^+, \lambda, t)$ is the solar irradiance taken at the same time, t , as the in-water data; and $E_d(0^+, \lambda, t_0)$ is the above water irradiance at time t_0 (where t_0 is generally chosen to coincide with the start of the cast).

Alternatively, $E_d(0^+, \lambda, t_0)$ can be defined as the median for data records in the extrapolation interval. The normalization process can be skipped if data are not available or are strongly affected by noise (e.g., ship motion). When $E_d(0^+, \lambda, t)$ is affected by harmonic noise (induced by the regular motion of the ship), $E_d(0^+, \lambda, t)$ can be linearly fitted as a function of t , and the fitted values can be used in the normalization of the profile data. For simplicity, the variable t is omitted in the following discussion.

3.3.2.3 Filtering

Data extrapolation in the subsurface layer is carried out using a least-squares linear fit. This technique may produce biased results in the presence of outliers, e.g., produced by wave focusing effects. This bias may become larger as the number of points per unit depth decreases in the optical profile. Because of this, two complementary filters have been implemented. The first ensures removal of

points distant by more than $n\sigma$ from the linear regression line obtained with all profile data, where n is a user-defined multiplier, and σ is the standard deviation in the distance of the data points from the regression line.

The second filter computes successive regressions by adding depth increments to a defined *basic* extrapolation interval, and compares the slope of the resulting regression line with the slope of the regression line obtained for the *basic* extrapolation interval. The latter filter may remove all points below a certain depth within the chosen fitting interval, if for a given depth increment, the slope of the fitting line changes by more than a selected percent difference with respect to the initial value.

Regression trials, to verify filtering in the extrapolation interval, are possible choosing a specific in-water quantity (i.e., L_u or E_d) and a specific wavelength, e.g., $E_d(665)$. The use of E_d also allows a direct comparison of the in-water extrapolated value $E_d(0^+, \lambda)$ with the solar reference value, $E_d(0^+, \lambda)$, to immediately identify *difficult* situations (i.e., those showing very different $E_d(0^-, \lambda)$ and $E_d(0^+, \lambda)$ values). The use of a channel in the red part of the spectrum, where seawater is characterized by high absorption and light levels exhibit a rapid drop to noise levels as a function of depth, helps in excluding noisy data from the fitting interval chosen for processing.

All records (i.e., all quantities and channels) taken at the same time as data flagged by the filter are removed. The assumption made here is that all data collected at the same time are affected by the same perturbations. The input parameters are user selectable, so the filtering techniques can be used while retaining complete control in the removal of the outliers.

3.3.2.4 Removing *In Situ* Perturbations

Instrument self-shading, bottom reflection, and tower-shading effects can be removed through single or multiple selections. The correction factors are calculated assuming all the perturbations are independent from each other.

Self-shading correction factors are computed using the scheme proposed by Gordon and Ding (1992) and the parameterizations suggested by Zibordi and Ferrari (1995) and Mueller and Austin (1995). The computations are carried out using the solar zenith angle, θ , as well as $a(\lambda)$, $r(\lambda)$, and the ratio between the instrument diameter and the sensor entrance optics diameter.

The correction factors for bottom reflection effects are estimated with a simple analytical model (Zibordi et al. 2001) adapted from Maritorena et al. (1994). Computations are performed using: a) the bottom reflectance, $\rho(\lambda) = E_u(z_b, \lambda)/E_d(z_b, \lambda)$, obtained from each profile at a depth z_b near the bottom; and b) the mean diffuse attenuation coefficient $\bar{K}_d(\lambda)$ for the depth interval $z_0 - z_b$, where z_0 is the subsurface depth identifying the uppermost value of the extrapolation interval.

Tower-shading correction factors are obtained from look-up tables (Doyle and Zibordi 1998) derived from

Monte Carlo simulations of the radiance and irradiance fields at the AAOT site for the specific point where the WISPER measurements are made (Zibordi et al. 1999). For each center wavelength, λ , the correction factors are indexed by discrete values of θ , $a(\lambda)$, $\omega(\lambda)$, and $r(\lambda)$.

3.3.2.5 Fitting

Subsurface $\mathcal{J}(0^-, \lambda)$ optical values (L_u , E_u , and E_d), are obtained from the exponent of the intercept given by the least-squares linear regression of $\ln[\mathcal{J}(z, \lambda)]$ (computed from data not removed by filters) versus z within the extrapolation interval identified by $z_0 < z < z_1$. Generally for the CoASTS profiles, $0.3 < z_0 < 1$ m and $2.5 < z_1 < 4.5$ m. The negative value of the slope of the regression fit is the diffuse attenuation coefficient $K_{\mathcal{J}}(\lambda)$.

An option, called “multicast processing” enables the processing of data from a set of profiles, collected within a user-defined time interval (generally spanning a few minutes), as a single optical profile. This procedure increases the statistical significance of regression analysis applied to subsurface data characterized by a low depth resolution (which is a usual characteristic of free-fall instruments) and affected by large perturbations (e.g., caused by surface effects).

3.3.2.6 Data Visualization

For each specific quantity and for all wavelengths, it is possible to display the optical data and accompanying tilts as a function of depth. Regression lines for the near-surface extrapolation layer and the bottom layer are also shown. In addition, arrows at 0 depth indicate the subsurface extrapolated value, the subsurface extrapolated value corrected for perturbation effects, and in the specific case of $E_d(0^-, \lambda)$, also the corresponding $E_d(0^+, \lambda)$.

3.3.2.7 In-Water Data Products

The major in-water products obtained from optical profiles are $L_u(0^-, \lambda)$, $E_d(0^-, \lambda)$, $E_u(0^-, \lambda)$, and $K_d(\lambda)$ computed from regressions in the extrapolation interval. Additional products are the subsurface Q -factor at nadir view, which is computed as $Q_n(0^-, \lambda) = E_u(0^-, \lambda)/L_u(0^-, \lambda)$, and the subsurface irradiance reflectance, $R(0^-, \lambda)$, which is given by

$$R(0^-, \lambda) = \frac{E_u(0^-, \lambda)}{E_d(0^-, \lambda)}. \quad (16)$$

3.3.2.8 Above-Water Data Products

The above-water products are a) the total solar irradiance measured at the start of the extrapolation range, $E_d(0^+, \lambda, t_0)$; b) the remote sensing reflectance, $R_{rs}(\lambda) = L_W(\lambda)/E_d(0^+, \lambda, t_0)$; and c) the normalized water-leaving radiance, $[L_W(\lambda)]_N = F_0(\lambda) R_{rs}(\lambda)$. For the latter, the mean extraterrestrial solar irradiance, F_0 , is corrected for

the Earth–sun distance which depends on the SDY, d , i.e., $F_0 = \bar{F}_0(\lambda)\delta_0(d)$ using

$$\delta_0(d) = \left[1.0 + 0.0167 \cos \left(\frac{6.283(d-3)}{365} \right) \right]^2. \quad (17)$$

The $\bar{F}_0(\lambda)$ values used with the JRC processor are interpolated from Neckel and Labs (1984) to the center wavelengths of the sensors involved.

Alternatively, if $E_d(0^+, \lambda)$ is not directly measured (with a separate sensor), $R_{rs}(\lambda)$ and $[L_W(\lambda)]_N$ are derived using $E_d(0^+, \lambda)$ values computed from $E_d(0^-, \lambda)$ according to

$$E_d(0^+, \lambda) = \frac{E_d(0^-, \lambda) - 0.49 E_u(0^-, \lambda)}{1 - \rho_s(\lambda)}, \quad (18)$$

where $\rho_s(\lambda)$ is the sea surface reflectance for downward irradiance. The latter is given by

$$\rho_s(\lambda) = \frac{\rho(\theta) + 0.66 r(\lambda)}{1 + r(\lambda)}, \quad (19)$$

where $\rho(\theta)$ is the Fresnel reflectance of the sea surface, and the constant 0.66 is the sea surface albedo under diffuse illumination. For very clear-sky conditions, $r(\lambda) \ll 1$ and $\rho_s(\lambda) \rightarrow \rho(\theta)$.

3.4 SUMMARY

The JRC Data Processing System has been designed to perform absolute calibration, formatting, visualization, and processing of in-water optical profile data. Data handling is specifically optimized for OCI-200 and OCR-200 Atlantic seven-channel radiometers. The processor, developed to ensure the analysis of both coastal and open ocean data, has options for the following:

1. The selection of the extrapolation interval chosen to satisfy linear decay of the logarithm of profile data at all wavelengths;
2. The normalization of the in-water profile data with respect to the above-water downward irradiance; and
3. The capability of combining multiple casts to increase the statistical significance of single profile data collected with low vertical resolution.

Additional relevant processing options are:

4. The filtering of outliers through statistical analysis; and
5. The removal of measurement perturbations for self-shading, bottom effects, and superstructure shading (only for data collected at the AAOT site in the northern Adriatic Sea) making use of atmospheric parameters as the ratio between diffuse and direct atmospheric irradiance, and marine parameters as seawater absorption and single scattering albedo.

ACKNOWLEDGMENTS

This activity has been supported by the European Commission through the MAST-III COLORS Project (contract MAS3-CT97-0087).

Chapter 4

The ProSoft Optical Data Processor

JURI SILDAM
SCOTT MCLEAN
Satlantic, Inc.
Halifax, Canada

ABSTRACT

The ProSoft data processor was developed for the analysis of optical data collected with instruments manufactured by Satlantic, Inc., including profiling and fixed-depth (buoy) systems. The data processing steps are organized into different levels which follow, as much as possible, the procedures given in the *Ocean Optics Protocols for SeaWiFS Validation, Revision 1* (Mueller and Austin 1995). The processing involves three steps wherein the level-0 raw data (usually binary) are converted to calibrated values (engineering units) using one of several options for dark current correction, the level-1 data are averaged and corrected for acquisition and performance problems (if any), and the level-2 data are used to compute the final data products, e.g., R_{rs} , $[L_W(\lambda)]_N$, PAR, etc. Processing can be done manually (and interactively) by the user, guided by the ProSoft processing steps, or in a fully automated batch mode. A notable difference between ProSoft and other data processors is the diffuse attenuation coefficient can be estimated using a traditional estimation of the slope of the optical variables within a user-defined extrapolation interval or using a new methodology based on multiresolution wavelet analysis.

4.1 INTRODUCTION

ProSoft is a data analysis package for processing optical data collected from oceanographic profiling systems. The primary goal in the development of ProSoft was to create a package capable of processing optical profile data in an automated manner to remove the subjective aspects of data processing, thereby ensuring any two investigators would get the same derived values from the same data set. ProSoft allows users to read, process, visualize, and produce numerous data products from raw data sets collected from their instrumentation.

The ProSoft program was developed over the past ten years by Dalhousie University (by the authors) and distributed to users as source code[†]. ProSoft currently consists of about 220 program modules and 60 support files linked by a GUI. The current version of ProSoft is 6.3d, and runs under MATLAB[‡] version 6.

This chapter is intended to give an overview of the main data processing steps carried out by ProSoft. It is assumed that the radiometric data have been collected with

an optical instrument whose raw data format is in compliance with the Satlantic Instrument Files Standard (SIFS) format[§] or with GSFC level-0 ASCII files. It is also assumed that the radiometric data have been collected as a vertical profile of the water column with coincident reference measurements from an instrument floating at the ocean surface.

The ProSoft data processing steps are organized into different levels which follow, as much as possible, the procedures given in the *Ocean Optics Protocols for SeaWiFS Validation, Revision 1* (Mueller and Austin 1995). The processing blocks which exactly follow the Mueller and Austin (1995) recommendations are explicitly indicated. During processing, detailed notes, equations, and references for the various modules can be obtained by clicking on the Help button in any of the ProSoft (internal) menus.

4.2 DATA PROCESSING

ProSoft processing is segmented into four different levels: a) level-0 data are raw (usually binary) files from an instrument; b) level-1 data are calibrated (engineering units), but unaveraged instrument data; c) level-2 data

[†] The ProSoft program is currently supported by Satlantic, Inc. and is freely available at the following Internet address: ftp.satlantic.com/pub/sensors/software/prosoft.

[‡] MATLAB is a registered trademark of MathWorks, Inc. (Natick, Massachusetts).

[§] Satlantic Instrument Files Standard, Satlantic's Data Format Standard for Calibration and Telemetry Definition Files, 2000, Version 6.

are averaged and corrected instrument data; and d) level-3 data are the final products, i.e., R_{rs} , $[L_W(\lambda)]_N$, PAR, etc. Processing can be done manually (and interactively) by the user, guided by the ProSoft processing steps, or in a fully automated batch mode. User preferences, settings, and instrument configuration parameters are set in a configuration file (`prosoft.cfg`). ProSoft will output data files in three formats: tab-delimited ASCII text in ProSoft format, SeaBASS text format, or MATLAB binary format. The latter can be reingested by ProSoft much faster than the ASCII formats.

4.2.1 Level-1 Data Processing

Level-1 data processing begins with reading the raw level-0 data produced by SatView (the Satlantic data acquisition program) compliant with SIFS 2000 (or GSFC level-0 data). These files typically contain detailed header information on the cast, in addition to the binary telemetry from one or more instrument systems. An instrument system usually consists of a profiling optical system (profiler) and a surface reference at some fixed depth or location above the sea surface (reference). ProSoft scans the data files and determines the number and type of instruments, prompting the user for the appropriate calibration files (or automatically loading the most recent file for that system in the current directory if the program is being used in an automated mode). The calibration information for each channel is then applied to the raw data to convert it to engineering units.

4.2.1.1 Optical Data Calibration

Standard optical sensor data formats are processed differently, based on the capabilities of the various types of acquisition systems. These are referred to as OPTIC1 (high resolution gain switching 24-bit systems), OPTIC2 (standard 12-, 16-, 24-, or 32-bit systems), and OPTIC3 (hyper-spectral systems with adaptive integration). Application of the calibration data to all optical and ancillary sensors is carried out in accordance with the procedures detailed in SIFS.

Optical data are converted into engineering units using:

$$\mathfrak{S}(\lambda, t_i) = C_c(\lambda) I_f(\lambda) [V(\lambda, t_i) - D(\lambda)], \quad (20)$$

where $\mathfrak{S}(\lambda, t_i)$ is the calibrated value from the Satlantic processor, for which \mathfrak{S} is replaced by $E_d(z)$, $E_u(z)$, $L_u(z)$, or $E_d(0^+)$; $C_c(\lambda)$ is the calibration coefficient; $I_f(\lambda)$ is the immersion factor; $V(\lambda, t_i)$ is the raw voltage (in digital counts) measured by the instrument at time t_i (which also sets the depth, z); and $D(\lambda)$ is the dark value (in digital counts). Within the ProSoft nomenclature, the dark value in (20) is referred to as the dark *current*, and can be obtained from a calibration file or from one of the dark current correction (DCC) methods described below.

ProSoft currently implements DCC options other than calibration dark or shutter dark (which are explained below) only in the OPTIC1 (high resolution 24-bit systems) fitting mode.† The dark current can change under varying thermal conditions on the high resolution systems and has to be adjusted accordingly.

In the OPTIC1 fitting mode, DCC other than that based on the calibration file (except HyperTSRB) can only be used for measurement frames obtained with a gain switch value of 1 or higher. In such a case, an analysis is first made of the measured frames according to the gain switches and applies the DCC according to the required correction scheme (e.g., PRO, BIN, or others). In the OPTIC2 fitting mode, there are only two options available: CAL or NUL.

4.2.1.1.1 CAL Darks

The CAL DCC method is given by (20) and is based on using the dark values recorded in the calibration files, $D_c(\lambda)$, for the instrument systems:

$$\mathfrak{S}(\lambda, t_i) = C_c(\lambda) I_f(\lambda) [V(\lambda, t_i) - D_c(\lambda)]. \quad (21)$$

This is the default mode for both OPTIC1 and OPTIC2 data types.

4.2.1.1.2 NUL Darks

The NUL dark correction scheme is a special mode in which no darks are subtracted during data calibration (note that in the OPTIC1 fitting mode, CAL darks are still subtracted for the data frames with a gain switch of zero):

$$\mathfrak{S}(\lambda, t_i) = C_c(\lambda) I_f(\lambda) V(\lambda, t_i). \quad (22)$$

The NUL DCC scheme for OPTIC3 data is explained in a later section.

4.2.1.1.3 PRO Darks

The PRO DCC option is a special mode for OPTIC1 data where a separate *dark* cast is taken. Immediately before or after a regular cast (profiler measurements with no caps on the sensors), a dark cast (profiler measurements with caps on the sensors) can be measured. Both profiles are first processed with the NUL option (i.e., no darks are subtracted), and then a second dark-corrected *light* profile, $\mathfrak{S}(z, \lambda)$, is obtained as a difference between the regular light profile, $\mathfrak{L}(z, \lambda)$ and the binned dark profile, $\langle \mathfrak{D}(z, \lambda) \rangle$:

$$\begin{aligned} \mathfrak{S}(z, \lambda) &= \mathfrak{L}(z, \lambda) - \langle \mathfrak{D}(z, \lambda) \rangle, \text{ and} \\ \langle \mathfrak{D}(z, \lambda) \rangle &= \frac{1}{M} \sum_{i=1}^M \mathfrak{D}(z_i, \lambda) \end{aligned} \quad (23)$$

where the correspondence between the light profile and the binned dark profile occurs within plus or minus half a binning interval. Dark data binning (averaging) is carried out within 1 m depth intervals.

† Explanations for the fitting modes are contained within SIFS.

4.2.1.1.4 BIN Darks

If the profiler attains a depth for which all the optical sensors reach their dark levels, the darks can be computed from the average of a number of samples at the bottom of the profile. For each wavelength, the value of DCC is obtained from a layer, defined by z_{\min} and z_{\max} , where the average minimum light values, $\langle \mathcal{L}_{\min}(z, \lambda) \rangle$, are observed:

$$\mathfrak{S}(z, \lambda) = \mathcal{L}(z, \lambda) - \langle \mathcal{L}_{\min}(z, \lambda) \rangle, \quad (24)$$

where $z = z_{\min}, \dots, z_{\max}$.

4.2.1.1.5 LUB Darks

For each wavelength, the DCC factors for $L_u(\lambda)$ values are obtained from a layer wherein average minimum light values are observed (24). At the same time, $E_d(\lambda)$ values are dark corrected with a calibrated dark value, $\mathfrak{D}_c(\lambda)$:

$$\mathfrak{S}(z, \lambda) = \mathcal{L}(z, \lambda) - \mathfrak{D}_c(\lambda), \quad (25)$$

where $z = z_{\min}, \dots, z_{\max}$.

4.2.1.1.6 LOG Darks

Prior to, or just after, a light profile (profiler measurements with no caps on), darks can be measured on the deck with the profiler caps in place. Both data files are first processed with the NUL option (i.e., no darks are subtracted), then the LOG dark-corrected light profile is obtained as a difference between the original light profile, $\mathcal{L}(z, \lambda)$, and the dark values, which are obtained at each wavelength as the result of time averaging all the calibrated dark data, $\bar{\mathfrak{D}}(\lambda)$:

$$\mathfrak{S}(z, \lambda) = \mathcal{L}(z, \lambda) - \bar{\mathfrak{D}}(\lambda). \quad (26)$$

Note that in this case, the PRESSURE TARE value is not subtracted at the time of data processing with NUL option. The value of PRESSURE TARE is estimated as an average pressure of the measurements carried out on deck. The PRESSURE TARE value is subtracted during LOG processing.

4.2.1.1.6 DCC of OPTIC3 (Hyperspectral) Data

Hyperspectral data are usually dark corrected with the values obtained from so-called *shutter darks* to obtain the most accurate correction. Shutter darks are continuously recorded during the measurements by occulting the input fiber with an optical shutter, typically after every five light samples. To calibrate hyperspectral data, the NUL DCC option should be used first, and the hyperspectral calibration and subsequent DCC factors are determined in the following steps:

1. Correct the shutter dark counts obtained from a log file, $\bar{D}(\lambda)$, by the dark offset, $D_o(\lambda)$:

$$D_s(\lambda) = \bar{D}(\lambda) - D_o(\lambda). \quad (27)$$

where $D_s(\lambda)$ is the corrected shutter dark values.

2. Convert the digital (voltage) dark counts into engineering units in accordance with the calibration equations. The calibration equation for hyperspectral data is:

$$\mathfrak{D}(\lambda) = C_c(\lambda) I_f(\lambda) D_s(\lambda) \frac{t_1}{t_2}, \quad (28)$$

where $C_c(\lambda)$ is the calibration coefficient, $I_f(\lambda)$ is the immersion coefficient, t_2 is the integration time during calibration, and t_1 is the integration time during the measurement. The former three are obtained from a calibration file, and the latter is obtained from the same log file as the optical data.

3. Check the sequence of frame numbers, and flag the frames (i.e., set to a value of -999) that are not in sequence.
4. Deglitch the dark data using a first difference filter (optional).
5. Smooth the shutter darks using a running boxcar filter.
6. Interpolate shutter darks as a function of measurement time to match the number of dark and light data measurements.
7. Correct the light data using the calibrated and corrected shutter darks:

$$\mathfrak{S}(z, \lambda) = \mathcal{L}(z, \lambda) - \mathfrak{D}(\lambda). \quad (29)$$

8. Correct the light data using the thermal responsivity correction:

$$\mathfrak{S}(z, \lambda) = \mathfrak{S}(z, \lambda) [1 + 0.01(c_1 \lambda^3 + c_2 \lambda^2 + c_3 \lambda + c_4)(T - 20)]^{-1}, \quad (30)$$

where c_1 , c_2 , c_3 , and c_4 are constants, and T is the temperature of the radiance or irradiance spectrograph ($c_1 = 6.79131 \times 10^{-9}$, $c_2 = -1.09902 \times 10^{-5}$, $c_3 = 6.51646 \times 10^{-3}$, and $c_4 = -1.31056$).

4.2.1.2 Range Check

Data that is suspect, out of range, or invalid is automatically flagged (i.e., set to a value of -999). Sensor values of -999 are not used for any computations and are ignored. On graphs, these values are not shown and, thus, are displayed as a missing section of data. The threshold limits for various sensors, which determines whether or not a particular value will be out of range, are set in the configuration file (`prosoft.cfg`).

4.2.1.3 Frame Check

ProSoft checks whether a frame counter was present. If it was, the sequence of frames, which should increase monotonically until the maximum value is reached whereupon the frame counter resets, is checked. Any frames out of sequence are flagged.

4.2.1.4 Rate Check

If the reference and profiler measurements are combined into a single data file, the data rates of both instruments (i.e., the number of frames per second) are checked (where time stamps are not available in the data). If the rates of both instruments are not equal, the following processing steps are executed (time stamps are optional during data acquisition, so the rate check and frame sequence procedures do not rely on them):

1. Information about the sequence of the reference and profiler frames is obtained from a raw binary file (the sequence can be obtained, because profiler and reference frames have unique frame counters);
2. Blank frames (i.e., frames with the variables set to values of -999) are added to the frames with the lowest data rate. This ensures that the number of frames corresponds to the measurement rates of the instruments; and
3. The blank frames that belong to the instrument with the lowest sampling frequency are removed.

Note that some blank frames could remain if the sequence of the reference and profiler data frames was not in strict accordance with the respective sampling frequencies.

4.2.1.5 Profiler Data

Profiler data are subjected to a number of corrections and checks before the level-1 data files are created. These include a) pressure tare (offset) correction, b) pressure spike check, c) wavelength sequence check, and d) a tilt quality control edit.

4.2.1.5.1 Pressure Tare Correction

Pressure sensors have a small offset value that varies with atmospheric pressure. The offset is removed by a pressure tare, which is stored in the header records by SatView when the data are acquired. The pressure tare is defined as the pressure value that is measured when the E_d sensor on the instrument system is located just at the surface. This value has to be subtracted later from the measured pressure values of a profile. If the profiler measurements were logged with SatView, the pressure tare value is optionally inserted into the file header. If no information is obtained, the pressure tare value is set to zero.

4.2.1.5.2 Wavelength Sequence Check

The wavelength sequence check resequences the optical data so that the data columns are organized from left to right as a function of increasing wavelength.

4.2.1.5.3 Pressure Spike Check

All frames with obvious pressure spikes are flagged. A deglitching procedure is applied using a threshold factor of 100 (Sect. 4.2.1.6.2).

4.2.1.5.4 Tilt Edit

Profiler measurements can be edited interactively or automatically to remove any data records with unacceptable tilt values. In manual mode, a plot is shown with profiler tilts (if available) and profiler velocity as a function of depth. With the interactive graphical editor, the user defines an upper (surface) z_{\min} and lower z_{\max} depth (the z coordinate is directed downwards). Data above z_{\min} or below z_{\max} are removed.

A tilt threshold, Tiltlimit (the default value is $\varphi_{\max}=5^\circ$ in the `prosoft.cfg` file), is usually used for estimating z_{\min} and z_{\max} . In the case of a missing (or inoperative) tilt sensor, the free-fall velocity of the profiler can be used (zero or negative velocity is assumed to be associated with high profiler tilts). An automated editor module determines z_{\min} and z_{\max} in 10% of the upper and lower part of the profiler measurements. The upper depth and the lower depth are defined as the first depth level (z) where the following conditions are satisfied:

1. $\varphi(z) < \varphi_{\max}$;
2. $z_{\min} \leq z < 0.1z_{\max}$ for the top layer of the profile; and
3. $(z_{\max} - 0.1z_{\max}) < z \leq z_{\max}$ for the bottom layer of the profile.

If a reference instrument is present, then the matching records in the reference data are also removed.

4.2.1.5.5 Output Files with the PRO Extension

The results of processing level-0 profiler data are saved in tab-delimited MAT (an optional MATLAB internal format) and ASCII formats.

4.2.1.6 Reference Data

Reference data are checked before the level-1 data files are created. These checks include the wavelength sequence check and spike deglitching.

4.2.1.6.1 Wavelength Sequence Check

The wavelength sequence check resequences the optical data so the columns are organized from left to right as a function of increasing wavelength.

4.2.1.6.2 Data Deglitching

The (optional) deglitching module is applied to data to remove obvious glitches in sensor performance. For reference data, the process begins with the application of a first difference operator to the time series of N data frames at each channel:

$$\delta(\lambda, t_i) = E_d(0^+, \lambda, t_{i+1}) - E_d(0^+, \lambda, t_i), \quad (31)$$

where t_i sets the sample index (in time or by frame count number), and the calculations occur over the interval $i = 1, \dots, N-1$.

The standard deviation for each channel, $\sigma(\lambda)$, is then calculated as:

$$\sigma(\lambda) = \left[\frac{1}{N-2} \sum_{i=1}^{N-1} \left(\delta(\lambda, t_i) - \bar{\delta}(\lambda) \right)^2 \right]^{0.5}, \quad (32)$$

where $\bar{\delta}(\lambda)$ is the average difference in the $E_d(0^+, \lambda)$ time series (of N frames). Any frames with differences more than 10σ from the average value are flagged.

The general process described above is used with other deglitching requirements, except a new threshold value is used to match the type of deglitching under consideration (e.g., pressure spike removal uses a threshold of 100).

4.2.1.6.3 Output Files with the REF Extension

The results of processing level-0 profiler data are saved in ASCII and in MAT formats.

4.2.2 Level-2 Data Processing

The level-2 ProSoft data processing produces averaged (binned) profiles from the calibrated level-1 data as level-2a output. The data from the profiler sensors are also adjusted to the same reference depth (to account for offsets in depth between the sensors). In level-2b, the reference correction of the profile for surface irradiance fluctuations can be applied. The smoothed and adjusted data are then ready for the production of the level-3 data products.

4.2.2.1 Level-2a Processing

The purpose of the level-2a processing is to provide or prepare for most of the binning and filtering options.

4.2.2.1.1 Calculation of Tilts

From the level-1 data, the x and y components of tilt measurements are obtained in degrees. The tilts are calculated using $\varphi = \tan^{-1} \sqrt{\tan^2 \varphi_x + \tan^2 \varphi_y}$, where φ_x and φ_y are the two-axis tilts with respect to the vertical.

4.2.2.1.2 Constant Wavelength Intervals

Interpolation to a constant wavelength interval can be carried out only with hyperspectral data. The interpolation interval is defined in the `prosoft.cfg` file by the `DELTA_WL` variable. If `DELTA_WL = 0`, no wavelength interpolation is performed.

4.2.2.1.3 Depth and Temporal Binning

Data processing from level-1 to level-2a performs data averaging (referred to in ProSoft as “binning”) as a function of pressure (depth) or time. If both profiler and reference or only profiler data is available, then the binning is performed as a function of pressure. Otherwise, binning

is performed as a function of time. If a profiler, for some reason, was kept at a fixed depth level for a long time, however, binning is still carried out as a function of time. A criterion for depth or time binning is based on the effective depth resolution.

The effective depth resolution is the ratio of the number of data points measured between the maximum and minimum pressure indices to the maximum change in pressure. If the effective depth resolution is less than 1 mm, binning is carried out as a function of time; otherwise binning is carried out as a function of pressure.

4.2.2.1.4 Calculation of Time and Velocity

In addition to the measured variables, level-2 data includes the variables that are derived from the measured ones: time (t) and velocity (v). Note that time stamps, which can be added to a file during data acquisition, are optional. For this reason, ProSoft cannot rely solely on time stamps, but rather has to generate the time for each data frame using the start time, t_0 (in hours), and the sampling frequency, f_s (in hertz):

$$t_i = t_0 + \frac{i-1}{3600 f_s}, \quad (33)$$

where the calculations are performed over the interval $i = 1, \dots, N$.

The velocity at each data frame is computed as

$$v(t_i) = f_s [z(t_{i+1}) - z(t_i)], \quad (34)$$

and calculated over the interval $i = 1, \dots, N$. After the computation is made, the velocity is smoothed using a boxcar filter with a filter width of M . The value of M is the product of `VEL_SMOOTH_TIME` times f_s (`VEL_SMOOTH_TIME` has units of seconds and is set within the `prosoft.cfg` file).

4.2.2.1.5 Binning

Binning is performed in several steps. In the first step, each instrument (i.e., profiler or reference) form an index vector that includes the sequential indices of the frames. The frame indices, F_i , depend on the measurement rate of an instrument in the following way:

$$F_i(i) = 1 + (i-1)f_r, \quad i = 1, \dots, N, \quad (35)$$

where N is the number of frames (measurements) carried out at a maximum rate, and f_r is an integer part of the rates ratio given by `MAXIMUM_RATE`/ $f_s(j)$ for $j = 1, \dots, N_I$ and N_I is the number of instruments (usually $N_I = 2$). If the rates of all instruments are equal, $F_i(i) = i$ over the interval $i = 1, \dots, N$.

In the second binning step, a coordinate vector must be chosen (i.e., time or pressure) corresponding to the binning that will be performed (Sect. 4.2.2.1.3). If depth (pressure)

binning is selected, the data are interpolated to ensure the difference between sequential frames is a constant (the default resampling is 0.1 m).

The third binning step adjusts the location between the E_d sensor and the other optical sensors based on the depth differences between the sensors. For example, the pressure measured at the L_u sensor is the pressure measured at the E_d sensor minus the PRO_LU_DIST value given in the `prosoft.cfg` file.

The binning along the chosen coordinate vector is carried out in the fourth step. Currently, it is assumed that profiler measurements are always carried out at a higher rate, and prior to binning, the optical data are log transformed (whether or not the data are log transformed depends on switches given in the `prosoft.cfg` file).

In the fifth and final step, the profiler optical data, other than E_d , are adjusted to match the depth of the first E_d measurement (in the `prosoft.cfg` file, the respective sensor distance offsets are given by PRO_SENSORNAME_DIST, where SENSORNAME is, for example, Lu or Eu). Extrapolation is based on a linear regression fit of the log-transformed data versus pressure. The number of points used in the linear regression calculation is defined in the `prosoft.cfg` file by the variable NUM_K_BINS.

4.2.2.2 Level-2b Processing

The purpose of the level-2b data processing is to comply with the SeaWiFS Ocean Optics Protocols (Mueller and Austin 1995) and as formulated in Smith and Baker (1984 and 1986), by weighting the in-water profiler data by the surface irradiance. The weighting is carried out using:

$$\mathfrak{S}(z, \lambda, t_0) = \mathfrak{S}(z, \lambda, t) \frac{E_d(0^+, \lambda, t_0)}{E_d(0^+, \lambda, t)}, \quad (36)$$

but note that this procedure is different from the alternate method also given in Mueller and Austin (1995) using the solar irradiance measured when the profiler was at the surface ($z = 0^-$)†. The reason for this difference is mainly related to the problem that $E_d(0^-, \lambda)$ is often unavailable, so ProSoft uses (36) instead.

Level-2a to level-2b processing automatically follows the level-1 to level-2a processing if the REF_CORRECT_PRO variable is enabled (turned ON) in the `prosoft.cfg` file. Note also that the weighting given by (36) often introduces significant variations in the profiler data, particularly when clouds are present, so the default is for REF_CORRECT_PRO to be disabled (set OFF).

4.2.3 Level-3 Data Processing

The level-3 data processing is based mostly on the level-2 data. An exception is the estimation of the diffuse attenuation coefficient and the related level-3 products from the level-1 (unaveraged) radiometric data. In

general, level-3 data processing can be divided into two parts: a) calculation of the products at the surface, and b) calculation of the products based only on the profiler measurements.

The calculation of the products at the surface involves three steps:

1. Propagation of all the radiometric data to the null depth, $z = 0^-$, level;
2. Propagation of the radiometric data through the air-sea interface and, thus, above the surface, $z = 0^+$; and
3. Calculation of the various products, such as, the remote sensing reflectance, reflectance, normalized water-leaving radiance, diffuse attenuation coefficient, PAR, and pigment concentration.

In addition to the surface products, level-3 (vertical) profile products are calculated and involve the estimation of the diffuse attenuation coefficient, PAR, pigment concentration, remote sensing reflectance, and reflectance.

4.2.3.1 Surface K

Surface values of $K(\lambda)$ and the primary radiometric variables, i.e., $E_d(\lambda)$ and $L_u(\lambda)$, are obtained from a least-squares regression fit to the first N (looking down from the surface) log-transformed radiometric and depth (or pressure) data points, expressed here in terms of the data indices‡:

$$\ln [\mathfrak{S}(z_i, \lambda)] = \ln [\mathfrak{S}(z_0, \lambda)] - K_{\mathfrak{S}}(z_0, \lambda) z_i, \quad (37)$$

where z_i sets the sample index in terms of the depth (or the frame count), z_0 denotes the surface value (or initial frame count), and the calculations occur over the interval $i = 1, \dots, N - 1$.

4.2.3.2 K Profile

A vertical profile of $K(\lambda)$ is obtained from a least-squares regression fit which is applied to the N data points at a time

$$\ln [\mathfrak{S}(z_i, \lambda)] = \ln [\mathfrak{S}(z_m, \lambda)] - K_{\mathfrak{S}}(z_0, \lambda)(z_i - z_m), \quad (38)$$

where $i = m + 1, \dots, m + N$ and $m = 1, \dots, M - N$, and M is the number of data points at a profile.

4.2.3.3 K from Fixed Depth Measurements

In some cases, $K(\lambda)$ has to be estimated from a time series of upwelling radiance measurements, collected at a

† See Mueller and Austin (1995), Sect. 6.1.3, page 49.

‡ Formulated from (31) on page 50 of Mueller and Austin (1995), which is based on the Smith and Baker (1984 and 1986) traditional method of K analysis.

fixed depth (approximately 1 m) below the surface (this type of measurement is a common feature of nonprofiling instruments, like surface buoys). In this case, ProSoft estimates the spectrum of $K(\lambda)$ based on an empirical model (valid for Case-1 conditions):

1. Compute $K(490)$ and $K(520)$ from $L_u(443)$ and $L_u(550)$ using the Austin and Petzold (1981) algorithms:

$$K(490) = 0.022 + 0.0883 \left[\frac{L_u(443)}{L_u(550)} \right]^{-1.491} \quad (39)$$

and

$$K(520) = 0.044 + 0.0663 \left[\frac{L_u(443)}{L_u(550)} \right]^{-1.398}$$

2. The Morel (1988) Case-1 empirical model for estimating K is inverted to obtain the pigment concentration C (chlorophyll a plus phaeopigments):

$$C_{490} = \left[\frac{K(490) - K_w(490)}{\chi_c(490)} \right] e^{-1(490)},$$

$$C_{520} = \left[\frac{K(520) - K_w(520)}{\chi_c(520)} \right] e^{-1(520)} \quad (40)$$

and

$$C = \frac{C_{490} + C_{520}}{2},$$

where $K_w(\lambda)$ represents the diffuse attenuation coefficient for pure water, and the coefficients $\chi_c(\lambda)$ and $e(\lambda)$ are regression coefficients determined by statistical analysis of $K(\lambda)$ in Case-1 water for the wavelength range 400–700 nm (Morel 1988).

3. The algorithm for computing $K(\lambda)$ is as follows:

$$K(\lambda) = K_w(\lambda) + \chi_c(\lambda) C e(\lambda). \quad (41)$$

To calculate $K(\lambda)$ within the 700–800 nm range, Prosoft uses the following steps:

- i) The values of $K_w(\lambda)$ within 700–800 nm are obtained from Smith and Baker (1981);
- ii) It is assumed that $\chi_c(\lambda)$ and $e(\lambda)$ decrease linearly from the values given at $\chi_c(700)$ and $e(700)$ to 0 at 800 nm; and
- iii) Using the above assumptions and $K_w(\lambda)$ within 700–800 nm, $K(\lambda)$ can be estimated for the 700–800 nm interval.

4.2.3.4 Remote Sensing Reflectance

The remote sensing reflectance is calculated using the ratio of the water-leaving radiance and incident solar irradiance, $R_{rs}(\lambda) = L_w(\lambda)/E_d(0^+, \lambda)$. $L_w(\lambda)$ is defined

as, $L_w = L_u(0^-, \lambda)(1 - \rho(\lambda, \vartheta))n_w^{-2}(\lambda)$, where $\rho(\lambda, \vartheta)$ is fixed at 0.021 for normal incidence, and $n_w^2(\lambda) = 1.345$ for seawater (Austin 1974). For the latter, if an above-water reference is unavailable, the incident solar irradiance is derived from the profiler $E_d(z, \lambda)$ measurements:

$$E_d(0^+, \lambda) = (1 + \alpha) E_d(0^-, \lambda), \quad (42)$$

where α is the Fresnel reflection albedo for irradiance from sun and sky (Gordon et al. 1988) which is fixed at 0.043. For these formulations, ρ and α are assumed independent of wind speed (Priesendorfer and Mobley 1986).

4.2.3.5 Normalized Water-Leaving Radiance

The normalized water-leaving radiance is estimated using (63) of the SeaWiFS Ocean Optics Protocols (Mueller and Austin 1995):

$$[L_w(\lambda)]_N = L_w \frac{\bar{F}_0(\lambda)}{E_d(0^+, \lambda)}, \quad (43)$$

where, in ProSoft, the Neckel and Labs (1984) mean extraterrestrial solar irradiance data are reinterpolated to a 0.1 nm resolution and then smoothed to match the 10 nm bandwidth of the radiometer detectors. The $L_w(\lambda)$ term in (43) is computed following the discussion in Sect. 4.2.3.4.

4.2.3.6 PAR

PAR, in units of quanta $\text{cm}^{-2} \text{s}^{-1}$, is estimated using:

$$\text{PAR} = \int_{400}^{700} \frac{\lambda}{hc} E_d(\lambda) d\lambda, \quad (44)$$

where h is Planck's constant, and c is the speed of light. The PAR formulation (44) is used for estimating PAR at the surface as well as for vertical profiles of PAR. ProSoft uses the MATLAB trapezoidal numerical integration routine `trapz.m` to perform the integration in (44). Prior to integration, $E_d(\lambda)$ is interpolated onto a constant 1 nm interval and a minimum-maximum wavelength check is performed:

$$\begin{aligned} \text{if } \lambda_1 > 400 &\Rightarrow E_d(400) = E_d(\lambda_1), \text{ and} \\ \text{if } \lambda_N < 700 &\Rightarrow E_d(700) = E_d(\lambda_N). \end{aligned} \quad (45)$$

4.2.3.7 Energy Flux

The energy flux, F_E , is computed as:

$$F_E = 100 \int_{400}^{700} E_d(\lambda) d\lambda, \quad (46)$$

ProSoft uses the MATLAB trapezoidal numerical integration routine `trapz.m` to perform the integration in (46). Prior to integration, $E_d(\lambda)$ is interpolated onto a constant 1 nm interval, and a minimum-maximum wavelength check

is performed as in (45). F_E is given in units of W m^{-2} , and because E_d is in units of $\mu\text{W cm}^{-2} \text{ nm}^{-1}$, a scaling factor of 100 is used in (46). The energy flux equation (46) is used for estimating F_E at the surface, as well as for vertical profiles of F_E .

4.2.3.8 Estimating K Using Wavelet Analysis

This section describes a new methodology for computing K using the K from multiresolution (KMR) wavelet analysis method (Sildam et al. 1998). This level-3 module uses high resolution level-1 (unaveraged) data instead of the standard (Smith and Baker 1984 and 1986) method which uses level-2 (averaged) data.

The following modules in ProSoft are experimental and are intended for advanced users. These subroutines do not follow the SeaWiFS Ocean Optics Protocols (Mueller and Austin 1995) and should not be used for submitting data to SeaBASS until further validation has been done.

Estimation of K from optical profiles involves ambiguity in the choice of the vertical scale. Usually, a noisy profile of K is obtained if K is estimated directly from:

$$K(z, \lambda) = \frac{-1}{E_d(z, \lambda)} \frac{\Delta E_d}{\Delta z}, \quad (47)$$

where $\Delta E_d = E_d(z_{n+1}, \lambda) - E_d(z_n, \lambda)$ is calculated at the resolution of the measurements, Δz . If ΔE_d is estimated at an increased vertical scale $m\Delta z$, i.e., $\Delta E_d = E_d(z_{n+m}, \lambda) - E_d(z_n, \lambda)$, smoother—but less detailed—profiles of K are obtained. Note that a similar problem holds also for estimating K using (38). The objective of the KMR methodology is to define an optimal depth interval for the determination of K that is objectively and automatically determined.

Estimation of the K profile from discrete irradiance or radiance measurements makes the assumption that any observed profile can be divided into optically homogeneous layers. Usually the choice of the thickness of these layers is subjective. Moreover, it varies with wavelength, depth, time, and the geographical location of the measurements. Multiresolution wavelet decomposition of a $K(z, \lambda)$ profile (that is calculated with a fixed high vertical resolution) provides a hierarchy of profiles of $K(z_m, \lambda)$ which are obtained by smoothing $K(z, \lambda)$ at different vertical scales. An optimal choice of the averaging scale at any depth level could then be based on a statistical approach (i.e., on the analysis of the K frequency distribution).

In practice, having a few K estimates at a fixed depth, results in an inconclusive analysis of the K frequency distribution. Frequency analyses, however, can be carried out over all observed depth levels if K is centralized and normalized by its standard deviation. The results of such an analysis show that in optically clear waters, recursive wavelet decomposition of the K profile combined with median averaging can be used to obtain K profiles, which asymptotically reach the state of maximum probability (Sildam et al. 1998).

4.2.3.8.1 Mathematics of the KMR Method

Multiresolution orthogonal Haar wavelet transforms decompose the $K(z, \lambda)$ profile into M profiles at M scales, so that $K(z_m, \lambda)$ at different scales are related to each other as:

$$K(z_{m-1}, \lambda) = K(z_m, \lambda) + K'(z_m, \lambda), \quad (48)$$

where $m = 1, \dots, M$ and $K'(z_m, \lambda)$ is the so-called *detail*. $K(z_m, \lambda)$ is given by:

$$K(z_m, \lambda) = \sum_{n=-\infty}^{\infty} C_{m,n} \phi_{m,n}(z), \quad (49)$$

where

$$\begin{aligned} C_{m,n} &= \int K(z) \phi_{m,n}(z) dz, \\ \phi_{m,n} &= \frac{1}{\sqrt{2^m}} \phi\left(\frac{z - n2^m \delta z}{2^m}\right), \text{ and} \\ \phi(z) &= \begin{cases} 1, & 0 \leq z < 1; \\ 0, & \text{otherwise.} \end{cases} \end{aligned} \quad (50)$$

In (49), the depth location and scale are given by the n and m indices, respectively, $\phi_{m,n}$ is the so-called *smoothing function*, and $\phi(z)$ is Haar's *scaling function*.

In the KMR method, at every depth level z , $m = 1, \dots, M$ estimates of $K(z_m, \lambda)$ can be obtained. From these M profiles, a median profile $\langle K(z, \lambda) \rangle$ can be easily obtained. The median profile can be decomposed once again using the Haar scaling function, and a new median profile can be obtained. This iterative procedure can be repeated several times until an asymptotic $K(\lambda)$ is reached.

4.2.3.8.2 Practical Steps of the KMR Method

The practical steps of the KMR method are as follows.

1. Estimate the $K(z, \lambda)$ profile using

$$K(z, \lambda) = \frac{1}{\Delta z} \ln \left[\frac{E_d(z_i, \lambda)}{E_d(z_{i+n}, \lambda)} \right], \quad (51)$$

where $\Delta z = z_{i+n} - z_i$ represents the maximum allowed resolution (if $i = 1$, the maximum allowed resolution is equal to the depth resolution of the measurements).

2. Apply the Haar multiresolution wavelet decomposition (50) to $K(z, \lambda)$. As a result, obtain M profiles of $K(z_m, \lambda)$, each calculated with a depth scale given by $(z_i - z_{i+1})2^m$, where $m = 1, \dots, M$. Note that n and m represent the minimum and maximum number of points, respectively, used in estimation of $K(z_m, \lambda)$.
3. From the $K(z_m, \lambda)$ profiles ($m = 1, \dots, M$), estimate a median profile, $\langle K(z, \lambda) \rangle$.
4. Repeat steps 2 and 3, each time using newly obtained $\langle K(z, \lambda) \rangle$ until an asymptotic limit is reached.

4.3 SUMMARY

The standard (40-cast) DARR-00 data were processed with ProSoft. Level-2 and level-3 products were submitted including $[L_W(\lambda)]_N$. For all the data, the K analyses (using the methods described in Sect. 4.2.3.1) were executed using the auto-edited profiles as produced by ProSoft. For Case-2 water comparison, K was computed with and without editing, ignoring near surface tilts for one example. All files (light and dark) were processed first using the NUL dark correction. Once all the data were converted to engineering units, the LOG dark correction was used to subtract the DARK casts from the LIGHT. Table 23 presents a sum-

mary of the ProSoft settings in the `prosoft.cfg` file for each of the instrument systems.

Table 23. The ProSoft configuration parameters used for processing the standard DARR-00 (40-cast) data set.

<i>Parameter</i>	<i>MN</i>	<i>WP</i>	<i>LN</i>	<i>SO</i>
PRO_LU_DIST	0.160	0.055	1.779	0.183
PRO_EU_DIST	1.021	0.045	1.787	0.181
PRES_TAR2	0.258	0.030	0.569	0.177
PRES_BIN_INT	1	1	1	1
NUM_K_BINS	5	5	5	5

APPENDICES

- A. The DARR-00 Science Team
- B. The DARR-00 Database

APPENDIX A

The DARR-00 Science Team

The DARR-00 science team is presented alphabetically.

Jean-François Berthon
JRC/SAI/ME T.P. 272
I-21020 Ispra (VA)
ITALY
Voice: 39-0-332-789-934
Fax: 39-0-332-789-034
Net: jean-francois.berthon@jrc.it

Davide D'Alimonte
JRC/SAI/ME T.P. 272
I-21020 Ispra (VA)
ITALY
Voice: 39-0-332-785-727
Fax: 39-0-332-789-034
Net: davide.d'alimonte@jrc.it

Stanford Hooker
NASA/GSFC/Code 970.2
Greenbelt, MD 20771
Voice: 301-286-9503
Fax: 301-286-1775
Net: stan@ardbeg.gsfc.nasa.gov

Stéphane Maritorena
ICES/UCSB
Santa Barbara, CA 93106
Voice: 805-893-2544
Fax: 805-893-2578
Net: stephane@icess.ucsb.edu

Scott McLean
Satlantic, Inc.
Richmond Terminal, Pier 9
3481 North Marginal Road
Halifax, Nova Scotia B3K 5X8
CANADA
Voice: 01-902-492-4780
Fax: 01-902-492-4781
Net: scott@satlantic.com

Juri Sildam
Satlantic, Inc.
Richmond Terminal, Pier 9
3481 North Marginal Road
Halifax, Nova Scotia B3K 5X8
CANADA
Voice: 01-902-492-4780
Fax: 01-902-492-4781
Net: juri@satlantic.com

Giuseppe Zibordi
JRC/SAI/ME T.P. 272
I-21020 Ispra (VA)
ITALY
Voice: 39-0-332-785-902
Fax: 39-0-332-789-034
Net: giuseppe.zibordi@jrc.it

APPENDIX B

The DARR-00 Database

A short summary of the data files used to create the DARR-00 database is given in Table B1.

GLOSSARY

- A/D Analog-to-Digital
- AAOT *Acqua Alta* Oceanographic Tower
- AMT Atlantic Meridional Transect
- AOP Apparent Optical Property
- ASCII American Standard Code for Information Interchange
- CoASTS Coastal Atmosphere and Sea Time-Series
- COLORS Coastal Region Long-Term Measurements for Colour Remote Sensing Development and Validation
- CT Conductivity and Temperature (probe)
- DAAC Distributed Active Archive Center
- DARR Data Analysis Round Robin
- DARR-94 The First DARR (July 1994)
- DARR-00 The Second DARR (March 2000)
- DCC Dark Current Correction
- DCM Depth of the Chlorophyll Maximum
- DO Deep Ocean
- EOF End-of-File
- ET Eutrophic
- FF Free-Fall
- GMT Greenwich Mean Time
- GS GSFC and Satlantic (comparison)
- GSFC Goddard Space Flight Center
- GUI Graphical User Interface
- HPLC High Performance Liquid Chromatography
- ICES (UCSB) Institute for Computational Earth System Science
- IDL Interactive Data Language
- IOP Inherent Optical Property
- JCR (Royal Research Ship) *James Clark Ross*
- JG JRC and GSFC (comparison)
- JGOFS Joint Global Ocean Flux Study
- JRC Joint Research Centre
- JS JRC and Satlantic (comparison)
- KMR *K* from Multiresolution (wavelet analysis)
- LN LoCNESS
- LoCNESS Low-Cost NASA Environmental Sampling System
- miniNESS miniature NASA Environmental Sampling System
- MLD Mixed Layer Depth
- MN miniNESS
- MT Mesotrophic
- NASA National Aeronautics and Space Administration
- NIST National Institute of Standards and Technology
- OC Ocean Color
- OC2v2 Ocean Color (algorithm) 2 Version 2
- OCI-200 Ocean Color Irradiance series 200 (sensor)
- OCR-200 Ocean Color Radiance series 200 (sensor)
- OLL One-Percent Light Level
- OT Oligotrophic

Table B1. The DARR-00 data set. The data that was part of the 40-cast data set is indicated by “(40)” next to the file name; the data that was added to create the 50-cast data set is indicated by “(50)” next to the file name. The concentration of total chlorophyll *a*, C_{Ta} , is given in units of milligrams per cubic meter.

LoCNESS (FF, DO)				SeaOPS (WC, DO)			
File Name	Longitude [°]	Latitude [°]	C_{Ta}	File Name	Longitude [°]	Latitude [°]	C_{Ta}
A07KD005 (40)	-10.7960	41.5791	0.28	A060U025 (40)	12.4044	-21.6534	1.66
A07KD020 (40)	-17.5773	14.9881	0.49	A060D028 (40)	12.4042	-21.6520	1.66
A07KD025 (40)	-21.3139	12.1723	1.18	A060D029 (40)	12.4042	-21.6529	1.66
A07KD028 (40)	-23.7503	4.2843	0.16	A060D030 (40)	12.1015	-21.3989	1.79
A07KD030 (40)	-23.7499	4.2864	0.16	A060U031 (40)	12.1011	-21.3984	1.79
A07KD040 (40)	-30.4334	-12.1615	0.08	A060D032 (40)	11.9995	-18.9960	1.86
A07KD045 (40)	-30.5133	-12.3743	0.08	A060D033 (40)	11.3314	-17.6599	2.43
A07KD060 (40)	-36.8965	-23.4888	0.13	A060D034 (40)	11.3315	-17.6601	2.43
A07KD070 (40)	-40.4902	-27.0146	0.29	A060D035 (40)	11.0733	-17.4396	0.82
A07KD090 (40)	-46.6759	-32.7510	0.10	A060D039 (40)	-2.6308	-5.8635	0.24
A06LD039 (50)	-19.9964	25.0854	0.03	A070U005 (50)	-13.6048	38.7815	0.09
A06LD041 (50)	-19.5624	29.0873	0.03	A070D007 (50)	-17.4900	36.3089	0.06
A06LD045 (50)	-17.1673	32.6517	0.03	A070U010 (50)	-19.9454	30.0624	0.09
A07KD009 (50)	-17.4967	36.0950	0.04				
A07KD047 (50)	-32.1382	-16.2339	0.04				
A07KD056 (50)	-35.1391	-19.8250	0.06				
A07KD092 (50)	-46.7654	-32.8267	0.07				
miniNESS (FF, SC)				WiSPER (WC, SC)			
P56S1H (40)	12.5083	45.3139	0.97	W56S1A (40)	12.5083	45.3139	0.97
P56S4D (40)	12.5083	45.3139	1.54	W56S4A (40)	12.5083	45.3139	1.54
P56S7G (40)	12.5083	45.3139	1.22	W56S7A (40)	12.5083	45.3139	1.22
P58S4B (40)	12.5083	45.3139	0.48	W58S4A (40)	12.5083	45.3139	0.48
P60S4R (40)	12.5083	45.3139	0.83	W60S4A (40)	12.5083	45.3139	0.83
P60S6C (40)	12.5083	45.3139	0.65	W60S6A (40)	12.5083	45.3139	0.65
P61S5J (40)	12.5083	45.3139	0.68	W61S5A (40)	12.5083	45.3139	0.68
P61S6E (40)	12.5083	45.3139	0.87	W61S6A (40)	12.5083	45.3139	0.87
P62S4F (40)	12.5083	45.3139	2.02	W62S4A (40)	12.5083	45.3139	2.02
P63S3B (40)	12.5083	45.3139	0.54	W63S3A (40)	12.5083	45.3139	0.54

PAR Photosynthetically Available Radiation

S/N Serial Number

SC Shallow Coastal

SDY Sequential Day of the Year

SeaBASS SeaWiFS Bio-Optical Archive and Storage System

SeaOPS SeaWiFS Optical Profiling System

SeaWiFS Sea-viewing Wide Field-of-view Sensor

SIFS Satlantic Instrument Files Standard

SIRREX SeaWiFS Intercalibration Round-Robin Experiment

SO SeaOPS

SOOP SeaWiFS Ocean Optics Protocols

SQM SeaWiFS Quality Monitor

THOR Three-Headed Optical Recorder

UCSB University of California at Santa Barbara

UPD Unbiased Percent Difference

V1 Version 1

V2 Version 2

V3 Version 3

V4 Version 4

V5 Version 5

WC Winch and Crane

WiSPER Wire-Stabilized Profiling Environmental Radiometer

WP WiSPER

SYMBOLS

 a The spectral seawater absorption. A The processor code for the first data product. B The processor code for the second data product. \mathfrak{B} The band-ratio data product being compared. \mathfrak{B}^A The first band-ratio data product being compared. \mathfrak{B}^B The second band-ratio data product being compared. c The speed of light. C Pigment concentration (chlorophyll *a* plus phaeopigments). C_{490} The pigment concentration contribution at 490 nm. C_{520} The pigment concentration contribution at 520 nm. $C_c(\lambda)$ The calibration coefficient. $C_{m,n}$ A summation coefficient in the KMR method. C_{Ta} The total chlorophyll *a* concentration. c_1 A thermal responsivity constant. c_2 A thermal responsivity constant. c_3 A thermal responsivity constant. c_4 A thermal responsivity constant.

- d* The SDY.
- $\mathfrak{D}(\lambda)$ The calibrated spectral dark value (in engineering units).
- $\mathfrak{D}(z_i)$ A dark (profile) value at depth z_i .
- $\langle \mathfrak{D}(z, \lambda) \rangle$ A binned spectral dark profile.
- $\bar{D}(\lambda)$ The spectral (time) averaged dark value in digital counts (usually measured during a special *dark cast* with the caps on the radiometer).
- $\bar{\mathfrak{D}}(\lambda)$ The spectral (time) averaged dark value in engineering units.
- $D_c(\lambda)$ The spectral dark values in a calibration file (in digital counts).
- $\mathfrak{D}_c(\lambda)$ The calibrated spectral dark values from a calibration file (in engineering units).
- $D_o(\lambda)$ The spectral dark offset (capped darks).
- $D_s(\lambda)$ The corrected spectral shutter darks from a log file.
- dz A depth increment interval ($z - z_0$).
- $e(\lambda)$ A spectral regression coefficient.
- $E_d(0^-, \lambda)$ The spectral downward irradiance immediately below the sea surface.
- $E_d(0^+, \lambda)$ The incident solar irradiance immediately above the sea surface (direct plus diffuse).
- $\bar{E}_d(0^+, \lambda)$ The spectral mean of a set of $E_d(0^+, \lambda)$ values.
- $E_d(z, \lambda)$ The spectral downward irradiance profile.
- $E_i(0^+, \lambda)$ The diffuse solar irradiance immediately above the sea surface.
- $E_u(0^-, \lambda)$ The spectral upward irradiance immediately below the sea surface.
- $E_u(z, \lambda)$ The spectral upward irradiance profile.
- \mathfrak{F} The data product being compared.
- \mathfrak{F}^A The first data product being compared.
- \mathfrak{F}^B The second data product being compared.
- f_r The integer part of the rates ratio.
- f_s The sampling frequency.
- $F_0(\lambda, d)$ The mean extraterrestrial solar irradiance corrected for the Earth-sun distance.
- $\bar{F}_0(\lambda)$ The mean extraterrestrial solar irradiance.
- F_E The energy flux.
- F_i The frame index.
- G* A data product computed with the GSFC processor.
- $\mathfrak{G}(\lambda)$ The calibrated value from the GSFC processor [\mathfrak{G} is replaced by $E_d(z)$, $E_u(z)$, $L_u(z)$, or $E_d(0^+)$].
- h* Plank's constant.
- i* A sequential index.
- $I_f(\lambda)$ The (spectral) immersion factor.
- j* A sequential index.
- J* A data product computed with the JRC processor.
- $\mathfrak{J}(\lambda)$ The calibrated value from the JRC processor [\mathfrak{J} is replaced by $E_d(z)$, $E_u(z)$, $L_u(z)$, or $E_d(0^+)$].
- k* A wavelength index.
- $K(\lambda)$ The spectral diffuse attenuation coefficient.
- $\langle K(z, \lambda) \rangle$ A median $K(\lambda)$ profile.
- $K'(z_m, \lambda)$ The so-called *detail* in the KMR method.
- $K_d(\lambda)$ The spectral diffuse attenuation coefficient computed from the downward irradiance.
- $\bar{K}_d(\lambda)$ The mean diffuse attenuation coefficient.
- $K_{Ed}(\lambda)$ The spectral diffuse attenuation coefficient computed from the downward irradiance; also denoted $K_d(\lambda)$.
- $K_{Eu}(\lambda)$ The spectral diffuse attenuation coefficient computed from the upward irradiance; also denoted $K_u(\lambda)$.
- $K_{\mathfrak{G}}(\lambda)$ The spectral diffuse attenuation coefficient computed with the GSFC processor [\mathfrak{G} is L_u , E_d , or E_u].
- $K_{\mathfrak{J}}(\lambda)$ The spectral diffuse attenuation coefficient computed with the JRC processor [\mathfrak{J} is L_u , E_d , or E_u].
- $K_L(\lambda)$ The spectral diffuse attenuation coefficient computed from the upwelled radiance.
- $K_{Lu}(\lambda)$ The spectral diffuse attenuation coefficient computed from the upwelled radiance; also denoted $K_L(\lambda)$.
- $K_{\mathfrak{S}}(\lambda)$ The spectral diffuse attenuation coefficient computed with the Satlantic processor [\mathfrak{S} is L_u or E_d].
- $K_u(\lambda)$ The spectral diffuse attenuation coefficient computed from the upward irradiance.
- $K_w(\lambda)$ The spectral diffuse attenuation coefficient for pure water.
- l* A wavelength index.
- $\mathfrak{L}(z, \lambda)$ A spectral light profile.
- $\langle \mathfrak{L}_{\min}(\lambda) \rangle$ The average minimum spectral light values.
- $L_u(0^-, \lambda)$ The spectral upwelled radiance immediately below the sea surface.
- $L_u(z, \lambda)$ The spectral upwelled radiance profile.
- $L_w(\lambda)$ The spectral water-leaving radiance.
- $[L_w(\lambda)]_N$ The spectral normalized water-leaving radiance.
- m* A sequential index.
- M* The boxcar filter width.
- n* The number of standard deviations used in a statistical filter.
- $n_w(\lambda)$ The spectral refractive index of seawater.
- N* The number of data frames.
- N_b The number of spectral bands being averaged.
- \bar{N}_G The average number of points in the extrapolation ranges for the GSFC processing.
- N_I The number of instruments (usually $N_I = 2$).
- \bar{N}_J The average number of points in the extrapolation ranges for the JRC processing.
- N_m The number of measurements being compared.
- $Q_n(0^-, \lambda)$ The spectral nadir *Q*-factor immediately below the sea surface.
- $r(\lambda)$ The spectral diffuse-to-direct solar irradiance ratio.
- $R(\lambda)$ The spectral irradiance reflectance.
- $R_{rs}(\lambda)$ The spectral remote sensing reflectance.
- S* A data product computed with the Satlantic processor.
- $\mathfrak{S}(\lambda)$ The calibrated value from the Satlantic processor [\mathfrak{S} is replaced by $E_d(z)$, $E_u(z)$, $L_u(z)$, or $E_d(0^+)$].
- t* The time coordinate.
- T* The temperature of the radiance or irradiance spectrograph.
- t_i The time associated with a data sample.
- t_0 A reference time (generally chosen to coincide with the start of a cast).
- t_1 The integration time during a measurement.
- t_2 The integration time during calibration.
- v* The velocity of a profiler.
- $V(\lambda)$ The raw (spectral) voltage (in digital counts) measured by an instrument.
- x* The abscissa coordinate.

- y The ordinate.
- z The vertical (depth) coordinate.
- z_0 A reference depth.
- z_1 The bottom (depth) of the extrapolation interval.
- z_b A depth near the bottom of a cast.
- z_i The sample index in terms of the depth.
- z_{\max} The maximum depth for a vertical layer.
- z_{\min} The minimum depth for a vertical layer.
- α The Fresnel reflection albedo for irradiance from sun and sky.
- δt A time interval.
- δz The vertical bin size (in meters).
- $\delta(\lambda, t_i)$ The spectral first difference operator for times t_i and t_{i+1} .
- $\bar{\delta}(\lambda)$ The spectral average difference.
- $\delta_0(d)$ The Earth-sun distance correction.
- ΔE_d A difference in E_d between two depth levels (or indices).
- $\Delta \bar{N}$ The average difference in the number of points in the extrapolation ranges for the JRC and GSFC processors.
- Δz The maximum allowed resolution.
- θ The solar zenith angle.
- ϑ The nadir angle.
- λ Wavelength.
- λ_{1-5} The blue-green wavelengths, nominally 412–555 nm (channels 1–5).
- $\lambda_{3/5}$ The blue-green wavelength ratio, nominally 490 and 555 nm (channels 3 and 5, respectively).
- λ_{6-7} The red wavelengths, nominally 665–683 nm (channels 6–7).
- λ_{1-7} All the wavelengths, nominally 412–683 nm (channels 1–7).
- $\lambda_{k/l}$ Denotes the wavelengths (by channel number) involved in a band-ratio data product for wavelengths k and l (the data product for wavelength k is divided by the data product for wavelength l).
- $\rho(\lambda)$ The spectral Fresnel surface reflectance.
- $\rho_s(\lambda)$ The sea surface reflectance for downward irradiance.
- σ The standard deviation.
- φ The sensor tilt with respect to the vertical axis.
- φ_{\max} The maximum allowed tilt.
- φ_x The x -axis tilt.
- φ_y The y -axis tilt.
- $\Phi_{\mathfrak{B}}^{AB}(\lambda_{k/l})$ The UPD between two band-ratio data products $\mathfrak{B}^A(\lambda_{k/l})$ and $\mathfrak{B}^B(\lambda_{k/l})$.
- $\Phi_{3/5}$ The average of the band-ratio results calculated for 490 and 555 nm (bands three and five, respectively).
- $\phi(z)$ Haar's scaling function.
- $\phi_{m,n}$ The so-called smoothing function (used with the KMR method).
- $\chi_c(\lambda)$ A spectral regression coefficient.
- $\bar{\psi}_{\mathfrak{F}}^{AB}(\lambda)$ The average UPD between two data products \mathfrak{F}^A and \mathfrak{F}^B .
- $\Psi_{\mathfrak{F}}^{AB}(\lambda)$ The spectral average of the UPD between two data products \mathfrak{F}^A and \mathfrak{F}^B .

- Ψ_{1-7} The spectral UPD average over all (seven) wavelengths, 412–683 nm (channels 1–7).
- Ψ_{1-5} The spectral UPD average of the (five) wavelengths in the blue-green part of the spectrum, 412–555 nm (channels 1–5).
- Ψ_{6-7} The spectral UPD average of the (two) wavelengths in the red part of the spectrum, 665–683 nm (channels 6–7).
- $\omega(\lambda)$ The spectral single scattering albedo for seawater.

REFERENCES

- Aiken, J., and S.B. Hooker, 1997: The Atlantic Meridional Transect: Spatially extensive calibration and validation of optical properties and remotely-sensed measurements of ocean color. *Backscatter*, **8**, 8–11.
- , D.G. Cummings, S.W. Gibb, N.W. Rees, R. Woodd-Walker, E.M.S. Woodward, J. Woolfenden, S.B. Hooker, J-F. Berthon, C.D. Dempsey, D.J. Suggett, P. Wood, C. Donlon, N. González-Benítez, I. Huskin, M. Quevedo, R. Barciela-Fernandez, C. de Vargas, and C. McKee, 1998: Cruise Report. *NASA Tech. Memo. 1998-206892*, Vol. 2, S.B. Hooker and E.R. Firestone, Eds., NASA Goddard Space Flight Center, Greenbelt, Maryland, 113 pp.
- , N.W. Rees, S. Hooker, P. Holligan, A. Bale, D. Robins, G. Moore, R. Harris, and D. Pilgrim, 2000: The Atlantic Meridional Transect: overview and synthesis of data. *Prog. Oceanogr.*, **45**, 257–312.
- Austin, R.W., 1974: The remote sensing of spectral radiance from below the ocean surface. In: *Optical Aspects of Oceanography*, N.G. Jerlov and E.S. Nielsen, Eds., Academic Press, London, 317–344.
- , 1980: Gulf of Mexico, ocean color surface truth measurements. *Bound.-Layer Meteorol.*, **18**, 269–285.
- , and T.J. Petzold, 1981: The determination of the diffuse attenuation coefficient of sea water using the Coastal Zone Color Scanner. In: *Oceanography from Space*, J.F.R. Gower, Ed., Plenum Press, 239–256.
- Doyle, J.P., and G. Zibordi, 1998: Correction of oceanographic tower-shading effects on in-water optical measurements. *Proc. Ocean Optics XIV*, [Available on CD-ROM], Office of Naval Research, Washington, DC.
- Gordon, H.R., and D.K. Clark, 1981: Clear water radiances for atmospheric correction of coastal zone color scanner imagery. *Appl. Opt.*, **20**, 4,175–4,180.
- , O.B. Brown, R.H. Evans, J.W. Brown, R.C. Smith, K.S. Baker, and D.K. Clark, 1988: A semianalytic radiance model of ocean color. *J. Geophys. Res.*, **93**, 10,909–10,924.
- , and K. Ding, 1992: Self shading of in-water optical instruments. *Limnol. Oceanogr.*, **37**, 491–500.
- Hooker, S.B., W.E. Esaias, G.C. Feldman, W.W. Gregg, and C.R. McClain, 1992: An Overview of SeaWiFS and Ocean Color. *NASA Tech. Memo. 104566*, Vol. 1, S.B. Hooker and E.R. Firestone, Eds., NASA Goddard Space Flight Center, Greenbelt, Maryland, 24 pp., plus color plates.

- , and W.E. Esaias, 1993: An overview of the SeaWiFS project. *Eos, Trans. AGU*, **74**, 241–246.
- , C.R. McClain, and A. Holmes, 1993: Ocean color imaging: CZCS to SeaWiFS. *Marine Tech. Soc. J.*, **27**, 3–15.
- , C.R. McClain, J.K. Firestone, T.L. Westphal, E-n. Yeh, and Y. Ge, 1994: The SeaWiFS Bio-Optical Archive and Storage System (SeaBASS), Part 1. *NASA Tech. Memo. 104566, Vol. 20*, S.B. Hooker and E.R. Firestone, Eds., NASA Goddard Space Flight Center, Greenbelt, Maryland, 40 pp.
- , and J. Aiken, 1998: Calibration evaluation and radiometric testing of field radiometers with the SeaWiFS Quality Monitor (SQM). *J. Atmos. Oceanic Tech.*, 995–1,007.
- , and C.R. McClain, 2000: The calibration and validation of SeaWiFS data. *Prog. Oceanogr.*, **45**, 427–465.
- , and S. Maritorena, 2000: An evaluation of oceanographic radiometers and deployment methodologies. *J. Atmos. Oceanic Technol.*, **17**, 811–830.
- Joint Global Ocean Flux Study, 1991: JGOFS Core Measurements Protocols. *JGOFS Report No. 6*, Scientific Committee on Oceanic Research, 40 pp.
- Loisel, H., and A. Morel, 1998: Light scattering and chlorophyll concentration in case 1 waters: A reexamination. *Limnol. Oceanogr.*, **43**, 847–858.
- Maritorena, S., A. Morel, and B. Gentili, 1994: Diffuse reflectance of oceanic shallow water: Influence of water depth and bottom albedo. *Limnol. Oceanogr.*, **39**, 1,689–1,703.
- McClain, C.R., M.L. Cleave, G.C. Feldman, W.W. Gregg, S.B. Hooker, and N. Kuring, 1998: Science quality SeaWiFS data for global biosphere research. *Sea Technol.*, **39**, 10–16.
- Mobley, C.D., 1999: Estimation of the remote-sensing reflectance from above-surface measurements. *Appl. Opt.*, **38**, 7,442–7,455.
- Morel, A., 1974: Optical properties of pure water and sea water. *Optical Aspects of Oceanography*, N.G. Jerlov and S. Nielsen, Eds., Academic Press, 1–24.
- , 1988: Optical modeling of the upper ocean in relation to its biogenous matter content (Case I waters). *J. Geophys. Res.*, **93**, 10,749–10,768.
- , and L. Prieur, 1977: Analysis of variations in ocean color. *Limnol. Oceanogr.*, **22**, 709–722.
- Mueller, J.L., 2000: "In-water radiometric profile measurements and data analysis protocols." In: Fargion, G.S., and J.L. Mueller, Ocean Optics Protocols for Satellite Ocean Color Sensor Validation, Revision 2. *NASA Tech. Memo. 2000–209966*, NASA Goddard Space Flight Center, Greenbelt, Maryland, 87–97.
- , and R.W. Austin, 1992: Ocean Optics Protocols for SeaWiFS Validation. *NASA Tech. Memo. 104566, Vol. 5*, S.B. Hooker and E.R. Firestone, Eds., NASA Goddard Space Flight Center, Greenbelt, Maryland, 43 pp.
- , and —, 1995: Ocean Optics Protocols for SeaWiFS Validation, Revision 1. *NASA Tech. Memo. 104566, Vol. 25*, S.B. Hooker, E.R. Firestone, and J.G. Acker, Eds., NASA Goddard Space Flight Center, Greenbelt, Maryland, 66 pp.
- , B.C. Johnson, C.L. Cromer, S.B. Hooker, J.T. McLean, and S.F. Biggar, 1996: The Third SeaWiFS Intercalibration Round-Robin Experiment (SIRREX-3), 19–30 September 1994. *NASA Tech. Memo. 104566, Vol. 34*, S.B. Hooker, E.R. Firestone, and J.G. Acker, Eds., NASA Goddard Space Flight Center, Greenbelt, Maryland, 78 pp.
- Neckel, H., and D. Labs, 1984: The solar radiation between 3300 and 12500 Å. *Sol. Phys.*, **90**, 205–258.
- O'Reilly, J.E., S. Maritorena, B.G. Mitchell, D.A. Siegel, K.L. Carder, S.A. Garver, M. Kahru, and C. McClain, 1998: Ocean color chlorophyll algorithms for SeaWiFS. *J. Geophys. Res.*, **103**, 24,937–24,953.
- Pope, R.M., and E.S. Fry, 1997: Absorption spectrum (380–700 nm) of pure water, II. Integrating cavity measurements. *Appl. Opt.*, **36**, 8,710–8,723.
- Press, W.H., S.A. Teukolsky, W.T. Vetterling, and B.P. Flannery, 1992: *Numerical Recipes in C: The Art of Scientific Computing*. Cambridge University Press, 994 pp.
- Priesendorfer, R.W., and C.D. Mobley, 1986: Albedos and glint patterns of a wind roughened sea surface. *J. Phys. Oceanogr.*, **16**, 1,293–1,316.
- Siegel, D.A., M.C. O'Brien, J.C. Sorensen, D.A. Konnoff, E.A. Brody, J.L. Mueller, C.O. Davis, W.J. Rhea, and S.B. Hooker, 1995: Results of the SeaWiFS Data Analysis Round-Robin (DARR-94), July 1994. *NASA Tech. Memo. 104566, Vol. 26*, S.B. Hooker and E.R. Firestone, Eds., NASA Goddard Space Flight Center, Greenbelt, Maryland, 58 pp.
- Sildam, J., M.R. Lewis, and J.C. Cullen, 1998: Multiresolution analysis of diffuse attenuation coefficient with an emphasis on surface and deep layers, Ocean Optics XIV.
- Smith, R.C., and K.S. Baker, 1981: The biooptical state of ocean waters and remote sensing. *Limnol. Oceanogr.*, **23**, 247–259.
- , and —, 1984: Analysis of ocean optical data. *Ocean Optics VII*, M. Blizard, Ed., SPIE, **478**, 119–126.
- , and —, 1986: Analysis of ocean optical data II. *Ocean Optics VIII*, P.N. Slater, Ed., SPIE, **637**, 95–107.
- Zibordi, G., and M. Ferrari, 1995: Instrument self-shading in underwater optical measurements: Experimental data. *Appl. Opt.*, **34**, 2,750–2,754.
- , J.P. Doyle, and S.B. Hooker, 1999: Offshore tower shading effects on in-water optical measurements. *J. Atmos. Ocean. Tech.*, **16**, 1,767–1,779.

—, J-F. Berthon, J.P. Doyle, S. Grossi, D. van der Linde, C. Targa and L. Alberotanza, 2001: Coastal Atmosphere and Sea Time Series (CoASTS): A tower based long-term measurement project supporting bio-optical modeling and ocean color cal/val in the North Adriatic Sea. *J. Atmos. Ocean. Tech.*, (submitted).

THE SEAWiFS POSTLAUNCH TECHNICAL REPORT SERIES

Vol. 1

Johnson, B.C., J.B. Fowler, and C.L. Cromer, 1998: The SeaWiFS Transfer Radiometer (SXR). *NASA Tech. Memo. 1998-206892, Vol. 1*, S.B. Hooker and E.R. Firestone, Eds., NASA Goddard Space Flight Center, Greenbelt, Maryland, 58 pp.

Vol. 2

Aiken, J., D.G. Cummings, S.W. Gibb, N.W. Rees, R. Woodd-Walker, E.M.S. Woodward, J. Woolfenden, S.B. Hooker, J-F. Berthon, C.D. Dempsey, D.J. Suggett, P. Wood, C. Donlon, N. González-Benítez, I. Huskin, M. Quevedo, R. Barciela-Fernandez, C. de Vargas, and C. McKee, 1998: AMT-5 Cruise Report. *NASA Tech. Memo. 1998-206892, Vol. 2*, S.B. Hooker and E.R. Firestone, Eds., NASA Goddard Space Flight Center, Greenbelt, Maryland, 113 pp.

Vol. 3

Hooker, S.B., G. Zibordi, G. Lazin, and S. McLean, 1999: The SeaBOARR-98 Field Campaign. *NASA Tech. Memo. 1999-206892, Vol. 3*, S.B. Hooker and E.R. Firestone, Eds., NASA Goddard Space Flight Center, Greenbelt, Maryland, 40 pp.

Vol. 4

Johnson, B.C., E.A. Early, R.E. Eplee, Jr., R.A. Barnes, and R.T. Caffrey, 1999: The 1997 Prelaunch Radiometric Calibration of SeaWiFS. *NASA Tech. Memo. 1999-206892, Vol. 4*, S.B. Hooker and E.R. Firestone, Eds., NASA Goddard Space Flight Center, Greenbelt, Maryland, 51 pp.

Vol. 5

Barnes, R.A., R.E. Eplee, Jr., S.F. Biggar, K.J. Thome, E.F. Zalewski, P.N. Slater, and A.W. Holmes 1999: The SeaWiFS Solar Radiation-Based Calibration and the Transfer-to-Orbit Experiment. *NASA Tech. Memo. 1999-206892, Vol. 5*, S.B. Hooker and E.R. Firestone, Eds., NASA Goddard Space Flight Center, 28 pp.

Vol. 6

Firestone, E.R., and S.B. Hooker, 2000: SeaWiFS Postlaunch Technical Report Series Cumulative Index: Volumes 1-5. *NASA Tech. Memo. 2000-206892, Vol. 6*, S.B. Hooker and E.R. Firestone, Eds., NASA Goddard Space Flight Center, Greenbelt, Maryland, 14 pp.

Vol. 7

Johnson, B.C., H.W. Yoon, S.S. Bruce, P-S. Shaw, A. Thompson, S.B. Hooker, R.E. Eplee, Jr., R.A. Barnes, S. Maritorena, and J.L. Mueller, 1999: The Fifth SeaWiFS Intercalibration Round-Robin Experiment (SIRREX-5), July 1996. *NASA Tech. Memo. 1999-206892, Vol. 7*, S.B. Hooker and E.R. Firestone, Eds., NASA Goddard Space Flight Center, 75 pp.

Vol. 8

Hooker, S.B., and G. Lazin, 2000: The SeaBOARR-99 Field Campaign. *NASA Tech. Memo. 2000-206892, Vol. 8*, S.B. Hooker and E.R. Firestone, Eds., NASA Goddard Space Flight Center, 46 pp.

Vol. 9

McClain, C.R., E.J. Ainsworth, R.A. Barnes, R.E. Eplee, Jr., F.S. Patt, W.D. Robinson, M. Wang, and S.W. Bailey, 2000: SeaWiFS Postlaunch Calibration and Validation Analyses, Part 1. *NASA Tech. Memo. 2000-206892, Vol. 9*, S.B. Hooker and E.R. Firestone, Eds., NASA Goddard Space Flight Center, 82 pp.

Vol. 10

McClain, C.R., R.A. Barnes, R.E. Eplee, Jr., B.A. Franz, N.C. Hsu, F.S. Patt, C.M. Pietras, W.D. Robinson, B.D. Schieber, G.M. Schmidt, M. Wang, S.W. Bailey, and P.J. Werdell, 2000: SeaWiFS Postlaunch Calibration and Validation Analyses, Part 2. *NASA Tech. Memo. 2000-206892, Vol. 10*, S.B. Hooker and E.R. Firestone, Eds., NASA Goddard Space Flight Center, 57 pp.

Vol. 11

O'Reilly, J.E., and 24 Coauthors, 2000: SeaWiFS Postlaunch Calibration and Validation Analyses, Part 3. *NASA Tech. Memo. 2000-206892, Vol. 11*, S.B. Hooker and E.R. Firestone, Eds., NASA Goddard Space Flight Center, 49 pp.

Vol. 12

Firestone, E.R., and S.B. Hooker, 2001: SeaWiFS Postlaunch Technical Report Series Cumulative Index: Volumes 1-11. *NASA Tech. Memo. 2001-206892, Vol. 12*, S.B. Hooker and E.R. Firestone, Eds., NASA Goddard Space Flight Center, Greenbelt, Maryland, 24 pp.

Vol. 13

Hooker, S.B., G. Zibordi, J-F. Berthon, S.W. Bailey, and C.M. Pietras, 2000: The SeaWiFS Photometer Revision for Incident Surface Measurement (SeaPRISM) Field Commissioning. *NASA Tech. Memo. 2000-206892, Vol. 13*, S.B. Hooker and E.R. Firestone, Eds., NASA Goddard Space Flight Center, Greenbelt, Maryland, 24 pp.

Vol. 14

Hooker, S.B., H. Claustre, J. Ras, L. Van Heukelem, J-F. Berthon, C. Targa, D. van der Linde, R. Barlow, and H. Sessions, 2000: The First SeaWiFS HPLC Analysis Round-Robin Experiment (SeaHARRE-1). *NASA Tech. Memo. 2000-206892, Vol. 14*, S.B. Hooker and E.R. Firestone, Eds., NASA Goddard Space Flight Center, Greenbelt, Maryland, 42 pp.

Vol. 15

Hooker, S.B., G. Zibordi, J-F. Berthon, D. D'Alimonte, S. Maritorena, S. McLean, and J. Sildam, 2001: Results of the Second SeaWiFS Data Analysis Round Robin, March 2000 (DARR-00). *NASA Tech. Memo. 2001-206892, Vol. 15*, S.B. Hooker and E.R. Firestone, Eds., NASA Goddard Space Flight Center, Greenbelt, Maryland, 71 pp.

REPORT DOCUMENTATION PAGE

Form Approved
OMB No. 0704-0188

Public reporting burden for this collection of information is estimated to average 1 hour per response, including the time for reviewing instructions, searching existing data sources, gathering and maintaining the data needed, and completing and reviewing the collection of information. Send comments regarding this burden estimate or any other aspect of this collection of information, including suggestions for reducing this burden, to Washington Headquarters Services, Directorate for Information Operations and Reports, 1215 Jefferson Davis Highway, Suite 1204, Arlington, VA 22202-4302, and to the Office of Management and Budget, Paperwork Reduction Project (0704-0188), Washington, DC 20503.

1. AGENCY USE ONLY (Leave blank)

2. REPORT DATE
December 2001

3. REPORT TYPE AND DATES COVERED
Technical Memorandum

4. TITLE AND SUBTITLE

SeaWiFS Postlaunch Technical Report Series
Volume 15: Results of the Second SeaWiFS Data Analysis Round Robin,
March 2000 (DARR-00)

S.B. Hooker, G. Zibordi, J-F. Berthon, D. D'Alimonte, S. Maritorena, S. McLean,
and J. Sildam

Series Editors: Stanford B. Hooker and Elaine R. Firestone

5. FUNDING NUMBERS

970.2

7. PERFORMING ORGANIZATION NAME(S) AND ADDRESS(ES)

Laboratory for Hydrospheric Processes
Goddard Space Flight Center
Greenbelt, Maryland 20771

8. PERFORMING ORGANIZATION
REPORT NUMBER

2002-00609-0

9. SPONSORING/MONITORING AGENCY NAME(S) AND ADDRESS(ES)

National Aeronautics and Space Administration
Washington, D.C. 20546-0001

10. SPONSORING/MONITORING
AGENCY REPORT NUMBER

TM—2001—206892, Vol. 15

11. SUPPLEMENTARY NOTES

E.R. Firestone: Science Applications International Corporation, Beltsville, Maryland; G. Zibordi, J-F. Berthon and D. D'Alimonte: JRC Space Applications Institute, Ispra, Italy; S. Maritorena: UCSB Institute for Computational Earth System Science, Santa Barbara, California; and S. McLean and J. Sildam: Satlantic, Inc., Halifax, Canada

12a. DISTRIBUTION/AVAILABILITY STATEMENT

Unclassified-Unlimited
Subject Category 48
Report is available from the Center for AeroSpace Information (CASI),
7121 Standard Drive, Hanover, MD 21076-1320; (301)621-0390

12b. DISTRIBUTION CODE

13. ABSTRACT (Maximum 200 words)

The accurate determination of upper ocean apparent optical properties (AOPs) is essential for the vicarious calibration of the Sea-viewing Wide Field-of-view Sensor (SeaWiFS) instrument and the validation of the derived data products. To evaluate the importance of data analysis methods upon derived AOP values, the Second Data Analysis Round Robin (DARR-00) activity was planned during the latter half of 1999 and executed during March 2000. The focus of the study was the intercomparison of several standard AOP parameters: a) the upwelled radiance immediately below the sea surface, $L_u(0^-, \lambda)$; b) the downward irradiance immediately below the sea surface, $E_d(0^-, \lambda)$; c) the diffuse attenuation coefficients from the upwelling radiance and the downward irradiance profiles, $K_L(\lambda)$ and $K_d(\lambda)$, respectively; d) the incident solar irradiance immediately above the sea surface, $E_s(0^+, \lambda)$; e) the remote sensing reflectance, $R_{rs}(\lambda)$; f) the normalized water-leaving radiance, $[L_w(\lambda)]_N$; g) the upward irradiance immediately below the sea surface, $E_u(0^-)$, which is used with the upwelled radiance to derive the nadir Q -factor immediately below the sea surface, $Q_n(0^-, \lambda)$; and h) ancillary parameters like the solar zenith angle, θ , and the total chlorophyll a concentration, C_{ta} , derived from the optical data through statistical algorithms. In the results reported here, different methodologies from three research groups were applied to an identical set of 40 multispectral casts in order to evaluate the degree to which differences in data analysis methods influence AOP estimation, and whether any general improvements can be made. The overall results of DARR-00 are presented in Chapter 1 and the individual methods used by the three groups and their data processors are presented in Chapters 2-4.

14. SUBJECT TERMS

SeaWiFS, Oceanography, Data Analysis, Round-Robin, DARR-00, Data Processing

15. NUMBER OF PAGES

71

16. PRICE CODE

17. SECURITY CLASSIFICATION
OF REPORT

Unclassified

18. SECURITY CLASSIFICATION
OF THIS PAGE

Unclassified

19. SECURITY CLASSIFICATION
OF ABSTRACT

Unclassified

20. LIMITATION OF ABSTRACT

Unlimited